CHANDRA EJECTA KINEMATICS STUDIES AND AN ISO SPECTROSCOPIC SURVEY OF SUPERNOVA REMNANTS

by

MATTHEW JAMES MILLARD

Presented to the Faculty of the Graduate School of
The University of Texas at Arlington in Partial Fulfillment
of the Requirements
for the Degree of

DOCTOR OF PHILOSOPHY

THE UNIVERSITY OF TEXAS AT ARLINGTON

August 2022

Copyright © by MATTHEW JAMES MILLARD 2022

All Rights Reserved

To my family, I am truly lucky to have you.

ACKNOWLEDGEMENTS

I would like to express my deep gratitude to my advisor, Sangwook Park, for his invaluable guidance and wisdom. He has set an example for how to be an astronomer.

I am grateful for the contributions of my scientific collaborators, Jack Hughes, Pat Slane, Toshiki Sato, Carles Badenes, David Burrows, and Dan Patnaude, who lent me their expert insight and advice. I extend a special thanks to Jeonghee Rho, for helping me to expand my work into infrared astronomy.

I appreciate the efforts of my committee members at UTA, Manfred Cuntz, Zdzislaw Musielak, Ramon Lopez, and Ben Jones, who patiently reviewed my doctoral work. I thank Stacey Codey for helping me with so many of my administrative issues.

I would also like to recognize my former advisor at Clemson University, Timothy DeVol, for helping me to start down this academic path.

Finally, I thank my colleagues and friends, Jayant Bhalerao, Aravind Pazhayath Ravi, Ananta Chalise, Michael Greene, Nil Pandey, Yuting Peng, Suman Satyal, and many others for their camaraderie and support.

August 3, 2022

ABSTRACT

CHANDRA EJECTA KINEMATICS STUDIES AND AN ISO SPECTROSCOPIC SURVEY OF SUPERNOVA REMNANTS

MATTHEW JAMES MILLARD, Ph.D.

The University of Texas at Arlington, 2022

Supervising Professor: Dr. Sangwook Park

The structure of metal-rich ejecta created from a supernova (SN) reveals vital information about the explosion of the progenitor star and the dynamical evolution of the supernova remnant (SNR). This research focuses on the ejecta kinematics of SNRs in two projects. In the first project, we use High Energy Transmission Grating (HETG) spectroscopy and archival Advanced CCD Imaging Spectrometer (ACIS) imaging from the Chandra X-ray Observatory to study the 3-D ejecta structure of the remnants of the historical Type Ia SNe, SN 1572 (Tycho's SNR) and SN 1604 (Kepler's SNR). We use our 150 ks high-resolution Chandra HETG spectroscopic observation of Kepler's SNR to reveal the 3-D spatial distribution of SN ejecta by measuring the line-of-sight (radial, v_r) velocities of clumpy ejecta gas throughout the remnants. We measure the v_r of 15 ejecta knots mainly in the northern part of the remnant. We estimate high v_r of up to $\sim$ 8000 km s^{-1} for some of these ejecta knots. We also measure proper motions for our sample based on the archival Chandra ACIS data taken in 2000, 2006, and 2014. The fastest moving knots show proper motions of up to $\sim 0\farcs2$ per year. Our measured v_r and proper motions imply space velocities

up to $\sim$ 9000 km s^{-1}, thus indicating that some of these ejecta knots are almost freely expanding after $\sim$ 400 yr since the explosion. Assuming that these high-velocity ejecta knots are traveling ahead of the forward shock of the SNR, we estimate the distance to Kepler's SNR, $d \sim$ 4.4–7.5 kpc. We find that the ejecta knots in our sample have an average space velocity of $v_s \sim$ 4600 km s^{-1} (assuming a distance of 6 kpc to Kepler's SNR). We note that 8 of the 15 ejecta knots from our sample show a statistically significant (at the 90% confidence level) redshifted spectrum, compared to only two with a blueshifted spectrum. This may suggest an asymmetry in the ejecta distribution in Kepler's SNR along the line of sight.

In Tycho's SNR, we use our 450 ks Chandra HETGS observation to study the ejecta kinematics. We find radial velocities of up to $v_r \sim$ 5,500 km s^{-1} in our sample of 59 ejecta knots scattered about the face of the SNR. We also measure the proper motions for our sample based on the archival Chandra ACIS data taken from 2003, 2009, and 2015. We estimate proper motions up to $0\farcs35$ yr^{-1}, and total space velocities of up to 6000 km s^{-1} (assuming a distance of 3.5 kpc to Tycho's SNR). We find that ejecta in the southeast quadrant generally expand faster than the rest of the SNR. A 3–D construction shows an apparent asymmetry in the spatial distribution of ejecta clumps with more blueshifted knots located towards the north and more redshifted knots in the south. We find that the inferred positions of the ejecta knots suggest that the reverse shock may reach further into the interior than previously estimated.

In the second project, we study the far-infrared (FIR) spectra of SNRs with a particular focus on searching for high-velocity IR-emitting ejecta (by detecting strong emission line broadening) that may be coincident with emission from newly formed dust in core-collapse (CC) SNRs. Our goal is to help reveal whether CC–SNe could be the main producer of interstellar dust. We present FIR spectroscopy of SNRs based on the archival data of the Infrared Space Observatory taken with the Long Wavelength

Spectrometer (LWS). Our sample includes previously unpublished profiles of line and continuum spectra for 20 SNRs in the Galaxy and Magellanic Clouds. In several SNRs including G21.5–0.9, G29.7–0.3, the Crab Nebula, and G320.4–1.2, we find evidence for broad [O I], [O III], [N II], and [C II] lines. We measure velocity dispersions up to a few 10^3 km s^{-1}, indicating that they are associated with high-velocity SN ejecta. For G320.4–1.2, we apply a blackbody model fit to the LWS continuum, taking into account the SNR and background emission. Based on this model, we estimate 0.1 – 0.2 $M_\odot$ of interstellar dust formation in this SNR.

TABLE OF CONTENTS

LIST OF ILLUSTRATIONS

LIST OF TABLES

CHAPTER 1

Introduction

1.1 Elements of the Universe

In the early Universe, the total amount of baryonic mass consisted almost entirely of only hydrogen ($\sim 75\%$) and helium ($\sim 25\%$) (Coc & Vangioni, 2010). Today, other elements, which astronomers refer to as "metals", make up about 1.4% of the mass in our solar neighborhood (Asplund et al., 2021). Metals play an impactful role in important physical processes. Without them, complex chemistry and biology would not be able to develop. How has our local neighborhood and the Universe in general become enriched with these elements? The answer lies at the end of a star's life, when it disperses metal-rich material into the interstellar medium (ISM) and illuminates the Universe in the ultimate cosmic explosion, a supernova (SN).

Stars form from dense knots in clouds of molecular hydrogen (H_2). These molecular clouds (MCs) are embedded throughout the ISM and contain as much mass as several million suns (solar masses, $M_\odot$; Miura et al. (2021)). Eventually, gravitational attraction causes parts of the cloud to condense into clumps. As gas falls towards the center of the clump, it heats up, and the temperature and pressure at the core builds. The temperatures at the center eventually reach a few 10^6 K, hot enough to begin fusion of hydrogen atoms into helium. The outward pressure caused by the heat at the core and the inward pressure caused by the weight of the outer layers eventually balance each other out. Thus, hydrostatic equilibrium is achieved and a star is born. A star will spend most of its lifetime primarily converting hydrogen to helium in its core. During this time, stars are said to be on the "main sequence".

When stars eventually begin fusing heavier elements (e.g., carbon, oxygen, etc.) they are no longer considered to be a main sequence star. Depending on the mass of the star, they will continue to burn heavier elements. Stars with masses $\lesssim 8$ $M_\odot$, are considered "low-mass" stars. When nuclear fusion ceases in low-mass stars, they leave behind a dense core composed primarily of carbon and oxygen, a so called "white dwarf". Stars with masses $\gtrsim 8$ $M_\odot$ are considered to be "high-mass" (or "massive") stars, and will burn heavier elements, up to Fe. At the end of their lifetimes, massive stars and certain white dwarfs with binary companions will go supernova, detonating in an explosion so bright that it can briefly outshine its entire host galaxy.

1.2 History of Supernova Observations

Although our understanding of SNe has developed only within the last ~ 100 years, they have been observed for at least a few millenia. The first confirmed observation of an SN was in 185 A.D. when Chinese astronomers saw a new star in the sky which remained visible for several months (Hsi, 1957). Humanity has since observed several more SNe throughout history before the advent of telescopes, e.g., SN 1006, SN 1054, SN 1572, and most recently, SN 1604[1]. These historical SNe happened in our Galaxy, and thus were bright enough to be observed with the naked eye. The first modern recognition of SNe happened in the early 1930s, when astronomers Fritz Zwicky and Walter Baade noted the appearance of several extremely bright novae which had been captured on photographic plates (Baade & Zwicky, 1934). They coined the term "supernova" to differentiate them from "common" novae, which were much more frequent and thousands of times dimmer. Currently, with the help of

[1]The SN that created the supernova remnant Cassiopeia A, may have been observed briefly in 1680 by astronomer John Flamsteed (Ashworth, 1980).

dedicated astronomical surveys, SNe are observed at a rate of a several thousand per year [2].

1.3 Supernova Types

Observationally, supernovae are grouped into types based on optical spectra taken near maximum light and their light curves (e.g., see Figure 1.1 and Gal-Yam (2017) for a review). After the initial explosion, the brightness of an SN rapidly increases for a few weeks until it reaches a maximum luminosity of up to $\sim 10^{43}$ ergs s^{-1}, well over a billion times as luminous as the sun. Supernovae near maximum brightness that display a strong Hα line (at 6562.8 Å) in their spectra are classified to be Type II. A strong Hα line indicates the presence of hydrogen in the outer layers of the exploding star. Type II SNe are divided into Types IIP and IIL, based on their light curves. The light curves of Type IIL SNe decay linearly in magnitude, while Type IIP have a plateau which lasts up to 3 months, caused by an extended outer layer of hydrogen (Branch & Wheeler, 2017). Type II SNe may also be grouped by their spectra. Type IIb SNe transition from having typical Type II hydrogen-rich spectra to He-dominated SN Ib-like spectra near maximum light. Type IIn SNe show strong, narrow hydrogen emission lines, possibly from heated circumstellar material (CSM) (Chugai & Danziger, 1994).

Supernovae without a strong Hα line in their spectra near maximum brightness are classified as Type I. These SNe did not have a hydrogen shell when the SN occurred. Type I SNe are divided further into Types Ia, Ib, and Ic. Type Ia SNe show a strong silicon absorption line at 6355 Å. Type Ib SNe show strong helium lines, while Type Ic SNe show neither hydrogen nor helium lines. Types Ib and Ic are likely cases of massive stars that blew off their hydrogen- and/or helium-rich

[2] https://www.rochesterastronomy.org/sn2021/snstats.html

outer layers (Wheeler & Harkness, 1990). The origin of a Type II or Ib/c SN is the gravitational collapse of a massive star, while the origin of a Type Ia SN is the runaway thermonuclear explosion of a white dwarf.

1.4 Type Ia Supernovae

Type Ia SNe result from the explosive thermonuclear unbinding of a white dwarf (WD), the extremely dense remnant cores of low-mass stars that are composed primarily of carbon and oxygen. Due to their extreme densities ($\sim 10^9$ kg m^{-3}), the lower electron energy states in a WD are filled, leaving only higher energy states. Thus, free electrons in a WD must have extremely high velocities, creating an electron-degeneracy pressure. However, electron-degeneracy pressure eventually fails when WDs reach masses up to 1.4 $M_\odot$ (the Chandrasekhar limit), at which point the WD may collapse to an even denser state. Since electron-degeneracy pressure is not sensitive to temperature, if a sufficiently strong fusion reaction occurs in a WD, it will not be able to expand to cool, and the fusion will continue at an extremely fast rate until it becomes a runaway reaction, resulting in a Type Ia SN.

White dwarfs have typical masses of ~ 0.6 $M_\odot$ (Kepler et al., 2007), and thus require a mass transfer from a companion star to approach the Chandrasekhar limit. To acquire mass, a WD should be close enough to a companion such that the gravitational pull from the WD on the companion's outer layers becomes stronger than that from the companion itself, also known as Roche-lobe overflow. The most likely candidate to donate mass is an evolved star, in particular, those in the Asymptotic Giant Branch (AGB) phase, since their outer layers are less strongly bound than main-sequence stars. This scenario is called the single degenerate (SD) channel. This SD channel is supported by the presence of CSM observed in some Type Ia supernova remnants, such as the remnant of SN 1604 (Burkey et al., 2013; Chiotellis et al.,

2012) or supernova remnant N103B (Guest et al., 2022; Williams et al., 2014). The companion donor star is expected to survive the blast wave impact from the SN.

The double-degenerate (DD) channel involves the merging of two WDs, creating a single more massive white dwarf that approaches the Chandrasekhar limit and eventually explodes. Some Type Ia SNe appear to have a high ^{56}Ni yield for which the total mass exceeds the Chandrasekhar limit, and thus must have resulted from the merger of WDs with a total mass greater than the Chandrasekhar limit (Howell et al., 2006). In the general case of the DD channel, both WDs are destroyed, leaving no companion behind. However, some scenarios suggest that the primary WD can accrete enough mass to approach the Chandrasekhar limit without totally destroying the secondary WD (Shen et al., 2018).

In the simplest model of the thermonuclear explosion of a WD (i.e., a Type Ia SN), a supersonic burning flame, referred to as a detonation, propagates out from the center of the WD. Simple detonation models produce mostly iron-group elements, however, observations of the Type Ia ejecta also indicate the presence of intermediate-mass elements like Si, S, Ar, and Ca. An alternative model which better aligns with observed ejecta abundances is the deflagration wave, where a subsonic burning layer is fueled by convection of unburned carbon and oxygen material. A combination of both the deflagration and detonation flames, the delayed detonation model (DDT), is a scenario where the burning wave starts as a deflagration and then turns into a detonation when the wave encounters a region of lower density (Khokhlov, 1991). DDT models generally match the observed elemental signatures even better than deflagration models. There are many modifications to the standard deflagration, detonation, and DDT models that are physically viable (see Hillebrandt & Niemeyer (2000) for a review).

1.5 Core–Collapse Supernovae

The fate of nearly all massive stars ($\gtrsim 8$ $M_\odot$) is determined from their birth. Due to their interior composition in their late-stage evolution, they will eventually explode as core-collapse (CC)–SNe (see Woosley et al. (2002) for a review). All stars fuse hydrogen into helium during most of their lifetimes. In massive stars, the extreme temperatures and densities at the core allow fusion of heavier elements, up to the creation of Fe nuclei. However, the reactions required to fuse elements heavier than Fe are endothermic, and thus energy is lost with each reaction. With energy no longer being produced from fusion, the core eventually begins to collapse, causing it to heat up to extreme temperatures. The γ-rays created from the high temperatures interact with the Fe nuclei, causing them to photodissociate. Meanwhile, the electron-degeneracy pressure previously stabilizing the core is overwhelmed by the infalling matter, causing electrons and protons to merge into neutrons. These reactions release copious amounts of neutrinos which further cool the core, causing it to contract even more, creating a proto-neutron star.

The outer layers of the star fall towards center, and bounce off the proto-neutron star core, creating an outwardly traveling shock wave (e.g., Figure 2 in Janka et al. (2012)). As the shock wave travels through the remaining outer layers of the star, explosive nucleosynthesis occurs. However, the bulk of ejecta from CC–SNe are the carbon, oxygen, neon, and magnesium, that were fused throughout the lifetime of the star before the SN and were blown out by the explosion (Woosley & Weaver, 1995).

1.6 Supernova Remnant Evolution

The explosive ejection of stellar debris into the ISM by an SN creates a blast wave that travels radially outward from the exploding star at mean velocities of $\sim 10^4$

km s^{-1} (Wongwathanarat et al., 2015; Wilk et al., 2018). This blast wave is known as the forward shock (FS), and generally represents the outermost boundary of a supernova remnant (SNR). The strength of a shock is often measured by the ratio of the shock velocity divided by the speed of sound in the medium in which the shock is propagating, i.e, the Mach number. The speed of sound in the ISM is generally ~ 10 km s^{-1} (Burkert, 2006), meaning the Mach number is roughly 10^3, an extremely strong shock. Decelerations in the FS cause the development of the so-called reverse shock, which propagates back through the ejecta, heating and compressing it (see Figure 1.2). A contact discontinuity (CD) forms, separating the shocked ISM gas shocked by the FS from the expanding ejecta. For the first few thousands years after the explosion, radiative losses are small (although are still of observational importance), and the expansion is adiabatic (Truelove & McKee, 1999). The shocked gas in young SNRs is heated to several 10^6 Kelvin, and thus radiates in X-rays. The emitted X-ray spectra are often dominated by line emission from the ejected elements (O, Ne, Mg, Si, S, Ar, Ca, and Fe).

The expansion of SNRs can generally be described by $R \propto t_{exp}^{\eta}$, where R is the radius of the SNR, t_{exp} is the time since the explosion, and η is the expansion index. As they evolve, SNRs are characterized by four distinct phases (Chevalier, 1977). Early on in the evolution of the SNR, although the expansion is immediately slowed by the surrounding medium, the expansion index is still roughly $\eta \sim 1$, meaning the blast wave expands at a nearly constant speed. This "free-expansion" stage typically may last a few hundred years. An example of an such a young SNR is the ~ 100 yr-old G1.9+0.3, which is expanding at 13,000 km s^{-1} (Carlton et al., 2011). As the swept up mass of the ISM increases, the blast wave decelerates to adiabatically expand with a negligible radiative loss of the kinetic energy. An analytic solution to describe this stage is analogous a point-explosion in a uniform medium, as studied

by John Taylor and Leonid Sedov (as well as John von Neumann) (von Neumann, 1947; Taylor, 1950; Sedov, 1959). Thus, the corresponding SNR phase is generally referred to as the "Sedov-Taylor", or "adiabatic" stage. The self-similar solution, $R = 1.15(E/\rho)^{1/5}t_{exp}^{2/5}$, conveniently relates SNR radius to the explosion energy E and uniform ambient density ρ. The expansion index for the Sedov-Taylor stage is 0.4, which may last up to several 10^4 years.

As the remnant continues to decelerate and cool, temperatures behind the shock front drop to the point where radiative processes become significant. Therefore, energy is no longer conserved. A dense cool shell of gas forms behind the FS and conserves the momentum of the shock. This epoch in the SNRs evolution is called the "momentum-conservation" (or "snowplough") stage. The expansion index is $0.25-0.3$ and the shock velocity is a few 10^2 km s^{-1}. Eventually, the shock decelerates to speeds less than the speed of sound in the ISM, and the shock dissipates and mixes with the ambient gas during the "merging" stage.

1.6.1 Dust Production in SNRs

As the ejecta cools towards the interior of the remnant, molecules (in particular, CO) and dust begin to form, only a few years after the SN (Nozawa et al., 2003). The abundant metals in the ejecta help to seed it with dust grains, with common dust species including $MgSiO_3$, SiO_2, Mg_2SiO_4, and C (Williams & Temim, 2017). Freshly formed dust has been observed in several SNRs with estimated dust masses of ~ 0.01 to 1 $M_\odot$ (Rho et al., 2009; Gomez et al., 2012; Matsuura et al., 2015; De Looze et al., 2017; Rho et al., 2018; Chawner et al., 2019). Some dust is likely destroyed by the reverse shock, however large enough dust grains ($\gtrsim 0.1$ μm) may survive to populate the ISM (Slavin et al., 2020).

1.7 Thesis Composition

This work is a compilation of studies that mainly focus on the kinematics of ejecta in young SNRs. In Chapters 2 and 3, we examine the 3–D structure of the historical Type Ia SNRs, Kepler's SNR and Tycho's SNR (Kepler and Tycho, respectively, hereafter). We use high-resolution gratings spectroscopy data of the Chandra X-ray Observatory (Chandra, hereafter) to measure the Doppler shift of the He-like Si Kα line at $\sim$ 1.865 keV, and thus estimate the line-of-sight, or radial velocity (v_r) of clumpy stellar debris in these SNRs. We also make use of archival Chandra images at different epochs to estimate the proper motion (positional changes of an object across the plane of the sky) of the clumpy ejecta gas. Based on the measurements of radial velocities and proper motions, we estimate the 3-D space velocity of individual clumpy ejecta "knots".

In Chapter 4, we present the line and continuum spectra for an unpublished Infrared Space Observatory (ISO; Kessler et al., 1996) sample of 20 SNRs in the Galaxy and Magellanic Clouds. In most remnants, we detect one or more far-infrared (FIR) atomic fine-structure lines: [O I] 63 and 145 μm, [O III] 52 and 88 μm, [N II] 122 μm, and [C II] 158 μm. In 10 SNRs, we find evidence for Doppler line broadening, indicating that they are from high–speed SN ejecta. By applying a blackbody model fit to the continuum in SNR G320.4–1.2, we estimate the lower limit of dust mass associated with SN ejecta. In the following Sections, 1.8 and 1.9, we give details on the overall design, onboard detectors, and data products of the telescopes utilized in this work, Chandra and ISO. The text, figures, and tables in Chapters 2, 3, and 4 are mostly adapted from Millard et al. (2020), Millard et al. (2022), and Millard et al. (2021), respectively. In Chapter 5, we summarize and conclude our work.

1.8 Chandra X-ray Observatory

Chandra is one of the four Great Observatories commissioned by the National Aeronautics and Space Administration (NASA). Launched in 1999, it is the premier X-ray telescope of its time, offering superior spatial and spectral resolution compared to other X-ray telescopes. The main elements of Chandra are (1) the High Resolution Mirror Assembly (HRMA), which focuses the X-rays onto the science instruments, (2) the Pointing Control and Aspect Determination (PCAD), which controls the pointing and dithering of the observatory, (3) the Focal-plane Science Instruments (SIs) that provide charged-coupled device (CCD) imaging and spectroscopic capabilities, and (4) the transmission gratings, for high-resolution spectroscopy[3]. The HRMA consists of 4 pairs of concentric thin-walled, grazing-incidence mirrors with a focal length of 10 m. The largest mirror has a diameter of 1.2 m.

Chandra has two SIs, the Advanced Imaging CCD Spectrometer (ACIS, hereafter) and the High Resolution Camera (HRC). The ACIS chips are capable of CCD spectroscopy, while the HRC chips only have imaging capabilities. ACIS is sensitive to X-ray energies of 0.2 to 10.0 keV. In this work, we focus on ACIS, since we require spectral information for our analyses. ACIS is split into two arrays, the ACIS-I array and the ACIS-S array. The ACIS-I array is comprised of four chips in a 2×2 grid, while the ACIS-S array has six chips placed in a single row (Figure 1.3). Each ACIS chip is 1024×1024 pixels, and each pixel is $0\farcs492$ across. A subpixel algorithm can be applied to the data which improves the spatial resolution by $\sim 50\%$ (Li et al., 2004).

Chandra has two grating spectrometers, the High Energy Transmission Grating Spectrometer (HETGS) and the Low Energy Transmission Grating Spectrometer (LETGS). The gratings can be deployed such that the dispersed spectrum falls on

[3]https://cxc.harvard.edu/proposer/POG/html/index.html

the ACIS-S chips. In our work, we use the HETGS, which has roughly twice the resolving power of the LETGS at our energy band of interest (the Si Kα band at $\sim$ 1.86 keV). The dispersion angle, β, of each photon is determined by the equation

$$sin(\beta) = m\lambda/p$$

where λ is the wavelength of the photon, m is the order, and p is the grating period. The HETGS is comprised of two legs, the Medium Energy Grating (MEG), and the High Energy Grating (HEG) (see Figure 1.4). The MEG and HEG have resolving powers of $\sim$ 300 and $\sim$ 600, respectively, at 1.86 keV[4]. The grating spectroscopy of the HETGS offers up to $\sim$ 100 times the resolving power of the CCD spectroscopy of ACIS.

1.8.1 Chandra Data Processing and Analysis

The Chandra Interactive Analysis of Observations (CIAO) (Fruscione et al., 2006) is a software suite developed by the Chandra X-ray Center. The CIAO package aids users in the reprocessing and analysis of data from the Chandra X-ray Telescope. Data from Chandra are disseminated as Flexible Image Transport System (FITS) files. The FITS format is convenient for storing data in multidimensional arrays and is the primary format used for astronomical data. The FITS files created from Chandra observations record the location on the detector, energy, and arrival time of each detected photon. CIAO may be used to extract the imaging, spectroscopic, and time series information from a FITS file.

[4]https://cxc.harvard.edu/proposer/POG/html/chap8.html

1.9 Infrared Space Observatory

The ISO mission, an infrared space telescope developed and operated by the European Space Agency (ESA) in cooperation with the Institute of Space and Astronautical Science (ISAS) and NASA, operated from November 1995 to May 1998. It utilized a 60–cm diameter primary mirror cooled to 1.7 K with superfluid helium, and performed over 26,000 scientific observations during its run. ISO consisted of four main science instruments: the ISO infrared camera (ISOCAM) covered the 2.5 to 17 micron band, the ISO photo-polarimeter (ISOPHOT) operated between 2.5 and 240 microns, the Short-Wave Spectrometer (SWS) covered the 2.4 to 45 micron band, and the Long Wavelength Spectrometer (LWS; Clegg et al., 1996) which operated in the 40 – 200 μm band. A comprehensive review of the achievements of ISO can be found in Cesarsky & Salama (2006). In this work, we utilize archival data from the LWS, since it is an ideal instrument for measuring FIR atomic fine-structure lines and continuum emission from cool dust in SN ejecta. The spectra available in the LWS archive are distributed as simple ASCII files, which can be directly analyzed without further reprocessing.

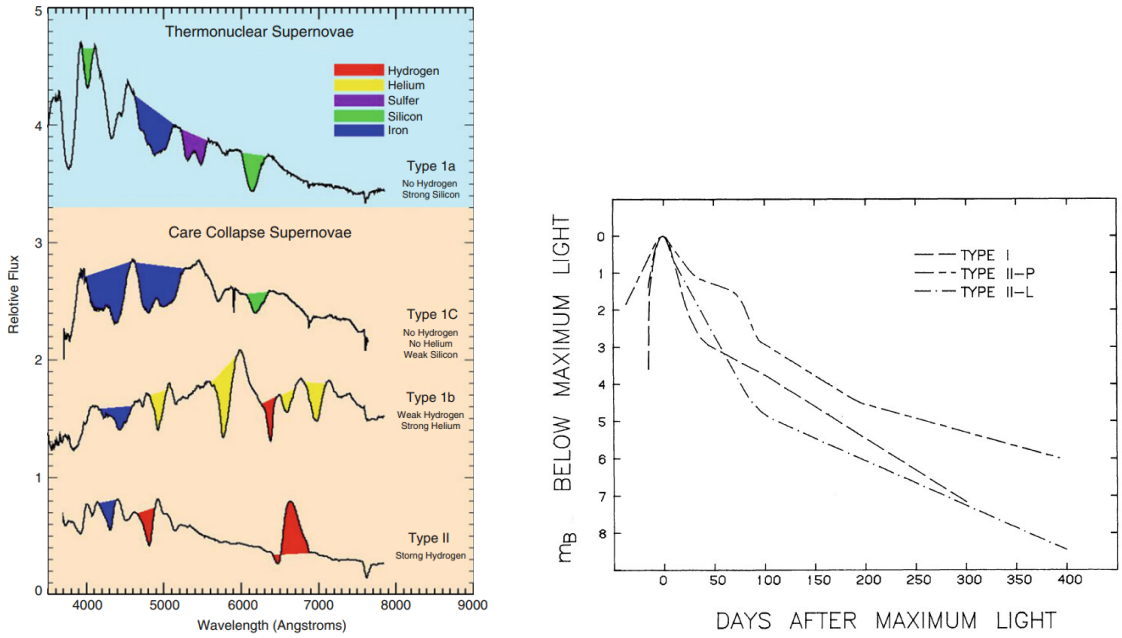

Figure 1.1: Left: Example SNe spectra near maximum light (Branch & Wheeler, 2017). Right: Example SNe light curves (Doggett & Branch, 1985).

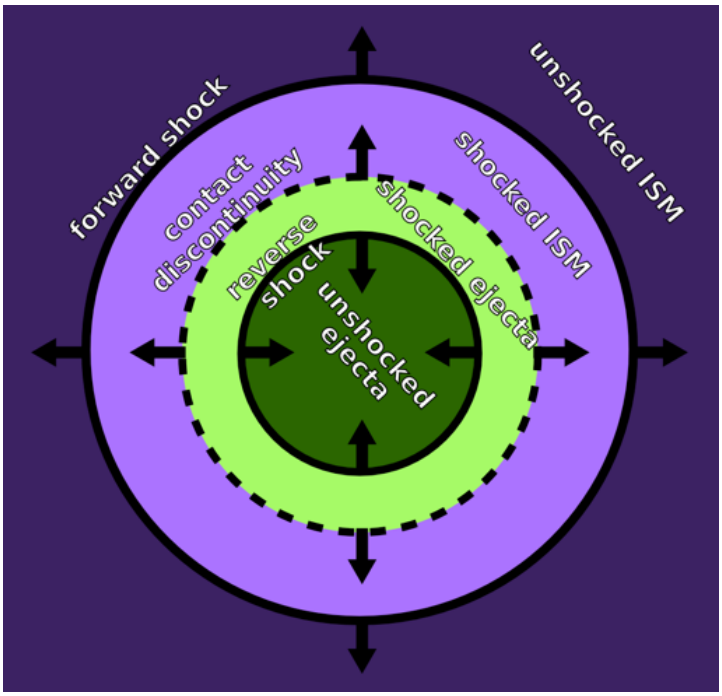

Figure 1.2: Cartoon diagram of a supernova remnant (Credit: https://www.cosmos.esa.int/documents/332006/2231234/GFerrand_t.pdf).

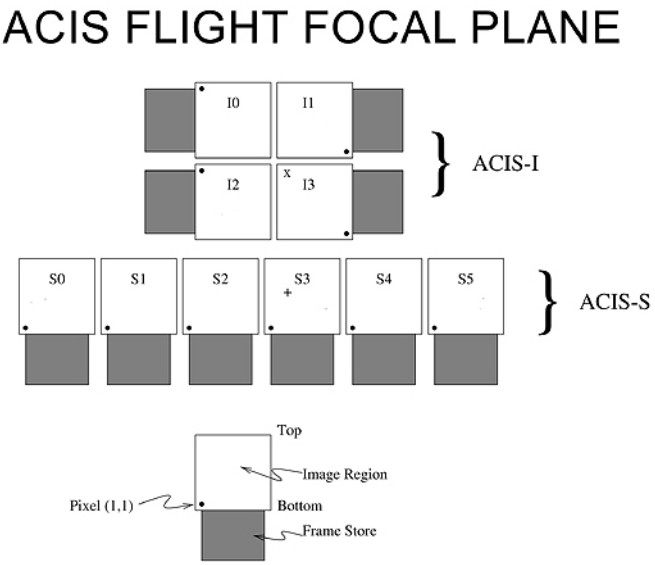

Figure 1.3: Schematic of Chandra ACIS array (https://chandra.harvard.edu/graphics/resources/illustrations.html)

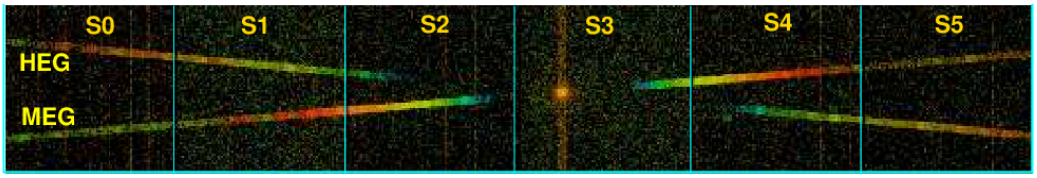

Figure 1.4: Dispersed 3–color HETG image of the bright star, Capella (https://cxc.harvard.edu/proposer/POG/html/chap8.html). Red, green, and blue colors represent high, medium, and low energy photons, respectively.

1.10 References

Ashworth, W. B., J. 1980, Journal for the History of Astronomy, 11, 1

Asplund, M., Amarsi, A. M., & Grevesse, N. 2021, A&A, 653, A141

Baade, W., & Zwicky, F. 1934, Physical Review, 46, 76

Branch, D., & Wheeler, J. C. 2017, Supernova Explosions, doi:10.1007/978-3-662-55054-0

Burkert, A. 2006, Comptes Rendus Physique, 7, 433

Burkey, M. T., Reynolds, S. P., Borkowski, K. J., & Blondin, J. M. 2013, ApJ, 764, 63

Carlton, A. K., Borkowski, K. J., Reynolds, S. P., et al. 2011, ApJL, 737, L22

Cesarsky, C. J., & Salama, A. 2006, ISO Science Legacy, Vol. 119

Chawner, H., Marsh, K., Matsuura, M., et al. 2019, MNRAS, 483, 70

Chevalier, R. A. 1977, ARA&A, 15, 175

Chiotellis, A., Schure, K. M., & Vink, J. 2012, A&A, 537, A139

Chugai, N. N., & Danziger, I. J. 1994, MNRAS, 268, 173

Clegg, P. E., Ade, P. A. R., Armand, C., et al. 1996, A&A, 315, L38

Coc, A., & Vangioni, E. 2010, in Journal of Physics Conference Series, Vol. 202, Journal of Physics Conference Series, 012001

De Looze, I., Barlow, M. J., Swinyard, B. M., et al. 2017, MNRAS, 465, 3309

Doggett, J. B., & Branch, D. 1985, AJ, 90, 2303

Fruscione, A., McDowell, J. C., Allen, G. E., et al. 2006, in Society of Photo-Optical Instrumentation Engineers (SPIE) Conference Series, Vol. 6270, Society of Photo-Optical Instrumentation Engineers (SPIE) Conference Series, ed. D. R. Silva & R. E. Doxsey, 62701V

Gal-Yam, A. 2017, in Handbook of Supernovae, ed. A. W. Alsabti & P. Murdin, 195

Gomez, H. L., Krause, O., Barlow, M. J., et al. 2012, ApJ, 760, 96

Guest, B. T., Blair, W. P., Borkowski, K. J., et al. 2022, ApJ, 926, 207

Hillebrandt, W., & Niemeyer, J. C. 2000, ARA&A, 38, 191

Howell, D. A., Sullivan, M., Nugent, P. E., et al. 2006, Nature, 443, 308

Hsi, T.-T. 1957, Smithsonian Contributions to Astrophysics, 2, 109

Janka, H.-T., Hanke, F., Hüdepohl, L., et al. 2012, Progress of Theoretical and Experimental Physics, 2012, 01A309

Kepler, S. O., Kleinman, S. J., Nitta, A., et al. 2007, MNRAS, 375, 1315

Kessler, M. F., Steinz, J. A., Anderegg, M. E., et al. 1996, A&A, 500, 493

Khokhlov, A. M. 1991, A&A, 245, 114

Li, J., Kastner, J. H., Prigozhin, G. Y., et al. 2004, ApJ, 610, 1204

Matsuura, M., Dwek, E., Barlow, M. J., et al. 2015, ApJ, 800, 50

Millard, M. J., Park, S., Sato, T., et al. 2022, submitted to ApJ

Millard, M. J., Ravi, A. P., Rho, J., & Park, S. 2021, ApJS, 257, 36

Millard, M. J., Bhalerao, J., Park, S., et al. 2020, ApJ, 893, 98

Miura, R. E., Espada, D., Hirota, A., et al. 2021, MNRAS, 504, 6198

Nozawa, T., Kozasa, T., Umeda, H., Maeda, K., & Nomoto, K. 2003, ApJ, 598, 785

Rho, J., Reach, W. T., Tappe, A., et al. 2009, ApJ, 700, 579

Rho, J., Gomez, H. L., Boogert, A., et al. 2018, MNRAS, 479, 5101

Sedov, L. I. 1959, Similarity and Dimensional Methods in Mechanics

Shen, K. J., Boubert, D., Gänsicke, B. T., et al. 2018, ApJ, 865, 15

Slavin, J. D., Dwek, E., Mac Low, M.-M., & Hill, A. S. 2020, ApJ, 902, 135

Taylor, G. 1950, Proceedings of the Royal Society of London Series A, 201, 159

Truelove, J. K., & McKee, C. F. 1999, ApJS, 120, 299

von Neumann, J. 1947, in Blast Wave, Los Alamos Sci. Lab. Rep., LA-2000, ed. H. A. Bethe, 27–55

Wheeler, J. C., & Harkness, R. P. 1990, Reports on Progress in Physics, 53, 1467

Wilk, K. D., Hillier, D. J., & Dessart, L. 2018, MNRAS, 474, 3187

Williams, B. J., & Temim, T. 2017, in Handbook of Supernovae, ed. A. W. Alsabti & P. Murdin, 2105

Williams, B. J., Borkowski, K. J., Reynolds, S. P., et al. 2014, ApJ, 790, 139

Wongwathanarat, A., Müller, E., & Janka, H.-T. 2015, A&A, 577, A48

Woosley, S. E., Heger, A., & Weaver, T. A. 2002, Reviews of Modern Physics, 74, 1015

Woosley, S. E., & Weaver, T. A. 1995, ApJS, 101, 181

CHAPTER 2

An Ejecta Kinematics Study of Kepler's Supernova Remnant with High-Resolution Chandra HETG Spectroscopy

2.1 Introduction

Type Ia supernova explosions are most likely the result of the unbinding of a WD which has accreted enough mass from a companion, either through a merger or matter stream (Iben & Tutukov, 1984), to burn carbon and oxygen (Hoyle & Fowler, 1960), resulting in a runaway thermonuclear explosion. The evolution of Type Ia SNRs may be modelled assuming a uniform ISM interaction(Badenes et al., 2007; Martínez-Rodríguez et al., 2018). However, asymmetries in ejecta distributions have been seen in some Type Ia SNRs (e.g., Uchida et al. (2013); Post et al. (2014)), indicating that the explosion environment is likely more complex. The explosion itself might not have been spherically symmetric (e.g., Kasen et al. (2009); Maeda et al. (2010, 2011)), and the initial non-uniformity in the SN ejecta may be caused by such an explosion asymmetry. If the WD is interacting with a non-degenerate companion star, the disk that would likely form around the accreting WD may produce a wind which could strip material from the companion, creating an anisotropic CSM (e.g., Hachisu et al. (2008)) surrounding the progenitor system. Such a modified medium could contain regions of varying density, which may slow down some of the ejecta from the SN explosion, while leaving other parts of the ejecta gas unaffected.

A well-known case where a Type Ia SNR is interacting with CSM is the remnant of SN 1604 (Kepler), the most recent Galactic historical supernova. As a young, ejecta-dominated remnant of a luminous (assuming a distance > 7 kpc) Type Ia SN

(Patnaude et al., 2012) from a metal-rich progenitor (Park et al., 2013), it provides an excellent opportunity to study the nature of a Type Ia progenitor and its explosion in the presence of CSM material (Burkey et al., 2013) and nitrogen-rich gas (Dennefeld, 1982; Blair et al., 1991; Katsuda et al., 2015). Strong silicate dust features observed in the infrared spectra of the remnant are indicative of the wind from an oxygen-rich AGB star (Williams et al., 2012). The distance to Kepler is uncertain; recent estimates put the distance from 3.9 kpc (Sankrit et al., 2005) to > 7 kpc (Patnaude et al., 2012; Chiotellis et al., 2012).

In X-rays, Kepler appears as mostly circular with an angular diameter of $\sim 3.6'$, however it does have curious morphological features. For example, there are two notable protrusions located in the east and west portion of the SNR, often referred to as "Ears" (Tsebrenko & Soker, 2013) (a similar case is G299.2-2.9 (Post et al., 2014)). Kepler also shows emission features from shocked CSM, one located across the center of the remnant and another which stretches across the northern rim (Burkey et al., 2013). Park et al. (2013) found a higher Ni to Fe K line flux ratio in the northern half than in the southern half of Kepler, but were not able to distinguish the origin for the differential Ni/Fe flux ratio (shock interactions with different CSM densities between the north and south versus an intrinsically different ejecta distribution between the north and south). Katsuda et al. (2008) found that the northern half was expanding more slowly than the southern half, suggesting an uneven ejecta distribution between the northern and southern shells, although they attributed the difference to interaction with a dense CSM in the north.

Measuring the Doppler shifts in the emission lines from the X-ray-emtting ejecta knots projected over the face of the SNR, and thus their bulk motion v_r is useful to reveal the 3-D structure of the clumpy ejecta gas. The velocity measurements of these knots may help to reveal the ejecta properties immediately after the explosion,

as well as their interaction with the circumstellar medium, which was formed by the progenitor system's mass loss history. Recently, Sato & Hughes (2017b) reported measurements of radial velocity for several compact X-ray-bright knots in Kepler's SNR using archival Chandra ACIS data. They measured high radial velocities of up to $\sim 10^4$ km s^{-1} and nearly free-expansion rates for some knots.

Here, we present the results of our study on 3-D velocity measurements of a sample of 17 small, bright regions in Kepler, based on high resolution X-ray spectroscopy from our Chandra HETGS observation. In Section 2.2, we present the observations we used for our analysis. In Section 2.3, we show our analysis techniques and results. In Section 2.4, we estimate the distance to Kepler and discuss its ejecta distribution based on our results, and in Section 2.5 we summarize our findings.

2.2 Observations

We performed our Chandra HETGS observation of Kepler using the ACIS-S array from 2016 July 20 to 2016 July 23. The aim point was set at RA(J2000) = $17^{\rm h}30^{\rm m}41^{\rm s}.3$, Dec(J2000) = -21°29′28″.9, roughly towards the geometric center of the SNR. The observation was composed of a single Observation Identifier (ObsID), 17901. We processed the raw event files using CIAO (Fruscione et al., 2006) version 4.10 and the Chandra Calibration Database (CALDB) version 4.7.8 to create a new level=2 event file using the CIAO command, `chandra_repro`. Next, we removed time intervals of background flaring using the Chandra Imaging and Plotting System (ChIPS) command, `lc_sigma_clip`, which left us with a total effective exposure of 147.6 ks. We then extracted the 1st-order dispersed spectra from a number of small regions across the SNR (Section 2.3.2) using the TGCat scripts (Huenemoerder et al., 2011) `tg_create_mask`, `tg_resolve_events`, and `tgextract`, and also created appropriate detector response files. The TGCat commands (in the order mentioned)

first create a FITS region file which specifies a region position, shape, size, and orientation in sky pixel-plane coordinates[1]. Next, event positions are compared with the 3-D locations at which dispersed photons can appear, given the grating equation and zero order position, and TGCat assigns them a wavelength and an order, and outputs these data into a grating events file[2]. Finally, the grating events file is filtered and binned into a one-dimensional counts spectrum for each grating part, order, and source[3]. In addition to our new HETGS data, we also used the archival ACIS data of Kepler as supplementary data (listed in Table 2.1). For spectral fitting purposes (Section 2.3.3), we reprocessed the six ObsIDs from the 2006 archival ACIS-S3 data by following standard data reduction procedures with CIAO versions 4.8 to 4.8.2 and CALDB version 4.7.2, which resulted in a total effective exposure of $\sim$ 733 ks. To make our proper motion measurements, we used the 2000, 2006, and 2014 archival Chandra ACIS data, as previously processed and prepared in Sato & Hughes (2017b).

2.3 Data Analysis and Results

2.3.1 Utility of HETGS for Extended Sources

Due to its dispersed nature, the Chandra HETGS (the 1st-order) is best suited to measure the spectra of isolated, point-like sources. The utility of the HETG spectrum is affected when the source is extended and/or surrounded by complex background emission features. Our study of Kepler is typical of such a case; the SNR comprises many small, discrete extended sources projected against its own complex diffuse emission. The HETG-dispersed image of Kepler is shown in Figure 2.1. Our goal is to measure the atomic line center energies in the X-ray emission spectrum

[1] http://cxc.harvard.edu/ciao/ahelp/tg_create_mask.html

[2] http://cxc.harvard.edu/ciao/ahelp/tg_resolve_events.html

[3] http://cxc.harvard.edu/ciao/ahelp/tg_extract.html

for small individual emission features within the SNR. For this type of measurement, the utility of HETG data have been successfully demonstrated by previous authors in the cases of Cassiopeia A (Cas A) (Lazendic et al., 2006) and G292.0+1.8 (G292) (Bhalerao et al., 2015). He-like Si Kα lines were used for Cas A, while He- and H-like Ne, Mg, and Si Kα lines were used for G292. In the integrated spectrum of Kepler, the Fe L and K, and He-like Si and S Kα lines are prominent. However, the Fe K line is faint in the spectra of individual small knots, and thus, not useful for our study. Additionally, the Fe L lines are a complex composed of several closely spaced emission lines, which makes it difficult to identify them for Doppler shift measurements, whereas the He-like Si Kα and S He-like Kα lines each may easily be represented by a simple trio of emission lines. Overall, ejecta knots in Kepler are fainter than those in Cas A and G292. Thus, the count statistics for most knots only allow us to use the brightest line, He-like Si Kα. In general, we found that at least $\sim$ 100 counts for the He-like Si Kα line emission features in the 1.75 - 1.96 keV band of the 1st-order MEG spectrum of each individual target source are required to make a reliable Doppler shift measurement.

Distinguishing the He-like Si Kα lines from the target emission knot from those of the surroundings is essential to correctly measure the line center energies of He-like Si Kα lines in the spectrum of small individual knots in Kepler. To quantitatively assess the contamination in the He-like Si Kα line profiles of the target source from the nearby emission features, as well as due to the target source extent, we performed ray-trace simulations of Chandra observations using the Model of AXAF Response to X-rays (MARX) package (Davis et al., 2012). Initially, we assumed a point-like target source with an X-ray spectrum representing the rest energy emission lines of He-like Si Kα, at various distances from the zeroth order position. Figures 2.2a and 2.2b show that the 1st-order spectral lines (He-like Si Kα) are shifted from the

true line center energies as the source position is off-centered, corresponding to the Chandra HETGS wavelength scale of 0.0113 Å/arcsec for HEG and 0.0226 Å/arcsec for MEG[4]. Using this relation, we may identify interfering emission lines in our source spectra originating from nearby sources. We also tested how the angular extent of the target sources affect our line center measurements. While larger source extents would increase the uncertainties in the line center energy measurements, we conclude that our radial velocity measurements would not be affected (within uncertainties) as long as the target source sizes are $\lesssim 10''$ (Figures 2.2c and 2.2d).

Based on our test simulations, we also conclude that nearby discrete sources positioned $\sim 25''$ or farther off the target source position along the dispersion direction would not affect our measurements of the source spectral line center energies for radial velocities. For the cases where nearby sources are present (with angular extent similar to that of the target source) within $\sim 25''$ of the target source along the dispersion direction, the effects on the line center measurements for the target source may vary. We investigated numerous source configurations (both with our actual data of Kepler and extensive MARX simulations), and found that even if the nearby source positions are relatively close to the target position, we may avoid a significant contamination from the nearby emission by adjusting the criteria for the selection of the 1st-order photons of the target spectrum via the "osort" parameters, *osort_lo* and *osort_hi*[5]. During HETG spectrum extraction, only photons with measured wavelengths that meet the criteria, $osort\_lo < \lambda_g/\lambda_{CCD} \leq osort\_hi$ are included in the 1st-order spectrum, where λ_{CCD} is the ACIS-S CCD wavelength, and λ_g is the gratings wavelength. Because λ_{CCD} and λ_g values of nearby sources become more divergent the farther they are located from the target position, photons from

[4]http://cxc.harvard.edu/proposer/POG/html/chap8.html

[5]See footnote 2

those nearby sources are less likely to be included in the extracted spectrum when small osort values are chosen. Thus, we may still be able to measure the source line center energies despite the presence of nearby contaminating emission features. However, we find it unlikely that the emission lines from sources located very near to each other ($\lesssim 5''$) along the dispersion direction, with similar brightness, would be properly distinguishable.

2.3.2 Radial Velocities

Based on archival Chandra ACIS data (Table 2.1), we identified numerous small emission features which are bright in the 1.7 - 2.0 keV band, suggesting that they may be good candidate targets for He-like Si Kα line center energy measurements using an HETG 1st-order spectrum. We selected 17 features (Figure 2.3), generally satisfying the criteria that we discussed in Sec 2.3.1. To measure the v_r of these X-ray emission features projected within the boundary of Kepler, we adopt a similar method to those pioneered by Lazendic et al. (2006) and Bhalerao et al. (2015), who analyzed HETG spectra of bright X-ray knots in SNRs Cas A and G292, respectively. For each of these 17 individual features, we extracted the 1st-order spectrum from our Chandra HETGS observation.

For each extracted region, the line center energies of the He-like Si Kα lines, and two Si XII emission lines (see below), were measured by fitting six Gaussian curves to the spectrum - three for He-like Si Kα, two for the Si XII emission lines, and one for the background continuum using the Interactive Spectral Interpretation System (ISIS) software package (Houck & Denicola, 2000). The measured line center wavelengths were then compared with the rest values (6.648 Å for resonance, 6.688 Å for intercombination, 6.740 Å for the forbidden line, and 6.717 Å and 6.782 Å for

the Si XII lines, respectively (Drake, 1988)), to measure the Doppler shifts in these lines, and thus to estimate the corresponding v_r.

The count statistics of our data do not allow us to directly measure the He-like Si (XIII) Kα intercombination to resonance (i/r) and forbidden to resonance (f/r) resonance line flux ratios. Thus, we use i/r and f/r ratios which correspond to the values that we measured for each knot using archival ACIS data (Section 2.3.3). At the temperatures and ionization timescales that we measure for the knots in our sample, Si XII emission lines at $\sim$ 6.717 Å and $\sim$ 6.782 Å may also contribute significantly to the spectrum. Thus, we account for these lines in our v_r fitting model. In Appendix A, we discuss the effects of varying line ratios on our v_r estimates. In general, the uncertainty in line ratio values does not affect our conclusions.

Our results are summarized in Table 2.2, with spectra and best-fit models shown in Figure 2.4. Errors represent a 90% confidence interval unless otherwise noted. Figure 2.3 shows the locations of blueshifted and redshifted regions, marked by cyan and red circles, respectively. Our measured v_r for two CSM regions (regions C2* and C4*) are negligible even though they are projected near the SNR center. This low v_r is perhaps as expected for the shocked CSM features regardless of their projected distance from the SNR center, supporting the reliability of our v_r measurements. Of the 15 ejecta knots for which we measured v_r, only two (N5 and Ear3) show a significantly blueshifted spectrum, while the other eight regional spectra are significantly redshifted.

We note that four ejecta knots in our sample (regions N2, N1, N3, and N7) were also studied in Sato & Hughes (2017b), who measured the v_r of these ejecta knots based on Chandra ACIS data. For three of these common regions, N2, N1, and N3, we measure high v_r values ($v_r \sim$ 5600 - 7700 km s^{-1}). These regions are located in the northern shell of the SNR, approximately 1$'$ from the kinematic center (R.A.(J2000)

= 17^{h} 30^{m} $41^{s}.321$ and Declination(J2000) = -21° 29′ 30″.51 (Sato & Hughes, 2017b)). For all four of our common knots, we find general agreement between our measured values and those from Sato & Hughes (2017b), as shown in Table 2.2. This is an interesting result when we consider that the v_r measurements based on the low-resolution ACIS spectrum are dominated by systematic uncertainties ($\sim$ 500 - 2,000 km s^{-1}) (Sato & Hughes, 2017a,b), while those using our high-resolution HETGS spectrum are mostly dominated by statistical uncertainties (due to the relatively lower throughput of the dispersed spectroscopy), yet our results for those four ejecta regions are consistent. Almost all other ejecta knots show significantly lower velocities of $v_r \lesssim 2300$ km s^{-1} (Table 2.2). It is notable that two ejecta knots (regions Ear1 and Ear2) projected within the western "Ear" region show a significant v_r ($\sim$ 2200 and 900 km s^{-1}) even though they are projected far ($\sim 2'$) from the center of the remnant beyond the main shell of the SNR.

2.3.3 Identifying Metal-Rich Ejecta

The extremely fast expansion of SNRs results in strong shocks being driven into the surrounding gas. The gas that encounters the shock is forced out of ionization equilibrium. In SNRs, the densities are so low that very few collisional ionizations will occur quickly after the plasma is shocked. Thus, the shocked plasma will take time to reach its new ionization state. This is called non-equilibrium ionization (NEI). The ion fraction for each species in the shocked plasma changes with temperature, time, and electron density. The NEI conditions are generally solved for in terms of the electron temperature (kT, where k is the Boltzmann constant and T is electron temperature), and ionization timescale ($n_e t$: the electron density, n_e, multiplied by the time since being shocked, t). Ionization states are lower in NEI conditions than those in collisional-equilibrium ionization (CIE) at similar temperatures.

To identify the origin of small emission regions in our sample (metal-rich ejecta vs low-abundant CSM), we performed spectral model fits for each individual regional spectrum based on the archival Chandra ACIS data with the deepest exposure (combining all ObsIDs taken in 2006, with a total exposure of 733 ks). We fitted the observed 0.3-7.0 keV band ACIS spectrum extracted from each region with an absorbed X-ray emission spectral model assuming optically-thin hot gas in NEI (`phabs*vpshock` (Borkowski et al., 2001)) using the XSPEC software package (Arnaud, 1996). We estimated the background spectrum with small faint diffuse emission regions nearby each source region within the SNR. Then, we subtracted the background spectrum from the source regional spectrum before the spectral model fitting. We allowed the electron temperature, ionization timescale, redshift, normalization, and abundances of O, Ne, Mg, Si, S, Ar, and Fe to vary in our spectral model fitting. We fixed all other elemental abundances at solar values (Wilms et al., 2000). We note that, although H and He are generally not expected to be abundant in the spectrum of ejecta-dominated emission features of Type Ia SNRs, Kepler is interacting with a significant amount of CSM. Thus, we leave the H and He abundances fixed at solar values in our model to account for possible CSM interaction throughout the SNR. In the ejecta-dominated knots, we also use the H and He continuum as an approximation for non-thermal power-law emission from the shock-accelerated electrons at the forward shock. We fixed the absorption column to $N_{\rm H} = 5.4 \times 10^{21}$ cm^{-2} (Foight et al., 2016). We found significant residuals at $E \sim 0.75$ and ~ 1.25 keV in the spectra of the ejecta knots. Similar features have been noticed in several other SNR studies of ejecta-dominated (particularly Fe-rich) spectra (Hwang et al., 1998; Katsuda et al., 2015; Sato & Hughes, 2017b; Yamaguchi et al., 2017). To improve our spectral model fits, we added gaussian components at these energies to account for these emission line features of the ejecta knot spectra (adding these gaussian components

does not significantly improve the spectral model fit of the CSM-dominated regions, and thus, were not included in those fits). We note that this implementation is not physically motivated, and is only intended as a statistical improvement in the spectral model fits. We confirm that excluding these gaussians does not affect our conclusions (distinguishing between ejecta-dominated and CSM-dominated regions, as discussed later). Our reduced chi-squared values for the best-fit models range from $\chi^2_\nu = 1.0$ - 1.4.

Given that Si and Fe are the most efficiently produced elements in a Type Ia explosion, we identified our knots as CSM-dominated or ejecta-dominated based on our measured abundances of Si and Fe. Knots with low Si and Fe abundances relative to solar values, $[\mathrm{Si/Si_\odot}] \lesssim 1.5$ and $[\mathrm{Fe/Fe_\odot}] \lesssim 1$, were deemed CSM-dominated, while those which have an enhanced abundance $[\mathrm{Si/Si_\odot}] \gtrsim 3$, and $[\mathrm{Fe/Fe_\odot}] > 1$, were classified to be ejecta-dominated. This way, we identified 15 knots as ejecta-dominated and two knots as CSM-dominated. The best-fit electron temperatures of nearly all ejecta knots in our sample are $kT \sim 2$ - 5 keV, with ionization timescales $n_e t \sim 1$ - 3×10^{10} cm^{-3} s. The medians of these best-fit kT and $n_e t$ ejecta values generally agree with the higher-temperature ejecta components measured by Katsuda et al. (2015). For three ejecta-dominated knots, S2, N7, and Ear1, and for the CSM-dominated knots, we measure lower temperatures ($kT \sim 0.5$ - 1.3 keV) and higher ionization timescales ($n_e t \sim 5 \times 10^{10}$ - 10^{12} cm^{-3} s). We attribute the outlying kT and $n_e t$ observed in these three ejecta knots to possible CSM interaction. The spectral fitting results are summarized in Table A.1 in the Appendix.

2.3.4 Proper Motions

Based on the archival Chandra ACIS data covering the net time-span of 14 years (2000-2014, Table 2.1), we estimate the proper motions of the small ejecta regions for

which we measure v_r. To measure the proper motions, we apply the methods used in Sato et al. (2018). We took the image from the long observation in 2006 as the reference "model" for each knot, compared it to the images from other epochs by incrementally shifting it in R.A. and declination, and then calculated the value of the Cash statistic (Cash, 1979),

$$C = -2 \sum_{i,j} (n_{i,j} \ln m_{i,j} - m_{i,j} - \ln n_{i,j}!), \tag{2.1}$$

where $n_{i,j}$ and $m_{i,j}$ are the number of counts in the i^{th}, j^{th} pixel from the current epoch, and in 2006, respectively, scaled by the total number of counts in the SNR. When the Cash statistic reached a minimum value, it means the pixel values in the image for each "test" epoch most closely matched those found in the reference image, indicating that its position in the test epoch was determined. We estimate the error in the parameters using $\Delta C = C - C_{min}$, which may be interpreted in a way similar to $\Delta\chi^2$, and also include the systematic image alignment uncertainty from each epoch (Sato & Hughes, 2017b). The results of our proper motion measurements are summarized in Table 2.2. Our measured proper motions range $\mu_{R.A.} \sim$ -0.17″ yr^{-1} to 0.17″ yr^{-1} in R.A. and $\mu_{Dec} \sim$ -0.12″ yr^{-1} to 0.14″ yr^{-1} in declination. Figure 2.5 shows zoom-in images of knots, demonstrating their positional changes over 14 years. Knot Ear2, projected within the western Ear of Kepler shows the largest proper motion, $\mu_{Tot} \sim 0.20''$ yr^{-1}, which is perhaps as expected, considering that it is an ejecta knot projected beyond the main shell of Kepler. The CSM-dominated regions generally show negligible proper motions, which may also be expected.

Sato & Hughes (2017b) found that ejecta knots with the highest v_r (N2, N1, N3) tend to show proper motions close to their extrapolated time-averaged rates for the change of angular positions, μ_{Avg} (their angular distance from the SNR center estimated by Sato & Hughes (2017b) divided by the age of Kepler, 412 years as

of 2016), suggesting that they have not undergone significant deceleration since the explosion (i.e. they are nearly freely expanding). From here on we refer to μ_{Tot}/μ_{Avg} as the expansion index, η. If an ejecta knot has been moving undecelerated since the explosion, we may expect $\eta \approx 1$. We find several ejecta knots to have an expansion index close to 1 ($\eta \gtrsim 0.7$, see Table 2.2). We note that region C3 is an anomaly with $\eta = 1.86$. This discrepancy is probably due to its projected proximity to the SNR center. The angular offset of C3 from the SNR center is similar to the uncertainties on the SNR center position, and, in fact, η is not constrained (Table 2.2). Knot C2* also shows a high η value, and is projected near the center of the SNR with a large uncertainty in η (± 0.3). Its spectrum is clearly CSM-dominated and its low proper motion is consistent with a CSM origin. In general, CSM-dominated regions are not expected to have a high η value. The source of this discrepancy is unclear, however, we speculate that this dense filament of CSM-dominated gas may have been ejected from the progenitor system shortly before the SN explosion took place. Thus, like other parts of the remnant, it has possibly only been traveling for $\sim$ 400 years.

2.4 Discussion

2.4.1 Distance to Kepler

The kinematic nature of ejecta knot N2 in Kepler is remarkable. Sato & Hughes (2017b) measured an expansion index $\eta \sim 1$, indicating that it is almost freely-expanding. Here, we measure a similarly high expansion index, and a high v_r (nearly 8,000 km s^{-1}). In general, X-ray-emitting ejecta features in SNRs are expected to be heated to $T > 10^6$ K by the reverse shock, being somewhat decelerated in the process. To explain the existence of nearly freely-expanding ejecta knots in Kepler, Sato & Hughes (2017b) used the findings from Wang & Chevalier (2001) to argue

that these ejecta knots may have survived to the current age of Kepler ($\sim$ 400 years) if their initial density contrast to the surrounding medium was high ($\gtrsim$ 100). Alternatively, they suggested that the highly-structured environment of the remnant contains low density ($n_H \sim 0.1$ cm^{-3}) "windows" through which some ejecta knots may have traveled. This causes a late encounter with the reverse shock, allowing for the survivability of lower density-contrast, nearly undecelerated knots to the forward shock region, according to the simulations of Wang & Chevalier (2001). This is the scenario favored by Sato & Hughes (2017b). Either scenario may be applied in the interpretation of our results. Considering that Kepler is located hundreds of parsecs out of the Galactic plane where the ambient density is $n_H \lesssim 0.01$ cm^{-3} (McKee & Ostriker, 1977), the existence of low density regions around the SN site appears to be plausible.

Since we know the exact age of the SNR, and we have measured the radial velocity and the projected angular distance from the center of the remnant, only the inclination angle of the nearly freely-moving knot's velocity vector against the line of sight needs to be constrained in order to estimate the distance. There are ejecta-dominated regions projected close to the outermost boundary of the main shell (e.g. N7) and even beyond it (Ear2). These knots show smaller expansion indices (i.e. stronger deceleration) than N2, while N2 has an apparent nearly constant proper motion since the explosion, and unusually high v_r. The forward shock itself has significantly decelerated: Vink (2008) and Katsuda et al. (2008) found an average expansion parameter of $\sim$ 0.5 to 0.6. Hence, it seems likely that N2 may have reached near or even beyond the main shell, similar to ejecta "bullets" reported in other SNRs (e.g., Strom et al., 1995; Park et al., 2012; Winkler et al., 2014).

Depending on the location of N2, the inclination angle for its space velocity vector against the line of sight may be constrained. We assume three cases for the

physical location of N2: 1) at the outermost boundary of the SNR's main shell (the projected angular distance from the SNR center $D \sim 1.8'$), 2) at the physical distance corresponding to the angular distance (from the SNR center) to the western Ear's outermost boundary, i.e., the visible maximum angular extent of the X-ray emission ($D \sim 2.3'$), and 3) a location significantly beyond the main SNR shell at the distance corresponding to ~ 1.5 times the radius of the SNR's main shell ($D \sim 2.7'$). The expansion center of Kepler's SNR has been estimated in radio wavelengths by Matsui et al. (1984) and DeLaney et al. (2002), and later in X-rays by Katsuda et al. (2008) and Vink (2008). Recently, Sato & Hughes (2017b) estimated two possible expansion centers by tracing back the proper motion of a few ejecta knots with high expansion indices to a common origin, one assuming no deceleration, and the other a power-law evolution of radius with time (i.e., deceleration). We take the "decelerated" kinematic center estimated by Sato & Hughes (2017b) as the explosion site unless otherwise noted. We may calculate the distance to Kepler by considering that N2 has been moving with our measured v_r along the line of sight since the explosion. This approach would almost certainly result in an underestimate of the true distance, however since we are in general more interested in a lower limit to the distance, this assumption would not affect our conclusions.

In scenarios 1, 2, and 3, we assume that N2 has reached the main shell of the remnant, or beyond, and thus we estimate distances of $d \sim 7.5$ kpc, ~ 5.4 kpc, and ~ 4.4 kpc, respectively. Recently, Ruiz-Lapuente (2017) interpreted historical light curves of SN 1604, and Sankrit et al. (2016) used proper motion and line width measurements of Balmer filaments to independently estimate a distance range, $d \sim 5.1 \pm 0.8$ kpc to Kepler. Our distance range is generally consistent with this value, and also with somewhat farther distance estimates which suggest an energetic Type Ia explosion for SN 1604 (Aharonian et al., 2008; Vink, 2008; Chiotellis et al., 2012;

Patnaude et al., 2012; Katsuda et al., 2015). Considering the amount of ^{56}Ni required to explain the bulk properties of the X-ray spectrum, the spectral and hydrodynamical fitting done by Patnaude et al. (2012) and Katsuda et al. (2015) suggests that the data are incompatible with a normal Type Ia explosion, but may be consistent with a DDTa model, which is more energetic. Since the age is known, this places the SNR at a distance of > 5 kpc. However, Ruiz-Lapuente (2017) argues that the best-fit stretch factor to the historical light curve indicates that it is more consistent with a normal Type Ia SN. Considering that our estimated lower limit (scenario 3) is likely to be conservative, and unless we have a relatively unique viewing angle, it is reasonable that knot N2 is located nearby, or less than, a distance from the center of the remnant described in scenario 2. Thus, we may conclude that our v_r measurement suggests $d \gtrsim 5$ kpc, and hence tends to favor the distance estimates which suggest an energetic Type Ia explosion for SN 1604.

Although it may not be favored due to our measured high proper motion and v_r, for completeness, we may consider that even the fastest ejecta knots (e.g., N2) in Kepler have been significantly decelerated rather than nearly freely expanding. In this scenario, the ejecta knot is heated between the forward and reverse shocks as expected by standard SNR dynamics (Chevalier, 1982), and it would be traveling generally with the bulk of ejecta gas in the SNR. With this configuration, a longer distance to Kepler is implied ($d \sim 11.0$ kpc), which we may consider to be a conservative upper limit.

2.4.2 Velocity Distribution of Ejecta

Based on our v_r and proper motion measurements, we measure space velocities, $v_s \sim$ (1,100 - 8,700)d_6 km s^{-1} (with d_6 in units of 6 kpc), with an average velocity, $v_s \sim$ 4,600d_6 km s^{-1}, for the 15 individual ejecta knots. The fastest known stars in the Milky Way (which are probably ejected from SN explosions in WD binaries)

show space velocities of $\sim$ 2,000 km s^{-1} (Shen et al., 2018). Thus, the velocities we obtain for several knots are highly significant, and cannot be attributed to a systemic velocity for the SNR.

The broad range of ejecta space velocities and expansion indices (see Table 2.2) that we measure in our sample may be characteristic for an SNR transitioning from the free-expansion to Sedov-Taylor phase. Measurements of the proper motion at various locations along Kepler's forward shock by Katsuda et al. (2008) and Vink (2008) found expansion indices of 0.47 - 0.82 and 0.3 - 0.7, respectively. For remnants nearing the Sedov-Taylor phase, Chevalier (1982) estimated $\eta = 0.4$ for $s = 0$ and $\eta = 0.67$ for $s = 2$ ambient density power-law solutions. Hence, our ejecta velocity measurements and previous forward shock analyses apparently suggest that the kinematics for some regions in Kepler may be dominated by nearly free-expansion, while others are better described by Sedov-Taylor dynamics. New 3-D hydrodynamical simulations that focus on Kepler and these high η knots may give some insight into their origin.

The knots N2, N5, N1, and N3 have the highest measured space velocities (6,100 - 8,700d_6 km s^{-1}), and are all located in the "steep arc" (DeLaney et al., 2002) of Kepler's SNR, a "bar" of bright X-ray emission which runs from east to west, located about halfway between the center of the remnant and the outer edge of the main shell. They are projected close to each other within a small ($50'' \times 20''$) area. This proximity, and similarities in their measured Si abundances, space velocity vectors, and expansion indices, suggest that these knots might have originated generally from a "common" layer of the exploding WD. Sato & Hughes (2017b) measured properties of another knot (they label "N4") projected within the steep arc, which exhibited similar properties to N2, N5, N1, and N3. This suggests that ejecta within the steep arc have generally homogeneous kinematic and spectroscopic properties.

In the western Ear, we measure high space velocity in region Ear2, $v_s \sim 5{,}800\,d_6$ km s^{-1}. Such a high velocity may be expected considering the knot's projected location in the western Ear feature which protrudes out about 30% beyond the main shell. Interestingly, knot Ear1 has a significantly smaller space velocity, $v_s \sim 3{,}300\,d_6$ km s^{-1}, even though it is projected very close to the position of Ear2. Knot Ear1 may be interacting with a CSM-dominated feature identified by Burkey et al. (2013) projected adjacent to it, which could have caused it to significantly decelerate recently. Such an interaction between ejecta and CSM may produce Hα emission. We searched for Hα emission at the location of Ear1 in the archival Hubble Space Telescope images (with the F656N filter) of Kepler (Sankrit et al., 2016). We found a faint wisp centered at Ear1's position, possibly indicating the presence of shocked CSM gas, which would support our conclusion of an ejecta-CSM interaction there.

Considering their spatial proximity and similarly high Si abundance, it seems likely that Ear1 and Ear2 were produced very near to each other during the SN. It is interesting that these knots are projected $\sim 1'$ in decl. north of the center of the remnant, as are the ejecta knots in the steep arc. In our distance estimation, we assumed that knot N2 is located at or beyond the main shell. Thus, if we viewed Kepler at a different angle, it may appear as though the steep arc and western Ear are similar structures extending to different directions. This morphological interpretation may not be consistent with the bipolar-outflow scenario (Tsebrenko & Soker, 2013) as the origin of the Ears. However, we measured generally higher Si abundances in the western Ear than in the steep arc (roughly by a factor of ~ 5), as did Sun & Chen (2019), who recently reported a similar result. This abundance discrepancy is not in line with the scenario that the Ear and arc features share a common physical origin. Thus, while we find intriguing similarities in kinematic properties between these substructures of Kepler, their true physical origins remain unanswered. Detailed

hydrodynamic simulations may be needed to test these scenarios, which are beyond the scope of this work.

The HETG spectra of ten ejecta regions from our sample show a significant Doppler shift (i.e., $|v_{\rm r}| \gtrsim 10^3$ km s^{-1}). The majority of them (eight regions) are redshifted. This may suggest a significantly asymmetric velocity distribution of ejecta knots along the line of sight (see Figure 2.6). However, we note that our sample size of the ejecta knots is limited. In particular, our sample regions offer very little coverage in the southern shell of the SNR. Thus, the apparent asymmetric ejecta distribution along the line of sight might have been a selection effect. To make a conclusive statement regarding the overall 3-D distribution of Si-rich ejecta in Kepler, a significantly larger sample of high-resolution velocity measurements from ejecta regions across the entire face of the SNR is required. A significantly deeper Chandra HETG observation would be needed to achieve this. Nonetheless, it is interesting to note that some similar uneven ejecta distributions have been reported in studies using the lower-resolution X-ray CCD spectroscopy from archival Chandra ACIS data. Sato & Hughes (2017b) found that only two ejecta-dominated knots out of the eleven (four in common with this work) included in their study were significantly blue-shifted. Those regions show relatively weak He-like Si Kα emission line fluxes, and thus, we could not measure their v_r using our HETGS data due to low photon count statistics. Kasuga et al. (2018) reported that a general asymmetry exists in the Fe-rich ejecta along the line of sight in Kepler. Burkey et al. (2013) suggested that the asymmetry in Fe ejecta across the face of the SNR could be a result of ejecta being blocked by the progenitor's companion star. While our results suggesting an uneven line-of-sight ejecta distribution cannot be conclusive based on the current data, previous studies of Kepler appear to be consistent with our results.

The suggested asymmetric distribution of the ejecta (if it is confirmed) could be the result of Kepler's interactions with its nonuniform surroundings. Patnaude et al. (2012) and Blair et al. (2007) argued that the north-south density gradient they found in the surrounding medium of Kepler is required to explain the observed bowshock in the north of the remnant, and the infrared intensity variation between the northern and southern rims. Such a density gradient across the near and far sides of the remnant, with surrounding material on the near side having a lower density on average, could lead to an under-developed or late reverse shock, causing blueshifted knots to appear fainter. Alternatively, the tentative asymmetric ejecta distribution along the line of sight might have been caused by a true asymmetry in the SN explosion itself. The global asymmetry in Type Ia SNe may in general be caused by the strength and geometry of ignition of the SN explosion (Maeda et al., 2010). The validity and true nature of the asymmetric ejecta distribution in Kepler's SNR that we observe in the Chandra data are unclear due to our small sample size. Follow-up Chandra HETGS observations of Kepler with deeper exposures would be warranted to perform a more extensive census of the ejecta velocity distribution (significantly beyond the capacity of the existing ACIS and HETG data) throughout the entire SNR, which is required to reveal the true 3-D nature of Kepler's SN explosion.

2.5 Conclusions

We have measured the radial velocities and proper motions of 17 small emission features (15 ejecta and 2 CSM knots) in Kepler's supernova remnant using our Chandra HETGS observation and the archival Chandra ACIS data. We find that a handful of knots are moving at speeds approaching $\sim 10^4$ km s^{-1}, with expansion indices approaching $\eta \sim 1$, indicating nearly a free expansion. Based on our radial velocity measurement of such a fast-moving ejecta knot, we estimate the distance to

Kepler. While our distance estimates may vary depending on our assumption of the degree of deceleration of the ejecta knot ($d \sim 4.4$ - 7.0 kpc), a relatively long distance of $d > 5$ kpc is favored. Our estimated distance range generally supports an energetic Type Ia SN for Kepler.

We note that most of our v_r measurements indicate a redshifted spectrum, suggesting an asymmetry in the along-the-line-of-sight ejecta distribution of the remnant. However, this study involves only a small sample of ejecta knots, most of which are projected in the northern shell of the SNR. Thus, while it provides hints into some intriguing kinematic characteristics of the Type Ia SN explosion which created Kepler, this work is limited in revealing the true 3-D structure of the entire SNR. A longer observation of Kepler using the Chandra HETGS would be required to measure v_r for a significantly larger number of ejecta knots covering the entire face of the SNR. Such measurements would yield a detailed picture of the 3-D distribution of ejecta, and provide observational constraints for more realistic Type Ia SN models.

Table 2.1. Archival Chandra ACIS Observations

Observation ID	Start Date	Exposure Time (ks)
116	2000-06-30	48.8
4650	2004-10-26	46.2
6714	2006-04-27	157.8
6715	2006-08-03	159.1
6716	2006-05-05	158.0
6717	2006-07-13	106.8
6718	2006-07-21	107.8
7366	2006-07-16	51.5
16004	2014-05-13	102.7
16614	2014-05-16	36.4

Table 2.2. Radial Velocity and Proper Motions of Small Emission Features in Kepler's SNR

Region†	R.A.[a] (degree)	Dec[a] (degree)	D[b] (arcmin)	v_r (km s^{-1})	$v_{r(SH)}$[c] (km s^{-1})	μ_{RA} (arcsec yr^{-1})	μ_{Dec} (arcsec yr^{-1})	μ_{Tot}[d] (arcsec yr^{-1})	η[e] (km s^{-1})	v_s[f]
N2	262.67314	-21.474812	1.02	7684^{+1155}_{-1177}	9110^{+30}_{-110}	0.028 ±0.017	0.137 ±0.024	0.140 ±0.029	0.94±0.14	8656^{+1093}_{-1112}
N1	262.68120	-21.476634	1.04	6019^{+1294}_{-1385}	8700^{+650}_{-470}	-0.065 ±0.016	0.081 ±0.024	0.104 ±0.028	0.68±0.10	6707^{+1213}_{-1291}
N3	262.66648	-21.480553	0.74	5550^{+2253}_{-2172}	5880^{+690}_{-1750}	0.045 ±0.016	0.078 ±0.024	0.090 ±0.028	0.83±0.16	6113^{+2073}_{-2000}
C3	262.67403	-21.491796	0.10	2281^{+1449}_{-1337}		0.019 ±0.018	-0.021 ±0.024	0.028 ±0.03	1.86±2.64	2416^{+1397}_{-1293}
N4	262.66124	-21.478912	0.98	2252^{+1761}_{-1664}		0.061 ±0.017	0.105 ±0.027	0.121 ±0.032	0.85±0.13	4115^{+1229}_{-1187}
Ear1	262.64352	-21.478218	1.79	2180^{+778}_{-752}		0.067 ±0.016	0.059 ±0.024	0.089 ±0.029	0.34± 0.03	3342^{+806}_{-795}
C1	262.67997	-21.502758	0.79	1823^{+1408}_{-1458}		-0.058 ±0.017	-0.064 ±0.024	0.086 ±0.029	0.75± 0.14	3052^{+1070}_{-1094}
Ear2	262.64087	-21.477378	1.95	942^{+525}_{-546}		0.172 ±0.017	0.104 ±0.024	0.201 ±0.029	0.71± 0.05	5798^{+819}_{-819}
N6	262.66920	-21.465973	1.56	883^{+954}_{-933}		0.002 ±0.018	0.141 ±0.024	0.141 ±0.03	0.62± 0.06	4109^{+859}_{-858}
E	262.70386	-21.495295	1.78	531^{+1551}_{-1269}		-0.171 ±0.016	-0.051 ±0.024	0.179 ±0.029	0.69± 0.06	5122^{+837}_{-831}
C2*	262.67685	-21.497011	0.41	-175^{+672}_{-700}		-0.047 ±0.016	-0.013 ±0.024	0.049 ±0.028	0.83± 0.30	1406^{+795}_{-796}
N7	262.65918	-21.466017	1.71	-225^{+382}_{-398}	244^{+46}_{-10}	0.026 ±0.015	0.026 ±0.023	0.037 ±0.028	0.15±0.01	1077^{+783}_{-784}
C4*	262.66782	-21.489190	0.29	-233^{+803}_{-862}		0.004 ±0.015	0.004 ±0.023	0.006 ±0.028	0.14± 0.07	289^{+801}_{-840}
S1	262.66758	-21.517109	1.54	-246^{+897}_{-882}		-0.033 ±0.018	-0.070 ±0.024	0.077 ±0.03	0.34± 0.03	2205^{+854}_{-854}
S2	262.66207	-21.512892	1.38	-536^{+1060}_{-1067}		0.058 ±0.017	-0.120 ±0.024	0.133 ±0.029	0.66± 0.07	3823^{+831}_{-831}
Ear3	262.63949	-21.488767	1.83	-2239^{+1087}_{-973}		0.140 ±0.016	0.018 ±0.024	0.141 ±0.03	0.53± 0.04	4595^{+915}_{-884}
N5	262.68243	-21.475636	1.13	-6716^{+1535}_{-1613}		-0.054 ±0.018	0.077 ±0.024	0.094 ±0.03	0.57± 0.07	7229^{+1461}_{-1531}

* CSM-dominated knot.

[a] Position in 2016 (J2000).

[b] Projected angular distance from kinematic center estimated by Sato & Hughes (2017b); R.A.(J2000) = $17^{\rm h}$ $30^{\rm m}$ $41^{\rm s}.321$ and Declination(J2000) = -21° 29′ 30″.51, with uncertainties of $\sigma_{R.A.} = \pm\ 0.073'$ and $\sigma_{Dec} = \pm\ 0.072'$, respectively.

[c] Values taken from Sato & Hughes (2017b). Errors represent a 68% confidence interval.

[d] $\mu_{Tot} = \sqrt{\mu^2_{R.A.} + \mu^2_{Dec}}$.

[e] Expansion index (see Section 2.3.4).

[f] Estimated space velocity for a distance of 6 kpc.

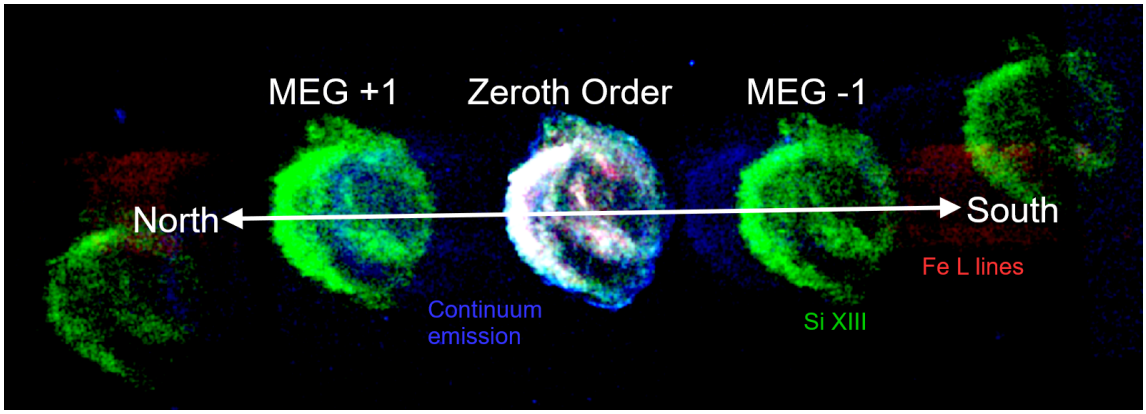

Figure 2.1: Chandra HETG 3-color image of Kepler. Red: 0.7-1.2 keV, Green: 1.7-2.0 keV and Blue: 2.0-8.0 keV. The Fe L complex and continuum emission appear smeared across the ACIS-S chips, the former because it consists of many emission lines, and the latter because it lacks individual emission lines. The Si XIII (He-like Si Kα) emission is more focused on the detector, because it consists only of three closely spaced lines at $\sim$ 1.865 keV

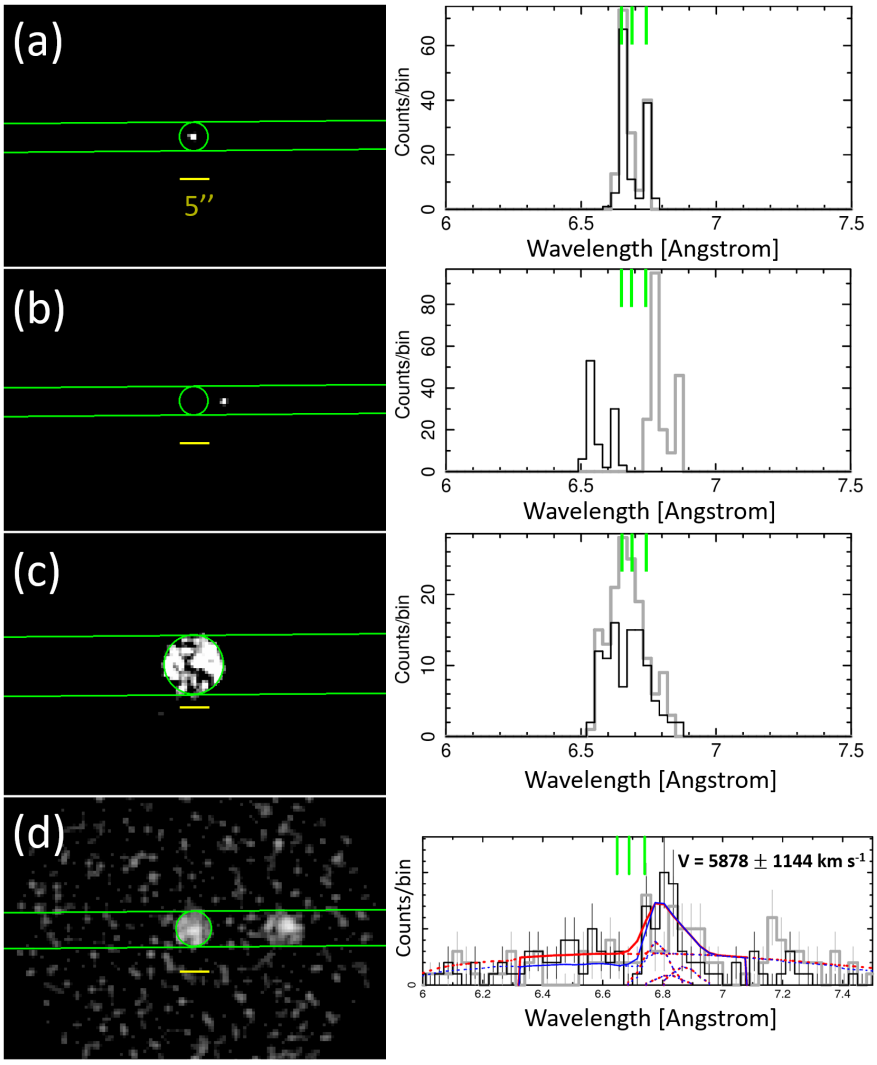

Figure 2.2: The left column shows images from our MARX simulations (assuming a *Chandra* HETGS + ACIS-S configuration). The green circle and horizontal lines show the target region, and dispersion direction, respectively. The yellow scale bar in each image is 5″ across. The right column shows the extracted 1st order MEG spectrum. The black line and gray line are the plus and minus order spectrum, respectively. The rest energies of the He-like Si Kα line used here are 6.648 Å, 6.688 Å, and 6.740 Å, denoted by green vertical lines in panel (d). Panel (a) shows the spectrum of a point source, with the zeroth order point centered on it. The plus and minus order spectra are aligned at the rest energy of the line trio when the source is located at the zeroth order point. (b) exhibits the effect of shifting the zeroth order point by 5″ along the dispersion direction. The plus and minus orders move away from the line center energy. (c) shows an extended source (10″), which broadens the resulting peaks in the spectra. (d) contains a complex source configuration. The target source has an angular size of 6″, and assumed radial velocity of v_r = + 6,000 km s^{-1}. The nearby source has an angular size of the 6″ and an assumed radial velocity of v_r = + 9,000 km s^{-1}. The assumed angular offset of the nearby source is 15″. Despite the proximity of the two sources, the correct Doppler shift was measured, $v_r = 5878 \pm 1144$ km s^{-1}, in part due to the appropriate choice of osort value (0.05 in this case). The red line and blue lines are the best-fit models for the +1 and -1 order spectra, respectively

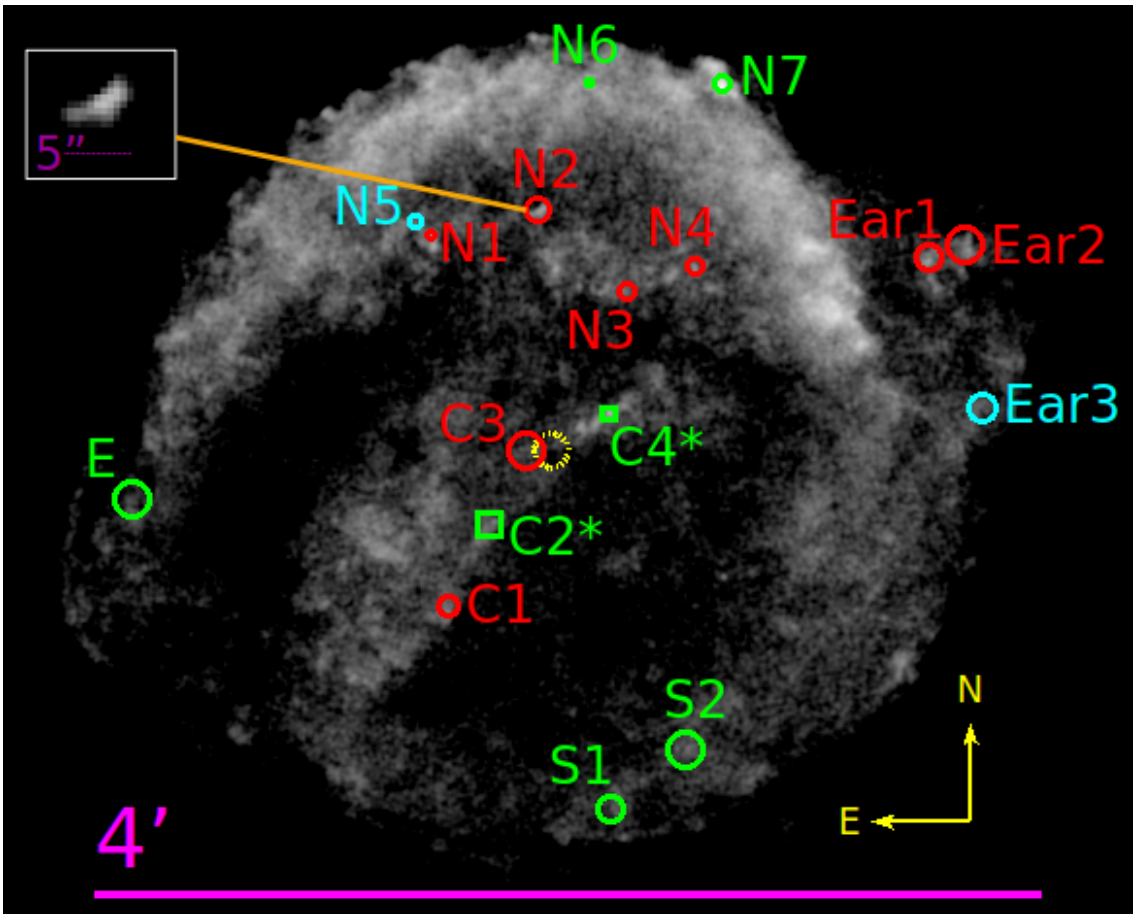

Figure 2.3: ACIS-S gray-scale image of Kepler's SNR from the 2014 observation, filtered to the energy range 1.7 to 2.0 keV. Seventeen ejecta and CSM knots which we analyzed in this work are marked with circles. CSM knots are marked with squares (also, their region names include " * "). Otherwise, we identify all other knots to be metal-rich ejecta based on our spectral analysis of the archival ACIS data. Cyan and red markers indicate blue- and red-shifted features, respectively, while green represents statistically negligible v_r at the 90% confidence interval. The uncertainty in the kinematic center of the SNR estimated by Sato & Hughes (2017b) is denoted by a dotted yellow circle. A zoomed-in image of knot N2 is shown in the upper left corner.

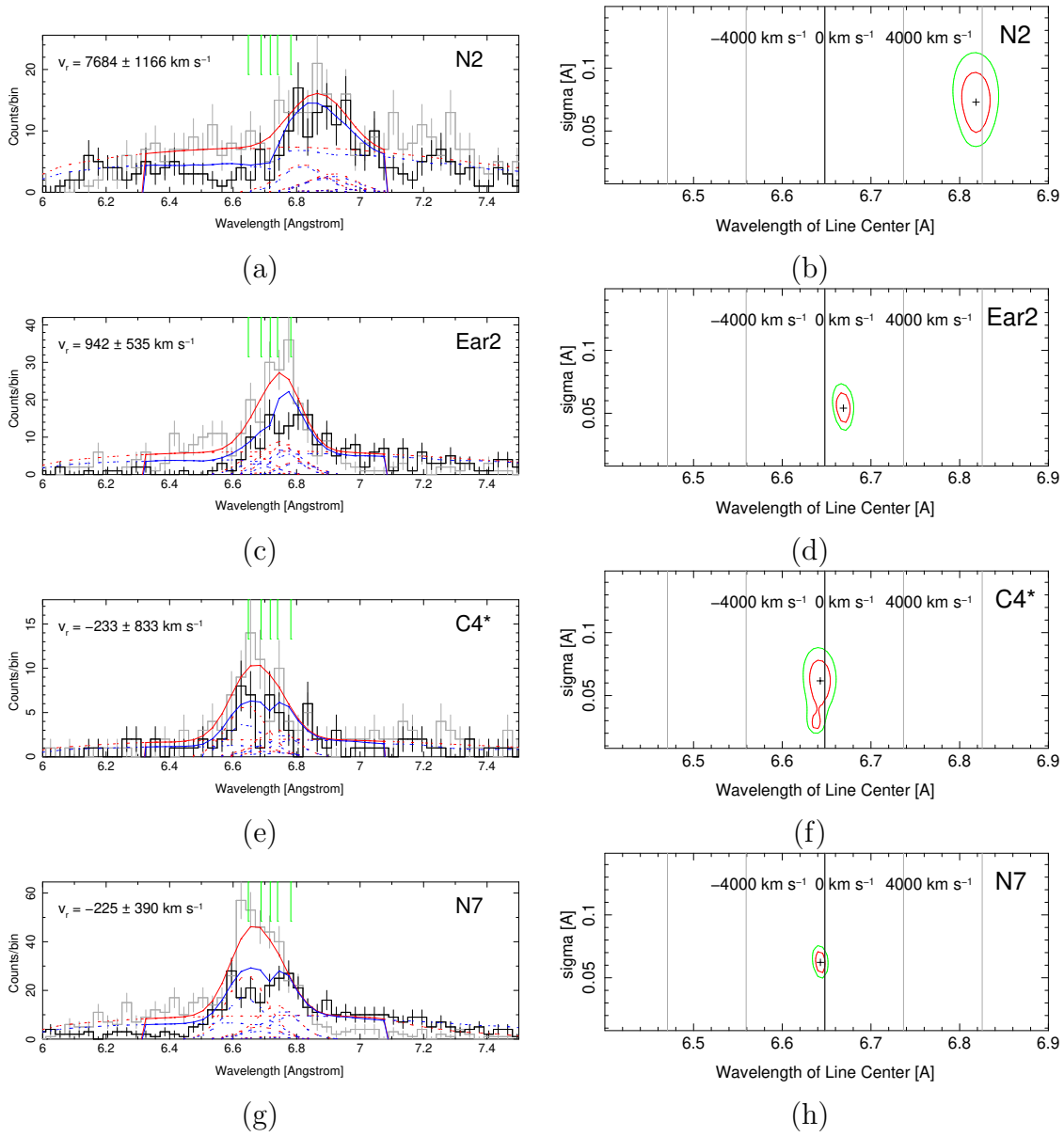

Figure 2.4: Examples of our line center energy fits for small emission features in Kepler. The left column is the HETG spectra overlaid with the best-fit model. The straight green lines show the locations of the rest frame He-like Si Kα line center wavelengths. The dashed lines show individual Gaussian components of our best-fit model. The errors represent a 90% confidence interval. Gray: MEG +1 data, Black: MEG -1 data, Red: MEG +1 model fit, Blue: MEG -1 model fit. The right column shows the confidence level contours for the best fit v_r value. The red and green contours represent a 68% and 90% confidence interval, respectively. Panels (a-b) and (c-d) are from regions N2 and Ear2, respectively, showing clearly redshifted spectra. Panels (e-f) and (g-h) are from regions C4* and N7, respectively, showing negligible Doppler shift

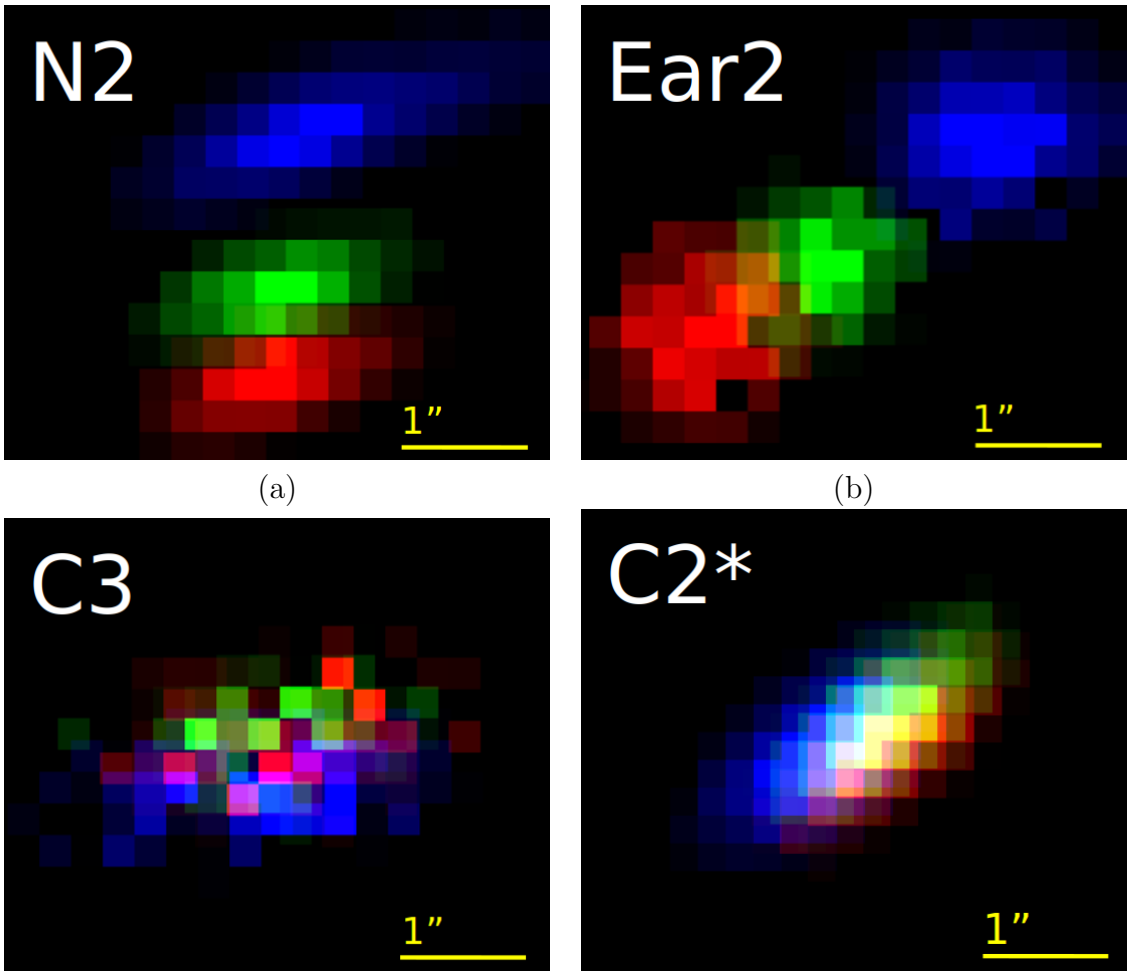

Figure 2.5: ΔC (where ΔC is the difference between the C statistic for this image and the minimum C statistic, as defined in Section 2.3.4) images showing positional differences of regions (a) N2, (b) Ear2, (c) C3, and (d) C2* among observations performed in 2000 (red), 2004 (green), and 2014 (blue).

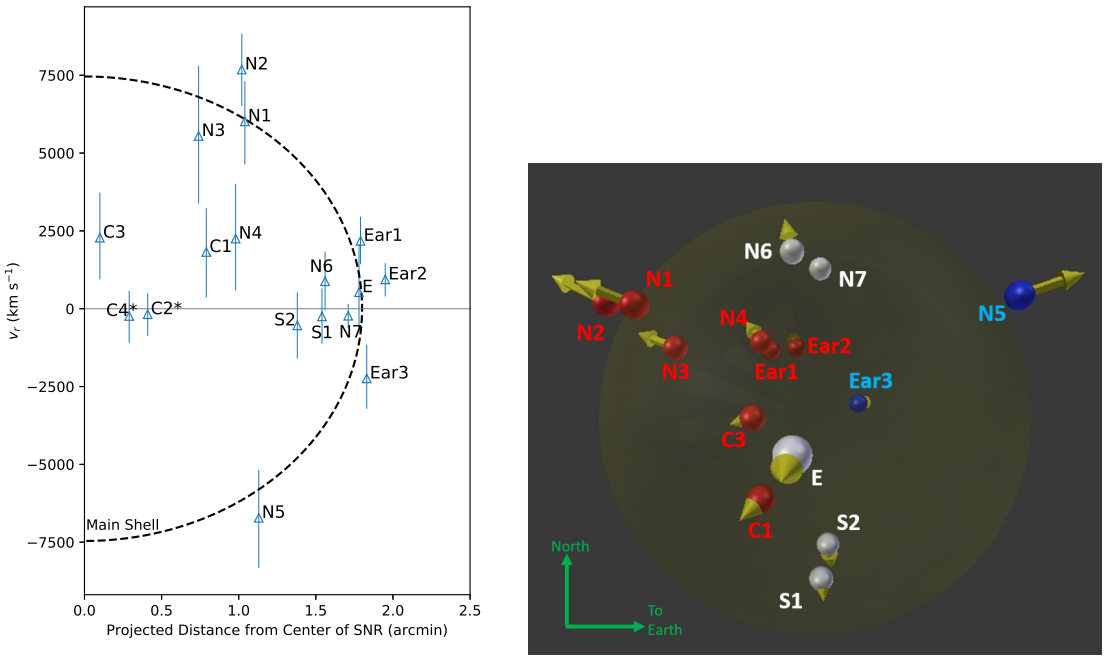

(a) (b)

Figure 2.6: Panel (a) shows the positions of ejecta knots in v_r vs. r (projected angular distance from the center of the SNR) space. The dashed line is the approximate location of the outermost boundary of the main SNR shell. Panel (b) shows a 3-D perspective of the locations of our measured ejecta knots. The red spheres represent redshifted knots, blue spheres are blueshifted knots, and white spheres are those with negligible Doppler shift. The gold arrows indicate the knots' relative magnitude of space velocites and directions. The shaded circle shows the approximate location of the main shell of Kepler's SNR.

2.6 References

Aharonian, F., Akhperjanian, A. G., Barres de Almeida, U., et al. 2008, A&A, 488, 219

Arnaud, K. A. 1996, Astronomical Data Analysis Software and Systems V, 101, 17

Badenes, C., Hughes, J. P., Bravo, E., & Langer, N. 2007, ApJ, 662, 472

Bhalerao, J., Park, S., Dewey, D., et al. 2015, ApJ, 800, 65

Blair, W. P., Long, K. S., & Vancura, O. 1991, ApJ, 366, 484

Blair, W. P., Ghavamian, P., Long, K. S., et al. 2007, ApJ, 662, 998

Borkowski, K. J., Lyerly, W. J., & Reynolds, S. P. 2001, ApJ, 548, 820

Burkey, M. T., Reynolds, S. P., Borkowski, K. J., & Blondin, J. M. 2013, ApJ, 764, 63

Cash, W. 1979, ApJ, 228, 939

Chevalier, R. A. 1982, ApJL, 259, L85

Chiotellis, A., Schure, K. M., & Vink, J. 2012, A&A, 537, A139

Davis, J. E., Bautz, M. W., Dewey, D., et al. 2012, Proc. SPIE, 8443, 84431A

DeLaney, T., Koralesky, B., Rudnick, L., & Dickel, J. R. 2002, ApJ, 580, 914

Dennefeld, M. 1982, A&A, 112, 215

Drake, G. W. 1988, Canadian Journal of Physics, 66, 586

Foight, D. R., Güver, T., Özel, F., & Slane, P. O. 2016, ApJ, 826, 66

Fruscione, A., et al. 2006, Proc. SPIE, 6270

Hachisu, I., Kato, M., & Nomoto, K. 2008, ApJ, 679, 1390

Houck, J. C., & Denicola, L. A. 2000, Astronomical Data Analysis Software and Systems IX, 216, 591

Hoyle, F., & Fowler, W. A. 1960, ApJ, 132, 565

Huenemoerder, D. P., Mitschang, A., Dewey, D., et al. 2011, AJ, 141, 129

Hwang, U., Hughes, J. P., & Petre, R. 1998, ApJ, 497, 833

Iben, I., Jr., & Tutukov, A. V. 1984, ApJS, 54, 335

Kasen, D., Röpke, F. K., & Woosley, S. E. 2009, Nature, 460, 869

Kasuga, T., Sato, T., Mori, K., Yamaguchi, H., & Bamba, A. 2018, PASJ, 70, 88

Katsuda, S., Tsunemi, H., Uchida, H., & Kimura, M. 2008, ApJ, 689, 225

Katsuda, S., Mori, K., Maeda, K., et al. 2015, ApJ, 808, 49

Lazendic, J. S., Dewey, D., Schulz, N. S., & Canizares, C. R. 2006, ApJ, 651, 250

Maeda, K., Benetti, S., Stritzinger, M., et al. 2010, Nature, 466, 82

Maeda, K., Leloudas, G., Taubenberger, S., et al. 2011, MNRAS, 413, 3075

Martínez-Rodríguez, H., Badenes, C., Lee, S.-H., et al. 2018, ApJ, 865, 151

Matsui, Y., Long, K. S., Dickel, J. R., et al. 1984, ApJ, 287, 295

McKee, C. F., & Ostriker, J. P. 1977, ApJ, 218, 148

Park, S., Hughes, J. P., Slane, P. O., et al. 2012, ApJ, 748, 117

Park, S., Badenes, C., Mori, K., et al. 2013, ApJL, 767, L10

Patnaude, D. J., Badenes, C., Park, S., & Laming, J. M. 2012, ApJ, 756, 6

Post, S., Park, S., Badenes, C., et al. 2014, ApJL, 792, L20

Ruiz-Lapuente, P. 2017, ApJ, 842, 112

Sankrit, R., Blair, W. P., Delaney, T., et al. 2005, Advances in Space Research, 35, 1027

Sankrit, R., Raymond, J. C., Blair, W. P., et al. 2016, ApJ, 817, 36.

Sato, T., & Hughes, J. P. 2017a, ApJ, 840, 112

Sato, T., & Hughes, J. P. 2017b, ApJ, 845, 167

Sato, T., Katsuda, S., Morii, M., et al. 2018, ApJ, 853, 46

Shen, K. J., Boubert, D., Gänsicke, B. T., et al. 2018, ApJ, 865, 15

Smith, R. K., Brickhouse, N. S., Liedahl, D. A., et al. 2001, ApJL, 556, L91

Strom, R., Johnston, H. M., Verbunt, F., et al. 1995, Nature, 373, 590

Sun, L., & Chen, Y. 2019, ApJ, 872, 45

Tsebrenko, D., & Soker, N. 2013, MNRAS, 435, 320

Uchida, H., Yamaguchi, H., & Koyama, K. 2013, ApJ, 771, 56.

Vink, J. 2008, ApJ, 689, 231

Wang, C.-Y., & Chevalier, R. A. 2001, ApJ, 549, 1119

Williams, B. J., Borkowski, K. J., Reynolds, S. P., et al. 2012, ApJ, 755, 3

Wilms, J., Allen, A., & McCray, R. 2000, ApJ, 542, 914

Winkler, P. F., Williams, B. J., Reynolds, S. P., et al. 2014, ApJ, 781, 65

Yamaguchi, H., Hughes, J. P., Badenes, C., et al. 2017, ApJ, 834, 124

CHAPTER 3

The 3–D X-ray Ejecta Structure of Tycho's Supernova Remnant

3.1 Introduction

Tycho is the remnant of the Galactic historical supernova SN 1572. Due to its young age, its well-documented SN light curve and its close proximity to Earth ($\sim$ 2 – 4 kpc, see Hayato et al. (2010)), Tycho is an ideal choice for studying the structure of a Type Ia SNR (e.g., Warren et al. (2005)). Both the X-ray spectrum of the SNR (Badenes et al., 2006) and the optical spectrum of the light echo (Krause et al., 2008b) indicate that Tycho is the remnant of a normal Type Ia supernova, neither subluminous nor overluminous. Tycho appears generally circular in shape, with a diameter of $\sim 8'$ in radio and X-ray wavelengths. XMM-Newton observations of Tycho showed an overall uniform distribution of X-ray emitting knots and filaments of shocked ejecta gas (Decourchelle et al., 2001). The X-ray spectrum shows bright emission from the shocked metal-rich ejecta, indicating that Si, S, Ar, Ca, and Fe abundances are several times greater than solar values (Hwang et al., 1998). Suzaku data showed Doppler broadening of X-ray emission lines over large areas of the SNR that suggest a generally spherical expanding ejecta shell (Hayato et al., 2010). Williams et al. (2017) measured the speeds of blueshifted and redshifted ejecta knots with Chandra ACIS data and found no clear evidence for significant asymmetry in the ejecta distribution in Tycho. In many respects, Tycho appears to be the remnant of a standard Type Ia SN explosion. In fact, Type Ia SNe in general show a low degree of continuum polarization, implying that large deviations from spherical symmetry are not common (Wang & Wheeler, 2008).

Although Tycho may be regarded as the remnant of a close approximation of a standard Type Ia SN, it does contain aspherical features whose origin is not fully understood. A prominent example is in the southeast region of the SNR, where a group of metal-rich X-ray emitting ejecta clumps appears to have overtaken the forward shock (Vancura et al., 1995; Decourchelle et al., 2001; Wang & Chevalier, 2001; Fang et al., 2018; Williams et al., 2020; Sato et al., 2020). These ejecta clumps protruding from the southeastern boundary of the SNR include Fe-rich ejecta gas that can be used to pinpoint specific nucleosynthesis models, e.g., an incomplete Si burning or an α-rich freeze-out regime (Yamaguchi et al., 2017). This is in contrast to the western side of the remnant, where there is obvious separation between the ejecta and forward shock (Warren et al., 2005). A Chandra study of the proper motions of reverse-shocked gas showed large azimuthal variations on the order of 50%, while an infrared study with the Spitzer Space Telescope (Spitzer) suggested an ambient density enhancement by a factor of $\sim 3 - 10$ in the northeastern regions compared to the southwest portion of the remnant (Williams et al., 2013). Sato et al. (2019) hydrodynamically simulated Tycho's clumpy structure assuming initially clumped ejecta, as well as perfectly smooth ejecta, in all cases evolving through a uniform ambient medium. Even for the perfectly smooth case, a clumpy structure appears in the ejecta due to Rayleigh-Taylor and Kelvin-Helmholtz instabilities. However, the observed structure in Tycho is more consistent with an initial clumped ejecta structure from the SN rather than instabilities arising from the ejecta interaction with the ambient medium. The optical light echo spectrum of Tycho shows an uncommon high-velocity Ca II absorption feature (Krause et al., 2008a), and thus an asymmetry in the ejecta distribution may have developed early in the evolution of the SNR, or in the SN itself. Sato & Hughes (2017a) performed detailed spectral fits on 27 individual X-ray emitting ejecta clumps across Tycho. They found a disparity in the maximum

velocities of redshifted and blueshifted features, $\lesssim$ 7800 km s $^{-1}$ and $\lesssim$ 5000 km s^{-1}, respectively. The authors also noted large-scale He-like Si Kα line centroid shifts across the SNR, on the order of arcminutes. They suggested that the apparent shifts may be due to differences in the intrinsic intensity of the approaching and receding sides of Tycho.

Here, we investigate the line–of–sight velocity distributions of the clumpy metal-rich ejecta in Tycho based on our deep 450 ks Chandra HETGS observation. The high resolution HETG spectroscopy has significant advantages over the ACIS spectroscopy in several aspects. For example, the gain energies of the ACIS detectors vary by up to 0.3% of the laboratory values[1]. For the He-like Si Kα energy, this corresponds to an estimated uncertainty in the line–of–sight (radial) velocity up to 900 km s^{-1}. The type of CCD array, either ACIS-I or ACIS-S, also adds uncertainties to the line-center energies (Sato & Hughes, 2017a). ACIS data show considerable systematic uncertainties on the emission line-center energy depending on background subtraction regions. These effects contribute to overall systematic uncertainties of up to 2000 km s^{-1} in ACIS radial velocity (v_r) measurements (Sato & Hughes, 2017a). The dispersed gratings spectroscopy of the HETG can avoid such systematic uncertainties associated with the ACIS spectroscopy. Absolute wavelength uncertainties in line-center measurements with the HETG are generally $\lesssim$ 100 km s^{-1} (Marshall et al., 2004; Ishibashi et al., 2006)[2]. Thus, HETG line-center energy measurements are dominated by statistical uncertainties, while the ACIS line-center measurements are dominated by systematic uncertainties. In this work, we combine our radial velocity measurements of clumpy ejecta knots using our deep HETG data with the proper motion measurements of those knots using archival ACIS imaging data–sets to build

[1]https://cxc.harvard.edu/proposer/POG/html/chap6.html#tth_sEc6.8

[2]https://cxc.harvard.edu/proposer/POG/html/chap8.html

a 3–D picture of the overall ejecta structure. In Section 3.2, we present the details of our deep Chandra HETG observation. In Section 3.3, we report our analysis and results, and in Section 3.4 we discuss our interpretations. We conclude our study in Section 3.5.

3.2 Observations

We performed our Chandra HETG observations of Tycho from 2017 October 17 to 2017 November 19. The aimpoint was set at R.A.(J2000) = $00^{\rm h}25^{\rm m}19^{\rm s}.0$, decl.(J2000) = $+64°08'10\farcs0$, which is close to the geometric center of the roughly circular SNR. The date and exposure time of each observation are listed in Table 3.1. The total effective exposure time is 443 ks. We processed the raw event files using CIAO version 4.11 and the CALDB version 4.8.2 to create a new level=2 event file using the CIAO command, `chandra_repro`. We extracted the 1st-order dispersed spectra from a number of small regions across the SNR (Section 3.3.3) using the TGCat scripts `tg_create_mask`[3], `tg_resolve_events`[4], and `tgextract`[5], and created the full set of corresponding detector response files using the script, `make_responses`, which accounts for the zero-order position and dispersed region size and orientation generated from `tg_create_mask`. The HETG-dispersed image of Tycho is shown in Figure 3.1.

We also use archival ACIS-I observations of Tycho (Table 3.2) to supplement the HETG data analysis. For the ObsIDs taken in 2009, we combined all 9 individual ObsIDs, re-projecting them onto ObsID 10095 which had the longest exposure. The main purpose of our archival ACIS data analysis is to measure proper motions of

[3]http://cxc.harvard.edu/ciao/ahelp/tg_create_mask.html

[4]http://cxc.harvard.edu/ciao/ahelp/tg_resolve_events.html

[5]http://cxc.harvard.edu/ciao/ahelp/tg_extract.html

small ejecta knots in Tycho. Thus, we re-align these ACIS images taken at three different epochs using the `reproject_aspect` command in CIAO, accounting for the astrometric correction based on 5 to 16 background point sources (depending on the ObsID) with their sky positions identified in the NASA/IPAC Extragalactic Database (NED)[6].

3.3 Data Analysis and Results

3.3.1 Region Selection

Based on the archival Chandra ACIS observation of Tycho, we identified clumpy emission features that are bright in the Si Kα (1.7 - 2.0 keV) band as candidate targets for HETG spectral extraction. We extracted their individual 1st-order MEG spectra from our Chandra HETG observation. In Figure 3.1, it is clear that the zero-order and 1st-order images overlap. In some regions, this overlap may cause the 1st-order HETG spectrum to be contaminated by the overlapping zero-order emission. To avoid these regions, we compared the counts in the +1 and -1 order spectra. We rejected regions where the discrepancy in counts in the Si Kα band between the +1 and -1 orders was extremely dissimilar (due to extra counts from the zero-order emission). Regions inside the overlap area that had a similar ratio of +1 to -1 counts as those regions outside the overlap area were not considered to be significantly contaminated. Applying similar methods to those developed by Millard et al. (2020), we select 59 small candidate ejecta regions (angular sizes of $\sim 3'' - 10''$) to measure the He-like Si Kα line-center energy ($\sim$ 1.86 keV) for each region. We selected target regions such that similarly bright emission features are at least $\sim 20''$ away along the dispersion

[6]https://ned.ipac.caltech.edu/

direction to avoid spectral contamination. Each region has at least 200 1st-order MEG counts in the Si Kα band.

3.3.2 Ejecta Identification

To identify the overabundant nature of the ejecta-dominated regions (out of our 59 selected candidate regions), we performed spectral model fits for each individual regional spectrum based on the combined 2009 archival Chandra ACIS data (merging all ObsIDs taken in 2009, to achieve the total of $\sim$ 731 ks). We fitted the observed 1.6 – 4.5 keV band ACIS spectrum extracted from each region with an absorbed `vpshock` model using the XSPEC software package version 12.10.1. We estimated the background spectrum using an annulus region encircling the entire remnant. Then, we subtracted the background spectrum from the regional source spectra before fitting them with the spectral model. We fixed the absorption column at $N_H = 8 \times 10^{21}$ cm^{-2} for Tycho (Foight et al., 2016). We allowed the electron temperature, kT, and ionization timescale, τ, to vary. We also varied the redshift, normalization, and abundances of Si, S, Ar, and Ca. Since contributions from other elements are negligible in the 1.6 – 4.5 keV band, we fixed all other elemental abundances at solar values (Wilms et al., 2000). The model gave satisfactory fits to the data, with reduced chi-squared values ranging from $\chi^2/dof = 51/73$ – $119/60$. We confirm that the best–fit abundances are several times solar values, indicating that all knots in our sample are ejecta-dominated. The best-fit electron temperatures of the ejecta knots in our sample are $kT_e \sim 1$ – 5 keV, with ionization timescales $\tau \sim 2$ – 50×10^{10} cm^{-3} s, generally consistent with the typical ejecta values reported in Williams et al. (2017).

3.3.3 Radial Velocities of Ejecta

To measure the radial velocity of each X-ray emission feature in our sample, we adopt the method used in Millard et al. (2020), using the Interactive Spectral Interpretation System (ISIS) software package version 1.6.2. Spatially integrated broadband ACIS spectra of Tycho shows bright Si, S, Ar, Ca, and Fe emission lines. However, we are interested in the HETG spectra of small features that are only a few arcseconds across. The effect of a small region size and the HETG detection efficiency greatly reduces the prominence of these lines. Ultimately, our HETG spectra of these small emission features are dominated by He-like Si-Kα. For each of our regional spectra, we measure the line-center energies in the Si Kα band by fitting six Gaussian curves to the spectrum to account for the three He–like Si Kα lines (6.648 Å for resonance, 6.688 Å for intercombination, 6.740 Å for the forbidden line), and two Li-like Si XII lines at 6.717 Å and 6.782 Å and one for the diffuse background emission of the SNR. We jointly fit the model to the MEG +/- 1 order spectra, tying the line-center wavelengths between spectra dispersed along the positive and negative arms. Since the individual spectral lines may not be clearly resolved due to the extended nature of the ejecta knots, we fix the flux ratios among the triplet He-like Si Kα lines and Li-like Si lines at those corresponding to the best-fit electron temperature and ionization timescale for each region (Section 3.3.2). We compared our measured line-center wavelength with the rest value for the resonance line at 6.648 Å, which is generally the strongest among the five lines in our model. The difference between the rest and observed values gives the Doppler shift, which we use to estimate the v_r for each knot. The location of each knot is marked in Figure 3.2a, and our results are summarized in Table 3.3. Example HETG spectra and best-fit models for the +1 and -1 arms are shown in Figures 3.2b and 3.2c.

In Figure 3.2a, we show regions for which we measure Doppler shifts of Si lines. Our measured v_r ranges from $\sim$ –5200 to +5300 km s^{-1}. We note that our sample partially overlaps with those studied by Sato & Hughes (2017a) and Williams et al. (2017) (SH17a and W17, hereafter), who measured the v_r of small ejecta regions in Tycho based on the lower-resolution ACIS spectroscopy: i.e., 15 and 19 regions of our sample are also included in SH17a and W17, respectively. We find general agreement between our measured values and those from ACIS data, as shown in Figure 3.3. We found a few exceptions where our measured radial velocities are smaller than those in SH17a by a few 10^3 km s^{-1} (e.g., regions C6 and SW3). The origin of the discrepancy is unclear, but may be due in part to confusion from neighboring emission. Contributions from the diffuse expanding hemispheres of the remnant may be present even in small extraction regions of only a few arcseconds in diameter, and could influence the ACIS velocity estimates.

It is remarkable that we measure a highly significant radial velocity of $v_r = -1860 \pm 170$ km s^{-1} for the SE protrusion (region SE3 in Figure 3.2a). This v_r has been suggested based on the ACIS spectroscopy, but was not constrained due to large uncertainties of a few 10^3 km s^{-1} (SH17a; W17). Based on our high resolution HETG spectroscopy, we accurately measure (within $\sim$ 10% uncertainties) this intriguing v_r for an ejecta feature projected beyond the main shell of the SNR with an order of magnitude improved accuracy.

3.3.4 Ejecta Proper Motions

Based on the archival Chandra ACIS-I data from 2003, 2009, and 2015 (Table 3.2), we estimate the proper motions of the ejecta regions in our sample. To measure the proper motions, we apply the methods described in Sato et al. (2018). To find the position of each knot at different epochs, we took the image from the long observation

in 2009 (ObsID 10095) as the reference image and compared it to the images from the 2003 and 2015 epochs filtered to the 1.6 – 4.5 keV band. We incrementally shifted the 2003 and 2015 images in R.A. and decl. until a statistically good match with the reference image was obtained, i.e., the Cash statistic was minimized. To estimate the systematic uncertainties, we applied this image fitting method to five background point sources. We find the systematic uncertainties of our method to be $\sigma_{\mu_{RA}} = 0\farcs06$ yr^{-1} and $\sigma_{\mu_{decl.}} = 0\farcs03$ yr^{-1}, in reasonable agreement with the uncertainties estimated in Katsuda et al. (2010). We were able to successfully measure proper motions for 37 of the 59 knots in our sample. For other knots, it was difficult to measure proper motions because they were faint or contaminated by complex emission features in the immediate surroundings. Regions projected close to the center of the SNR do not show measurable proper motions (as perhaps expected), and thus their space velocity is dominated by their radial velocity.

The results of our proper motion measurements are summarized in Table 3.3. Our measured values range from $-0\farcs32$ yr^{-1} to $+0\farcs29$ yr^{-1} in R.A. and $-0\farcs33$ yr^{-1} to $+0\farcs35$ yr^{-1} in decl. Our proper motion measurements suggest that all of the knots in the sample have undergone some significant deceleration, ranging from $\eta = 0.21$ to 0.80, with an average $\eta = 0.51$. The proper motion directions are shown in Figure 3.4.

We combine the radial velocity and proper motion measurements to estimate the 3–D space velocity of regions in our sample. We adopt a distance of 3.5 kpc to Tycho (Williams et al., 2013). At this distance, the transverse velocities of knots at the boundary and the radial velocities of knots projected near the center of the SNR generally agree, $v_r \sim 5500$ km s^{-1}, which is consistent with the maximum range of space velocities for ejecta regions in our sample. Combining the radial velocity and proper motions we estimate the space velocities of $\sim$ 1900 – 6000 km s^{-1}, with

an average $v_s \sim 4200$ km s^{-1}. These velocity ranges are in plausible agreement with those estimated by SH17a and W17, but with uncertainties smaller by a factor of $\sim$ 3 on average.

3.4 Discussion

3.4.1 Azimuthal Variations in Ejecta Velocity

In Figure 3.5, we plot our estimated space velocity for each knot against its azimuthal angle (position angles measured counter-clockwise from north). For knots projected closer to the center of the remnant, their true location along the periphery of the SNR is more uncertain. Thus, we only included knots with projected positions offset from the center where we have firmly estimated their proper motions. The ejecta knots in the southeast (SE) quadrant of Tycho have $v_s \sim 6000$ km s^{-1}, and thus appear to be among the fastest-moving knots ($\sim$ 40% faster than the average space velocity of our sample). This high space velocity is in plausible agreement with the presence of ejecta bullet-like features (protrusions extending beyond the main SNR shell, (Wang & Chevalier, 2001)) where high-speed overdense clumps overtake the forward shock. However, the protruding knots are not individual ejecta features like in Wang & Chevalier (2001), but are part of a large-scale portion of the ejecta that was propelled from the explosion more energetically than elsewhere in the remnant. The densities along the SE rim are larger by a factor of a few than those in the southwest (SW) (Williams et al., 2013). However, the ejecta space velocities in the SE are faster by a factor of $\sim$ 2 than those in the SW. Thus, the ejecta velocities in SE regions may not be directly related to a rarefied ISM in that direction, but probably due to their intrinsically energetic nature. It is interesting to note that there is a prominent high-speed ejecta knot (NW5) approaching $v_{space} \sim 6000$ km

s^{-1} projected at the northwest (NW) boundary, in a nearly opposite direction from the protruding SE knots. While it is tempting to speculate strong ejecta outflows along the SE-NW axis connecting these particularly fast-moving knots, we find no additional substantial evidence to support such a bi-polar ejecta outflow along this axis.

In the northeast (NE), from position angles 10° to 100°, the ejecta space velocities appear to decrease, from $\sim$ 6000 km s^{-1} to $\sim$ 2000 km s^{-1}. The space velocity then sharply rises back up to $\sim$ 6000 km s^{-1} for ejecta knots in the SE from position angles $\sim$ 100° – 170°, before decreasing again to 2000–4000 km s^{-1} in the SW from 200° to 250°. Some decreases in ejecta velocity with azimuthal angle are coincident with increasing ambient density, suggesting an origin from the SNR's interaction with a dense surrounding medium. A Spitzer study of the ratio of the 70 to 24 μm fluxes in Tycho revealed an increase of post-shock densities at the rim from azimuthal angles of roughly 10 – 80° and 300 – 330° (Williams et al., 2013), similar to the angle ranges of decreasing velocity (see Figure 3.5). The ejecta in these regions may have been slowed either by direct interaction with the higher-density ISM gas or by an enhanced reverse shock that developed due to the shock-ISM interaction, or a combination of both.

3.4.2 3–D Ejecta Structure

The X-ray emitting knots and filaments of the shocked ejecta gas in Tycho are distributed, in general, uniformly across the face of the SNR (see Figure 3.2). Our kinematic study of these ejecta knots shows that the overall spatial and velocity distributions of ejecta in Tycho are relatively smooth, in contrast to the case of Kepler's SNR where significant deviations from a spherical distribution, such as the "Ears" and nearly freely-expanding ejecta knots are present (Sato & Hughes, 2017b;

Millard et al., 2020). On the other hand, we find some asymmetric ejecta structures in Tycho, based on our ejecta velocity measurements. Our 3–D reconstruction of the ejecta distribution (Figure 3.6) based on our radial velocity and proper motion measurements for a number of clumpy ejecta features indicates that the southern shell is dominated by redshifted ejecta (23 redshifted vs 6 blueshifted), while the majority of clumpy ejecta features in the northern shell are blueshifted (13 blueshifted vs 8 redshifted). The Chandra ACIS study by SH17a similarly revealed more blueshifted Si He-like and S He-like line-center energies in the north than in the south. The authors suggested that the observed discrepancy may be caused by a density enhancement of $\lesssim \sqrt{3}$ on the near side of the SNR compared with the far side. In this scenario, the density enhancement causes a stronger reverse shock on the northern near side. Thus, more reverse-shocked ejecta is observed in the north than in the south. A similar scenario could account for the north-south (N-S) differential in ejecta knots on the far side of the SNR. This N-S asymmetry of ejecta due to ambient density variation may be supported by the interacting density variations as reported by Williams et al. (2013) and Katsuda et al. (2010).

Although a variation in the ambient gas density surrounding Tycho is a plausible origin for the N–S ejecta differential, we may also consider that it could be due to an asymmetry in the early ejecta distribution immediately after the explosion. Seitenzahl et al. (2013) simulated a range of Type Ia explosion scenarios and found that DDT models with fewer ignition points resulted in more asymmetric explosions. Ferrand et al. (2019) propagated a fully 3–D N100 DDT model of Seitenzahl et al. (2013) into the SNR stage. They found that asymmetries in the explosion were required to explain the large-scale structures in X-ray maps of Tycho (specifically, the power spectrum of radius fluctuations around the rim, Warren et al. (2005)). Ferrand et al. (2021) further explored the early–stage evolutions of SNRs using the

N5 (small number of ignition points) and N100 (large number of ignition points) DDT and pure deflagration models of Seitenzahl et al. (2013) and Fink et al. (2014). The authors found that the N5ddt models produce a more asymmetric, dipolar remnant whose imprint lasts up to a few hundred years. It is not straightforward to directly compare the results of these simulations with the non-uniform ejecta distribution inferred from our velocity measurements. However, our work suggests the presence of an aspherical ejecta velocity distribution in Tycho.

3.4.3 Explosion Center and Reverse Shock

We estimate the kinematic center of Tycho from our proper motion measurements of ejecta knots. We choose knots which have both $\mu_{R.A.}$ and $\mu_{decl.}$ greater than the systematic uncertainty. We generally follow the technique employed in Sato & Hughes (2017b). Initially, we assume that each knot has moved at its current proper motion speed since the explosion (i.e., $\eta = 1$) to estimate its 2-D starting position. We average the starting positions of all individual knots to calculate the tentative "initial" kinematic center. Then, we calculate the new expansion index for each knot based on this tentative kinematic center, and trace its motion back to a new starting point, this time dividing the distance traveled by the expansion index to account for its decelerated motion. We repeat this process until the average kinematic center converged on a single value (after about 25 iterations). Our estimated kinematic center is R.A.(J2000) = $00^{\rm h}25^{\rm m}18^{\rm s}.725 \pm 1^{\rm s}.157$ and decl.(J2000) = $+64^\circ08'02''.5 \pm 11''.2$. This position is $\sim 13''$ southwest of the geometric center estimated by Warren et al. (2005). The previously suggested candidates for the companion of Tycho's progenitor, Tycho G (Ruiz-Lapuente et al., 2004), Tycho E (Ihara et al., 2007), and Tycho B (Kerzendorf et al., 2013, 2018), are located approximately $33''$ E, $14''$ NE, and $17''$ NW from our estimated center, respectively. Assuming a distance of 3.5 kpc, their

transverse velocities since the explosion would be $\sim$ 1200 km s^{-1}, 500 km s^{-1}, and 600 km s^{-1}, respectively. This is in contrast to their recently measured proper motions (Kerzendorf et al., 2013), which would imply transverse velocities of 100 – 200 km s^{-1}. However, since the positions of Tycho E and Tycho B are within a few arcseconds of the error ellipse of our estimated center (see Figure 3.4), they may have travelled a shorter distance if our kinematic center is representative of the explosion site. Thus, their transverse velocities since the explosion could be significantly slower, in line with the current values. Tycho G is located several arcseconds outside of the error ellipse, and therefore its current proper motion is still too low to account for the angular distance it would have travelled from our kinematic center since the explosion.

We plot our measured radial velocity for each knot against its angular distance from the center of the SNR in Figure 3.7a. Figures 3.7b and 3.7c show the north–south asymmetry discussed in Section 3.4.2. We plot the main shell (the forward shock) and the reverse shock position from Yamaguchi et al. (2014) estimated from the location of Fe Kβ emission generally in the NW quadrant of Tycho. The bulk of the ejecta knots in our sample are positioned between the forward and reverse shocks, as expected. However, there are several knots positioned closer to the SNR center beyond the reverse shock. The locus of these inner ejecta knots appears to form a smaller reverse shock at $\sim 2.0'$ from the SNR center, or 75% of the $2.6'$ radius for the reverse shock estimated by Yamaguchi et al. (2014). According to models of dynamical evolution of SNRs (Truelove & McKee, 1999) with an explosion energy of 1.2×10^{51} ergs (Badenes et al., 2006) and an ejected mass of 1.4 M$_{\odot}$, ambient density variation by a factor of $\sim$ 4 (similar to that reported by Williams et al. (2013) for Tycho) may produce $\sim$ 30% deeper-reaching reverse shock. These knots beyond the reach of the previously-known reverse shock are blueshifted, and therefore are positioned on the near side of the SNR. Thus, these inner ejecta knots may represent deviated parts of the reverse

shock due to the shock interaction with denser medium on the near side of the SNR. Recently, X-ray proper motion measurements of Tycho's forward shock showed that its expansion has significantly decelerated from 2003 to 2015 (down to 40% of its initial value, Tanaka et al. (2021)). The authors suggested that the forward shock may be encountering a non-uniform wall of dense gas, possibly created from the winds of the progenitor system. Our results may support the presence of a similar density variation along the line of sight.

3.5 Conclusions

We have measured the radial velocities of 59 small ejecta features in Tycho's SNR using our deep 450 ks Chandra HETG observation. Based on these measurements, our 3–D reconstruction of Tycho shows a large-scale asymmetry where most knots in the northern half are blueshifted and thus on the near side, and most knots in the southern half are redshifted and therefore are located on the far side. Ambient density variations across the near and far sides of the remnant might have caused non-uniformity in the formation of reverse shock, and thus resulted in the differences in the frequency of detected ejecta knots. Alternatively, the identified asymmetry could be caused by a non-spherical explosion of the progenitor.

For 37 of the 59 ejecta features in our sample, we measured their proper motions using archival Chandra ACIS data. We estimate an expansion center based on our measured proper motions. Combining the radial velocities and proper motions, we find space velocities up to 6000 km s^{-1}. The azimuthal distribution of our measured space velocities shows generally higher speeds of ejecta towards the SE. Regions with low velocity coincide with higher ambient density at the rim. However, the high-velocity SE regions do not coincide with comparatively lower ambient densities, and therefore probably resulted from higher kinetic energy being deposited in that direc-

tion from the explosion. Based on our detection of relatively lower radial velocities for several ejecta knots projected near the center of the SNR, we postulate a considerable ambient density variation along the line of sight (e.g., a higher density on the near side of Tycho).

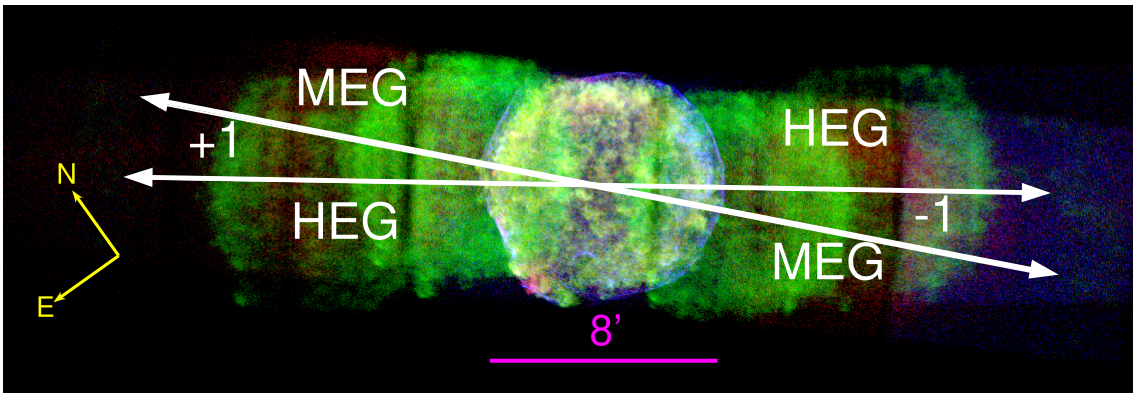

Figure 3.1: Chandra HETG 3-color dispersed image of Tycho. Red: 0.7-1.2 keV, Green: 1.7-2.0 keV and Blue: 4.0-8.0 keV. Our color codes are selected to represent the Fe L line complex (red), He-like Si Kα lines (green), and the continuum-dominated band (blue), respectively. The white arrows show the dispersion directions of the Medium and High Energy Gratings.

Table 3.1. Chandra HETG Observations of Tycho's SNR

Observation ID	Start Date	Exposure Time (ks)
19293	2017-10-17	49.7
20813	2017-10-21	47.8
20822	2017-10-23	13.9
19292	2017-10-26	19.8
20820	2017-10-27	30.5
20819	2017-10-29	44.5
19291	2017-10-30	40.0
20832	2017-11-01	50.1
20833	2017-11-03	34.6
20834	2017-11-04	35.9
20835	2017-11-06	27.6
20799	2017-11-17	22.2
20821	2017-11-19	25.6

Table 3.2. Archival Chandra ACIS-I Observations of Tycho's SNR

Observation ID	Start Date	Exposure Time (ks)
3837	2003-04-29	144.6
10093	2009-04-13	117.6
10094	2009-04-18	89.9
10095	2009-04-23	173.4
10096	2009-04-27	104.9
10097	2009-04-11	106.9
10902	2009-04-15	39.3
10903	2009-04-17	23.9
10904	2009-04-13	34.7
10906	2009-05-03	40.9
15998	2015-04-22	146.7

Table 3.3. Radial Velocity and Proper Motion Measurements of Ejecta Features in Tycho's SNR

Region	R.A.[a] (degree)	Decl.[a] (degree)	D[b] (arcmin)	v_r (km s^{-1})	μ_{RA}[c] (arcsec yr^{-1})	μ_{Dec}[c] (arcsec yr^{-1})	μ_{Tot}[d] (arcsec yr^{-1})	η[e]	v_s[f] (km s^{-1})
SE1	6.48336	64.130282	4.07	-2470^{+410}_{-420}	-0.323 ± 0.064	-0.002*	0.323 ± 0.064	0.6 ± 0.12	5910 ± 980
SE2	6.47022	64.128169	3.74	-670 ± 560	-0.09 ± 0.064	-0.057 ± 0.04	0.106 ± 0.066	0.21 ± 0.13	1890 ± 1040
SE3	6.49035	64.125542	4.28	-1860 ± 170	-0.299 ± 0.063	-0.096 ± 0.04	0.314 ± 0.064	0.56 ± 0.11	5530 ± 1000
SE4	6.46192	64.12032	3.6	1650^{+690}_{-710}	-	-	-	-	-
SE5	6.40962	64.125008	2.2	3840 ± 820	-	-	-	-	-
SE6	6.47617	64.106979	4.21	1660 ± 660	-0.249 ± 0.062	-0.061 ± 0.038	0.257 ± 0.063	0.45 ± 0.11	4580 ± 1000
SE7	6.46718	64.10879	3.95	1380^{+610}_{-620}	-0.314 ± 0.063	0.06 ± 0.035	0.32 ± 0.063	0.6 ± 0.12	5490 ± 1020
SE8	6.41552	64.118707	2.47	2780^{+690}_{-710}	-0.238 ± 0.061	-0.086 ± 0.033	0.253 ± 0.061	0.76 ± 0.18	5040 ± 930
SE9	6.3844	64.120199	1.69	4210^{+980}_{-1030}	-	-	-	-	-
SE10	6.42579	64.099514	3.29	2780 ± 680	-	-	-	-	-
SE11	6.4111	64.088671	3.49	1070^{+730}_{-740}	-	-	-	-	-
SE12	6.36942	64.113216	1.65	-920 ± 490	-	-	-	-	-
SE13	6.39798	64.086552	3.39	2100 ± 430	-	-	-	-	-
SE14	6.36005	64.090842	2.72	5180^{+770}_{-740}	-0.012*	-0.171 ± 0.04	0.172 ± 0.07	0.44 ± 0.19	5920^{+880}_{-860}
SE15	6.34372	64.085777	2.93	-20*	-0.053*	-0.326 ± 0.037	0.33 ± 0.067	0.8 ± 0.17	5480 ± 1110
NE1	6.36031	64.198296	3.95	960 ± 600	0.001*	0.354 ± 0.038	0.354 ± 0.068	0.71 ± 0.13	5950 ± 1120
NE2	6.34541	64.162038	1.74	2460^{+1010}_{-1070}	-0.001*	0.158 ± 0.041	0.158 ± 0.071	0.77 ± 0.3	3600^{+1100}_{-1130}
NE3	6.37907	64.182406	3.19	-2290^{+590}_{-600}	-0.029*	0.243 ± 0.038	0.245 ± 0.068	0.61 ± 0.16	4670^{+1020}_{-1030}
NE4	6.35505	64.156519	1.52	-3590^{+490}_{-500}	-0.062*	0.077 ± 0.038	0.099 ± 0.067	0.54 ± 0.33	3950^{+640}_{-650}
NE5	6.38373	64.178972	3.06	-4210^{+600}_{-620}	-	-	-	-	-
NE6	6.40231	64.193381	4.06	910^{+460}_{-470}	-0.125 ± 0.063	0.195 ± 0.038	0.231 ± 0.067	0.45 ± 0.12	3940 ± 1090
NE7	6.40808	64.189185	3.92	-400*	-0.16 ± 0.063	0.207 ± 0.04	0.262 ± 0.068	0.53 ± 0.13	4360 ± 1130
NE8	6.40062	64.165145	2.66	-1800 ± 440	-0.126 ± 0.061	0.158 ± 0.034	0.202 ± 0.063	0.61 ± 0.18	3800^{+950}_{-940}
NE9	6.45171	64.179368	4.23	490*	-0.133 ± 0.062	0.159 ± 0.035	0.207 ± 0.064	0.38 ± 0.11	3460 ± 1050
NE10	6.43524	64.161668	3.26	-1660^{+490}_{-480}	-0.204 ± 0.062	0.049 ± 0.035	0.21 ± 0.062	0.51 ± 0.14	3860 ± 950
NE11	6.46282	64.153989	3.72	100*	-0.173 ± 0.062	0.021*	0.174 ± 0.062	0.36 ± 0.12	2900 ± 1030
NW1	6.20057	64.139647	3.35	1900 ± 570	0.231 ± 0.064	-0.077 ± 0.038	0.244 ± 0.064	0.53 ± 0.14	4470 ± 990
NW2	6.1934	64.153122	3.7	-800 ± 670	0.264 ± 0.064	0.103 ± 0.039	0.284 ± 0.065	0.57 ± 0.13	4780 ± 1070
NW3	6.22578	64.149849	2.84	-310*	0.17 ± 0.064	0.071 ± 0.036	0.185 ± 0.064	0.48 ± 0.17	3080 ± 1060

Table 3.3 (cont'd)

Region	R.A.[a] (degree)	Decl.[a] (degree)	D[b] (arcmin)	v_r (km s^{-1})	μ_{RA}[c] (arcsec yr^{-1})	μ_{Dec}[c] (arcsec yr^{-1})	μ_{Tot}[d] (arcsec yr^{-1})	η[e]	v_s[f] (km s^{-1})
NW4	6.21326	64.154398	3.24	1180 ± 580	0.227 ± 0.064	0.083 ± 0.038	0.242 ± 0.065	0.56 ± 0.15	4190 ± 1050
NW5	6.17947	64.160641	4.2	220*	0.289 ± 0.065	0.155 ± 0.037	0.328 ± 0.066	0.6 ± 0.12	5450 ± 1100
NW6	6.25986	64.154143	2.15	-3980^{+650}_{-660}	0.162 ± 0.063	0.039 ± 0.037	0.167 ± 0.064	0.6 ± 0.22	4850^{+810}_{-820}
NW7	6.25252	64.162735	2.62	-1000 ± 600	0.126 ± 0.064	0.14 ± 0.04	0.189 ± 0.068	0.55 ± 0.19	3290 ± 1090
NW8	6.26811	64.162003	2.3	-3430 ± 500	0.116 ± 0.063	0.081 ± 0.037	0.141 ± 0.065	0.47 ± 0.21	4150^{+740}_{-730}
NW9	6.29317	64.153676	1.49	5320^{+920}_{-950}	-	-	-	-	-
NW10	6.2808	64.16993	2.48	-2620^{+560}_{-540}	0.029*	0.102 ± 0.034	0.106 ± 0.064	0.34 ± 0.19	3160^{+750}_{-740}
NW11	6.30679	64.162212	1.78	-1120 ± 640	-	-	-	-	-
NW12	6.30327	64.166397	2.05	-5220 ± 890	-	-	-	-	-
NW13	6.29901	64.192441	3.58	-80*	-0.030*	0.147 ± 0.04	0.15 ± 0.07	0.33 ± 0.14	2490 ± 1160
NW14	6.31804	64.168952	2.11	5280^{+980}_{-2070}	0.031*	0.149 ± 0.036	0.152 ± 0.065	0.58 ± 0.23	5860^{+1000}_{-1920}
SW1	6.28838	64.07014	3.97	160*	-	-	-	-	-
SW2	6.29334	64.094728	2.53	1140 ± 520	0.076 ± 0.063	-0.194 ± 0.039	0.208 ± 0.068	0.57 ± 0.2	3640 ± 1080
SW3	6.30962	64.113309	1.33	3860^{+870}_{-900}	-	-	-	-	-
SW4	6.2801	64.091581	2.84	2060^{+580}_{-560}	0.061*	-0.214 ± 0.036	0.223 ± 0.065	0.55 ± 0.17	4240 ± 980
SW5	6.27296	64.096338	2.68	840^{+470}_{-480}	0.111 ± 0.063	-0.106 ± 0.035	0.153 ± 0.064	0.4 ± 0.18	2680 ± 1020
SW6	6.24856	64.084384	3.64	860^{+680}_{-630}	0.021*	-0.208 ± 0.035	0.209 ± 0.065	0.41 ± 0.13	3570 ± 1060
SW7	6.28942	64.111983	1.67	3010^{+590}_{-580}	-	-	-	-	-
SW8	6.25281	64.108776	2.49	2370^{+730}_{-720}	0.018*	-0.073 ± 0.038	0.076 ± 0.067	0.21 ± 0.2	2680^{+830}_{-820}
SW9	6.22021	64.099009	3.52	2540 ± 700	0.153 ± 0.063	-0.068 ± 0.037	0.168 ± 0.064	0.34 ± 0.13	3760 ± 920
SW10	6.22228	64.105266	3.26	-1630 ± 340	0.21 ± 0.063	-0.154 ± 0.038	0.26 ± 0.065	0.57 ± 0.15	4620 ± 1020
SW11	6.27209	64.12145	1.65	2830^{+700}_{-680}	-	-	-	-	-
SW12	6.22676	64.120373	2.78	740^{+640}_{-630}	0.118 ± 0.063	-0.081 ± 0.036	0.143 ± 0.064	0.37 ± 0.17	2490 ± 1030
C1	6.3738	64.143253	1.32	-1700 ± 590	-	-	-	-	-
C2	6.36353	64.132469	0.93	-2860^{+580}_{-570}	-	-	-	-	-
C3	6.34361	64.139439	0.52	4460^{+780}_{-770}	-	-	-	-	-
C4	6.34296	64.130289	0.45	4060 ± 880	-	-	-	-	-
C5	6.33638	64.13981	0.41	3680^{+870}_{-950}	-	-	-	-	-
C6	6.31697	64.132757	0.3	3700^{+850}_{-730}	-	-	-	-	-

Table 3.3 (cont'd)

Region	R.A.[a] (degree)	Decl.[a] (degree)	D[b] (arcmin)	v_r (km s^{-1})	μ_{RA}[c] (arcsec yr^{-1})	μ_{Dec}[c] (arcsec yr^{-1})	μ_{Tot}[d] (arcsec yr^{-1})	η[e]	v_s[f] (km s^{-1})
C7	6.31072	64.14762	0.93	4390^{+1040}_{-1210}	-	-	-	-	-

[Note] Errors represent a 90% confidence interval unless otherwise noted.

[a] Position in 2015 (J2000).

[b] Projected angular distance from our estimated kinematic center (see Section 3.4.3)

[c] Includes systematic uncertainties (see Section 3.3.4).

[d] $\mu_{Tot} = \sqrt{\mu^2_{R.A.} + \mu^2_{decl.}}$.

[e] Expansion index (see Section 3.3.4).

[f] Estimated space velocity for a distance of 3.5 kpc.

[*] The error interval includes 0, and thus the direction of motion is uncertain. We show only our best-fit value.

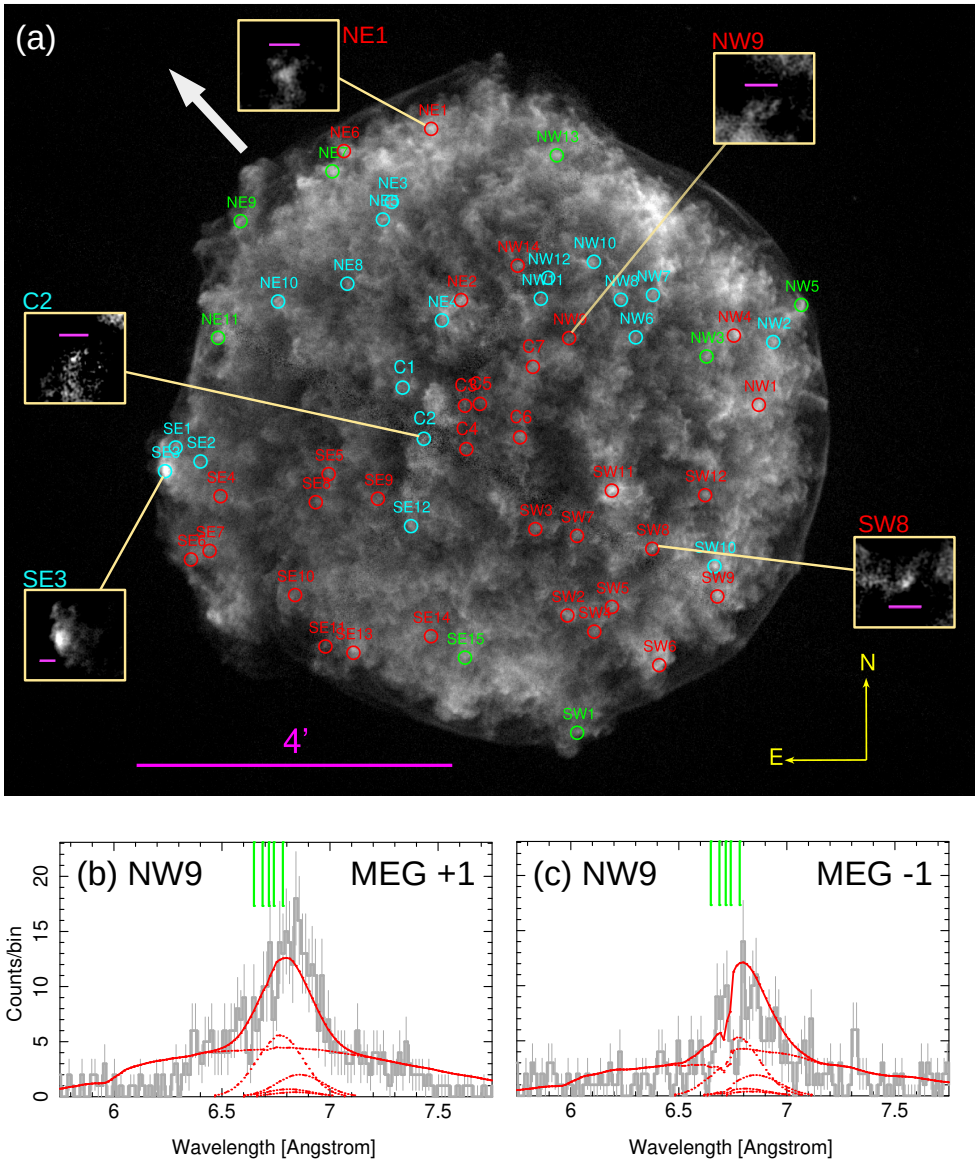

Figure 3.2: (a): An exposure-corrected Chandra ACIS image of Tycho's SNR in the Si Kα band (1.7 - 2.0 keV) based on the archival Chandra data taken in 2009. The fifty-nine ejecta knots analyzed in this work are marked with circles. The white arrow in the upper left indicates the dispersion direction. Cyan and red circles indicate blue- and red-shifted features, respectively, while green represents statistically negligible v_r at the 90% confidence interval. The image cutouts along the periphery show zoom-in views of example ejecta features. The scale bar in each cutout is 10″ across. (b): An example of our line-center energy fit for region NW9. The MEG +1 spectrum is overlaid with our best-fit Gaussian model (Gray: data; Red: model fit). The dashed lines show individual Gaussian components of our best-fit model. The vertical green lines show the locations of the rest frame He-like Si Kα and Li-like Si XII line-center wavelengths. (c): The same as (b), however the data and model are from the MEG -1 spectrum.

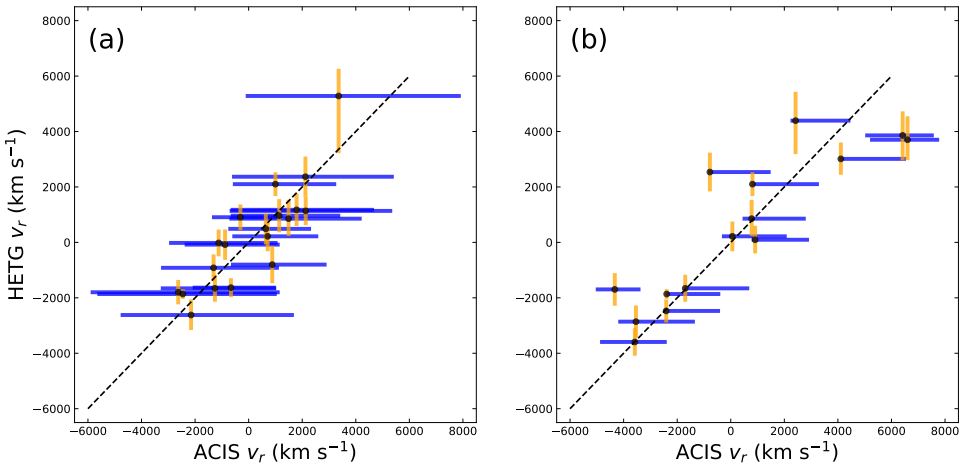

Figure 3.3: Comparison of Chandra HETG vs. ACIS measurements of radial velocity for the common samples of ejecta knots in Tycho between this work and (a) W17 and (b) SH17a. The error bars (blue) in the ACIS measurements include systematic uncertainties.

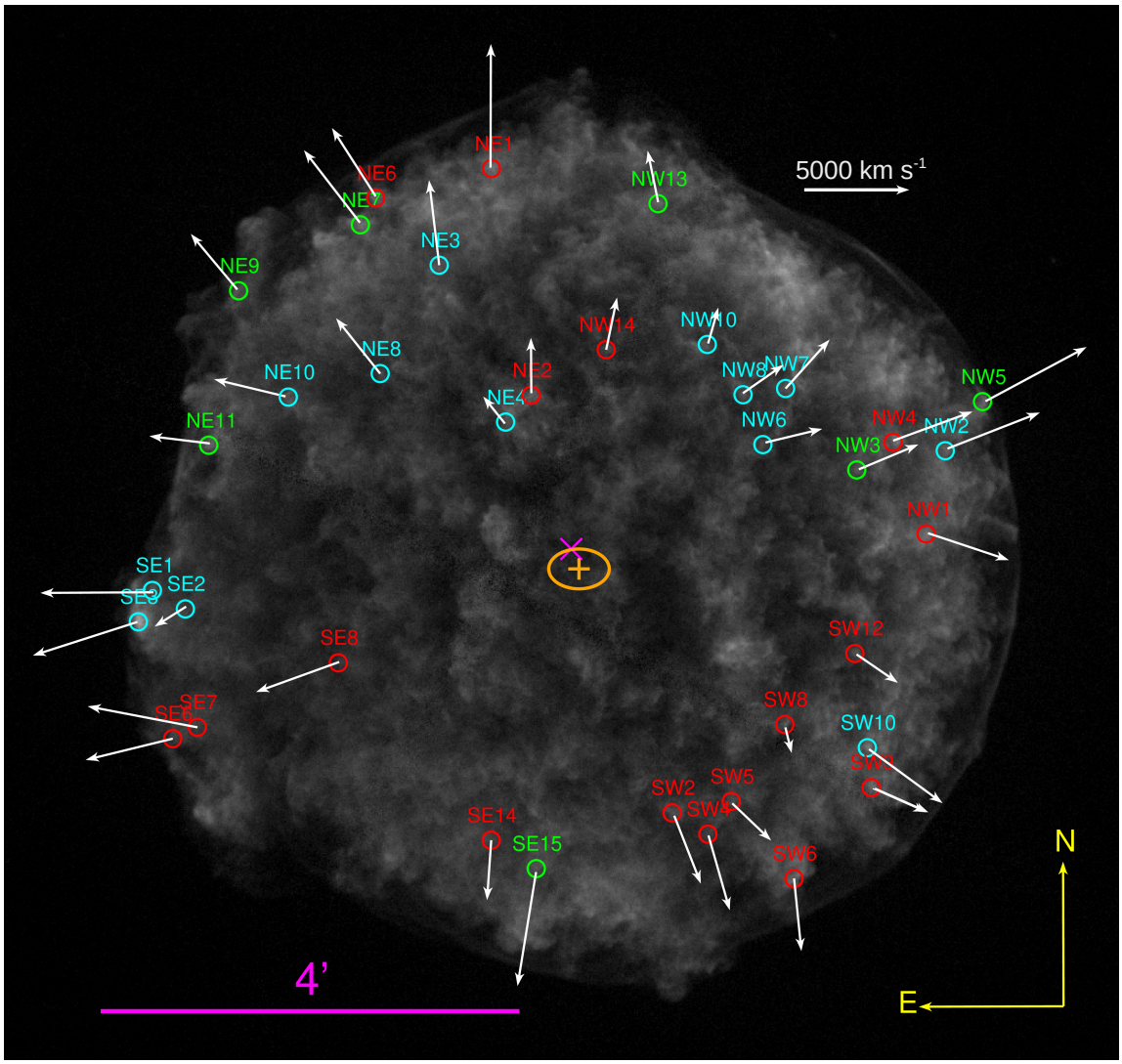

Figure 3.4: The subset of our regions where we measure the proper motion. Each white arrow shows the direction and relative magnitude of the proper motion for each knot. The length of the white arrow at the top right indicates a speed of 5000 km s^{-1}. The orange cross and ellipse indicate the position and uncertainty of our estimated kinematic center based on our proper motion measurements of ejecta knots (see Section 3.4.3). The magenta "X" indicates the geometric center (Warren et al., 2005). The image is the same as in Figure 3.2, scaled to make the arrows more visible.

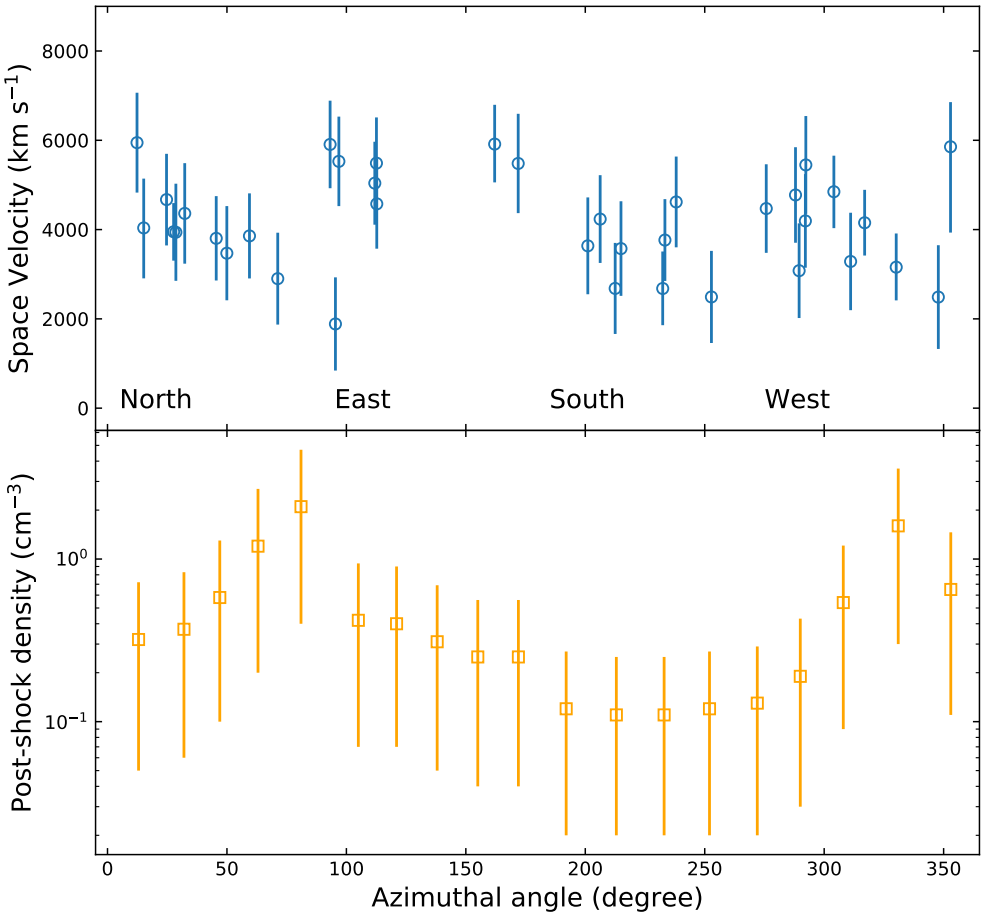

Figure 3.5: The upper panel shows the azimuthal distribution of our estimated ejecta space velocities in Tycho. The bottom panel shows the estimated post-shock densities along the rim from Williams et al. (2013).

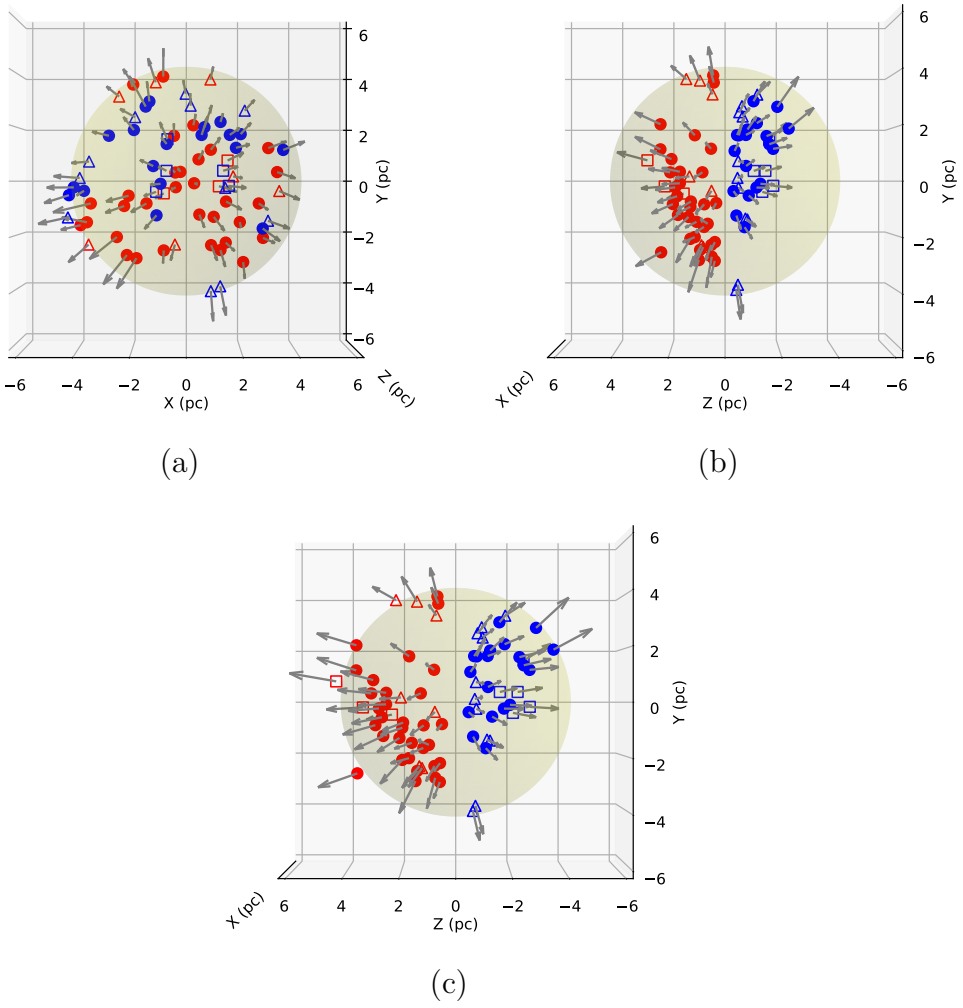

Figure 3.6: 3–D perspectives of the ejecta knots in Tycho. The red markers represent redshifted ejecta and blue are blueshifted ejecta. In (a) – (c), we also overlay the ACIS measurements of ejecta velocities by SH17a and W17. The circles, squares, and triangles show velocity measurements from our HETG sample, SH17a, and W17, respectively. For shared regions, we plot only our v_r values. For the ACIS data, we include only those high-velocity regions with $v_r > 900$ km s^{-1} (the ACIS systematic gain shift uncertainty). For knots where the proper motion was measured, the arrows point in the direction of the estimated 3–D velocity. For the rest of the sample, the arrows point from the SNR center to the position of the knot. The length of the arrow represents the magnitude of the space velocity for each knot. The pale shaded circle shows the approximate location of the main X-ray shell of Tycho. In (a), the X and Y components represent the current locations based on each knot's R.A. and decl. In (b), the Z component of each knot is the measured v_r multiplied by the age of the remnant. The Z component in (b) is likely underestimated due to the deceleration of the knots. In (c), the Z component from (b) is divided by the maximum forward shock expansion index, $\eta = 0.65$ (Katsuda et al., 2010) to show a general approximation of the current physical positions of knots along the line of sight, accounting for their deceleration.

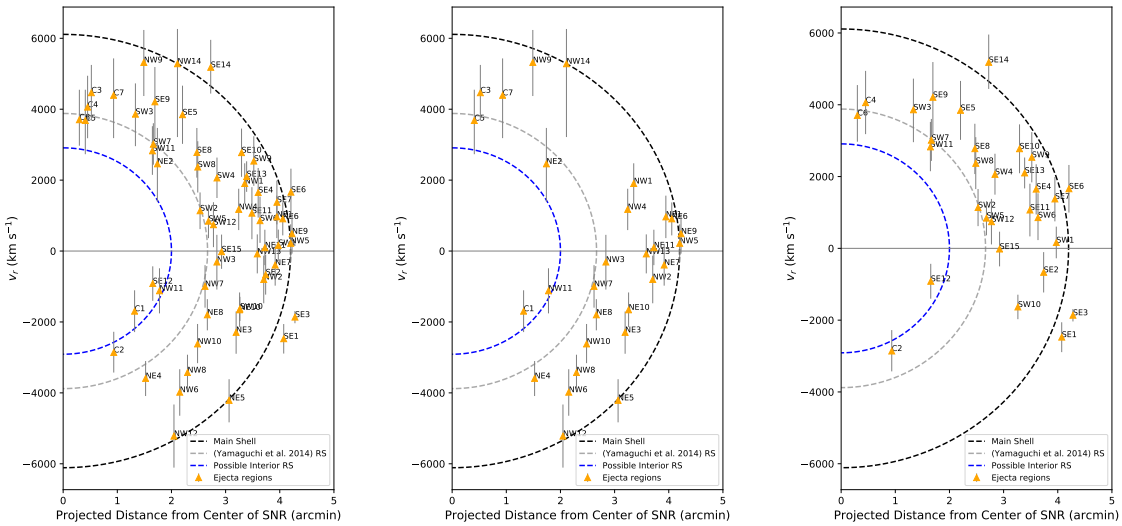

(a) (b) (c)

Figure 3.7: In panel (a), the positions of ejecta knots in v_r vs. r (projected angular distance from the center of the SNR) space. The black and gray dashed loci are the approximate locations of the outermost boundary of the main SNR shell and the reverse shock, respectively. The blue locus is a new potential reverse-shock location. A proportionality constant of $0\farcs041$ (km s^{-1})$^{-1}$ is applied to the loci based off the maximum expansion rate ($\sim$ 0.15 % yr^{-1}) estimated by Katsuda et al. (2010). Panels (b) and (c) show those knots located only in the northern and southern hemispheres, respectively.

3.6 References

Badenes, C., Borkowski, K. J., Hughes, J. P., Hwang, U., & Bravo, E. 2006, ApJ, 645, 1373

Decourchelle, A., Sauvageot, J. L., Audard, M., et al. 2001, A&A, 365, L218

Fang, J., Yu, H., & Zhang, L. 2018, MNRAS, 474, 2544

Ferrand, G., Warren, D. C., Ono, M., et al. 2019, ApJ, 877, 136

—. 2021, ApJ, 906, 93

Fink, M., Kromer, M., Seitenzahl, I. R., et al. 2014, MNRAS, 438, 1762

Foight, D. R., Güver, T., Özel, F., & Slane, P. O. 2016, ApJ, 826, 66

Hayato, A., Yamaguchi, H., Tamagawa, T., et al. 2010, ApJ, 725, 894

Hwang, U., Hughes, J. P., & Petre, R. 1998, ApJ, 497, 833

Ihara, Y., Ozaki, J., Doi, M., et al. 2007, PASJ, 59, 811

Ishibashi, K., Dewey, D., Huenemoerder, D. P., & Testa, P. 2006, ApJL, 644, L117

Katsuda, S., Petre, R., Hughes, J. P., et al. 2010, ApJ, 709, 1387

Kerzendorf, W. E., Long, K. S., Winkler, P. F., & Do, T. 2018, MNRAS, 479, 5696

Kerzendorf, W. E., Yong, D., Schmidt, B. P., et al. 2013, ApJ, 774, 99

Krause, O., Birkmann, S. M., Usuda, T., et al. 2008a, Science, 320, 1195

Krause, O., Tanaka, M., Usuda, T., et al. 2008b, Nature, 456, 617

Marshall, H. L., Dewey, D., & Ishibashi, K. 2004, in Society of Photo-Optical Instrumentation Engineers (SPIE) Conference Series, Vol. 5165, X-Ray and Gamma-Ray Instrumentation for Astronomy XIII, ed. K. A. Flanagan & O. H. W. Siegmund, 457–468

Millard, M. J., Bhalerao, J., Park, S., et al. 2020, ApJ, 893, 98

Ruiz-Lapuente, P., Comeron, F., Méndez, J., et al. 2004, Nature, 431, 1069

Sato, T., Bravo, E., Badenes, C., et al. 2020, ApJ, 890, 104

Sato, T., & Hughes, J. P. 2017a, ApJ, 840, 112

—. 2017b, ApJ, 845, 167

Sato, T., Hughes, J. P., Williams, B. J., & Morii, M. 2019, ApJ, 879, 64

Sato, T., Katsuda, S., Morii, M., et al. 2018, ApJ, 853, 46

Seitenzahl, I. R., Ciaraldi-Schoolmann, F., Röpke, F. K., et al. 2013, MNRAS, 429, 1156

Tanaka, T., Okuno, T., Uchida, H., et al. 2021, ApJL, 906, L3

Truelove, J. K., & McKee, C. F. 1999, ApJS, 120, 299

Vancura, O., Gorenstein, P., & Hughes, J. P. 1995, ApJ, 441, 680

Wang, C.-Y., & Chevalier, R. A. 2001, ApJ, 549, 1119

Wang, L., & Wheeler, J. C. 2008, ARA&A, 46, 433

Warren, J. S., Hughes, J. P., Badenes, C., et al. 2005, ApJ, 634, 376

Williams, B. J., Borkowski, K. J., Ghavamian, P., et al. 2013, ApJ, 770, 129

Williams, B. J., Katsuda, S., Cumbee, R., et al. 2020, ApJL, 898, L51

Williams, B. J., Coyle, N. M., Yamaguchi, H., et al. 2017, ApJ, 842, 28

Wilms, J., Allen, A., & McCray, R. 2000, ApJ, 542, 914

Yamaguchi, H., Hughes, J. P., Badenes, C., et al. 2017, ApJ, 834, 124

Yamaguchi, H., Eriksen, K. A., Badenes, C., et al. 2014, ApJ, 780, 136

CHAPTER 4

A Spectroscopic Study of Supernova Remnants with the Infrared Space Observatory

4.1 Introduction

Supernovae enrich the ISM by dispersing metal-rich ejecta created in the SN explosion into their surrounding environment. In the years following a CC–SN (since Type Ia SNe have not been observed to form dust), the ejecta cools quickly as it expands, allowing chemical reactions to take place, which leads to the creation of molecules and dust grains in the ejecta (Todini & Ferrara, 2001; Nozawa et al., 2003; Sarangi & Cherchneff, 2015; Sluder et al., 2018). The elements comprising these grains, including Si and O, will likely remain locked in dust until they encounter a strong reverse shock created by the interaction of the blast wave and the ISM, or the shock wave from a pulsar wind nebula (PWN). The ejecta are compressed and heated by the shock, causing ionization and destruction of the molecules and dust within. Once the ejecta cools to $\sim 10^2$ – 10^3 K, line emission from atomic fine-structure transitions is radiated in the FIR band. These emission lines originate from a rapidly expanding shell of ejecta and therefore are broadened due to the Doppler effect. The radiation from the surviving dust grains shows a blackbody-like spectrum (the so-called "grey-body"), where the overall flux level depends on the total mass of the dust.

It has yet to be determined if SNe are major sources of dust in the Universe. The large quantity of dust observed in high-redshift galaxies (Bertoldi et al., 2003; Laporte et al., 2017; Isaak et al., 2002; Hirashita et al., 2017) raises the fundamental astrophysical question on the origin of dust in the Universe, because the timescales

of dust formation in low-mass stellar winds are longer than the age of the Universe in that era. On the other hand, CC–SNe of massive stars may create dust on short timescales of $\lesssim$ several 10^6 yr (Morgan & Edmunds, 2003; Dwek & Arendt, 2008), and thus are compelling candidate sources for significant dust production in the early Universe.

In this work, we probed the ISO data archive for LWS spectra of SNRs. Although it has made significant contributions in the field of infrared astronomy, some archival ISO data sets have yet to be analyzed, including a substantial fraction of the LWS SNR observations. In these spectra, we search for Doppler-broadened atomic fine-structure emission lines due to high-speed ejecta that are also coincident with bright continuum emission from dust. Based on these emission lines and underlying FIR continuum, we study the characteristics of the shocked gas and dust. We present the results of our FIR spectroscopic study of 18 CC–SNRs. We also present our FIR emission line profile measurements for two Type Ia SNRs (Kepler and Tycho) in this work. Although Type Ia SNe would unlikely contribute to the dust budget of the early Universe, our measurements of FIR fine-structure emission line profiles may be helpful to search for unshocked ejecta in these historical Type Ia SNRs (which is beyond the scope of this work). We investigate our sample by comparing [O I] and [C II] line strengths in several SNRs interacting with molecular clouds with various shock models. Finally, we present previously unpublished LWS data of HII regions to compare their emission line profiles and ratios with those for SNRs. We show that several FIR line flux ratios may be useful to differentiate SNRs from HII regions in future SNR searches.

4.2 Observations and Data

4.2.1 Sample Selection

We searched the ISO data archive for LWS observations of SNRs. We identified 31 instances of observations where the data are unpublished, including 20 individual SNRs. Table 4.1 lists these observations. ISO LWS observations of SNRs that are not included in our sample are shown in Appendix B (Table B.1). For each observation in our sample, we selected the Highly Processed Data Products (HPDPs)[1] from the archive (Lloyd et al., 2003). We use the average values of the forward and reverse scans in our analysis. We also compare the unpublished LWS data from the HII regions W51, G159.6–18.5, and NGC 6334, and the planetary nebula (PN) NGC 6720, with the SNR spectra.

4.2.2 The LWS Spectra

The LWS consists of 10 subdetectors (SW1 – SW5 and LW1 – LW5), each covering a fraction of the total LWS wavelength range, 43 – 197 μm. These spectra are often "fractured" – the flux levels of some detectors do not match adjacent detectors by up to $\sim$ 10%. To align the flux levels between adjacent detectors, we scaled each subdetector spectrum based on the average flux of the overlapping wavebands such that the full broadband spectrum becomes continuous without any jump in flux density. This scaling negligibly affects the emission line profiles. However, the scaled overall flux level of the continuum may vary by up to a factor of $\sim$ 2. Since SNRs in our sample are diffuse emission sources, we applied the effective area correction for the extended sources (Gry et al., 2003) (Section 4.6). Application of the extended source correction causes the overall flux level of the spectrum to be reduced by up to 40%. In Figure 4.1, we show an example of the LWS spectrum before and after the

[1] https://www.cosmos.esa.int/web/ISO/highly-processed-data-products

flux scaling and application of extended source correction. Figures 4.2 – 4.24 show the resulting minimum broadband LWS spectrum of each SNR and HII region in our sample, along with the pointing position and aperture (80″ diameter) overlaid on an infrared image of the SNR from Herschel, Spitzer, or Wide-field Infrared Survey Explorer (WISE) observations. The line fluxes are listed in Table 4.2 and the changes in the fluxes between the minimum and maximum broad-band spectra are less than 1%.

We found that some flux values in the LWS spectra have zero uncertainties. The wavelengths at which these zero flux uncertainties appear vary depending on the observation. Their origin is unclear, although they may originate from glitches in the detector photocurrent. In some cases, these fluxes were in regions of interest (at wavelengths corresponding to identified emission lines) in the LWS spectra. Since these values were consistent with the fluxes that have non-zero uncertainties, instead of removing them, we assigned the largest uncertainty value in the subdetector spectrum to these fluxes.

4.3 Detected Line Profiles

The candidate atomic fine-structure emission lines are approximately Gaussian in shape and the underlying continuum is roughly linear over small wavelength ranges. Thus, we fit the narrow-band spectrum of each line with a Gaussian + linear component model (Levenberg–Marquardt algorithm) using the Python package "LMFIT" (Newville et al., 2014). These narrow-band line spectra and best–fit models are plotted in Figure 4.25, and our results are summarized in Table 4.2. We clearly detect atomic fine-structure emission lines from [C II] at 158 μm, [N II] at 122 μm, [O I] at 63 and 145 μm, and [O III] at 52 and 88 μm in several remnants. On several occasions, the [O I] 63 and 145 μm and [O III] 88 μm lines are detected in adjacent

subdetectors. The SW3 subdetector always covers the [O I] 63 μm band, while its adjacent subdetector (SW2) covers this band only in a few observations. For the [O I] 145 μm line, while both the LW3 and LW4 subdetectors always cover the wavelength band of interest, LW4 consistently provides better signal-to-noise (S/N). The [O III] 88 μm line is detected with both the SW5 and LW1 detectors. The SW5 detector provides roughly twice the resolving power of LW1 (Table 4.7). Therefore, we report the [O I] 63 and 145 μm and [O III] 88 μm line measurements detected with the SW3, LW4, and SW5 subdetectors, respectively. In a few cases, the data quality is poor in these detectors, so we instead report measurements using the adjacent subdetector. We note these exceptions in Table 4.2.

A clear signature of emission lines emanating from fast-moving ejecta gas from a SN is their significant Doppler broadening, which may be detected in the ISO LWS spectra of SNRs. To calculate the velocity broadening (B) of each emission line, we remove the effect of the instrumental broadening through the relation, $B_{Line} = \sqrt{B_{Obs}^2 - B_{LWS}^2}$, where B_{Obs} is the observed full width at half maximum (FWHM) of the emission line, B_{LWS} is the instrument resolution of the LWS detector (Table 4.7), and B_{Line} is the true FWHM of the line. We measure an apparent Doppler broadening of $B_{Line} \gtrsim 1000$ km s^{-1} for several emission lines, mostly from the 63 μm [O I] and 88 μm [O III] lines (see Figure 4.28 and Table 4.8). The detection of [C II] lines requires caution because [C II] 158 μm emission is the primary coolant in interstellar gas. Galactic plane surveys of the [C II] 158 μm line revealed ambient intensities of $\sim 10^{-5} - 10^{-4}$ erg s^{-1} cm^{-2} sr^{-1} (Bennett et al., 1994; Nakagawa et al., 1998; Pineda et al., 2013). Thus, our measured line profiles may be contaminated by emissions originating from along the line–of–sight, not associated with the SNR. Unfortunately, in most cases, no accompanying background observation is available to distinguish between the line–of–sight and SNR emission. Future on–off observations are required

to unambiguously determine if the [C II] emission belongs to the SNR. Nonetheless, a clear case of Doppler-broadening of the [C II] 158 μm line is in the Crab Nebula ($B_{Line} \sim 1800$ km s^{-1}). We also note that the Herschel spectroscopic observation of Kes 75 (G29.7-0.3) resolves the [C II] line into two components of narrow and broad (1300 – 1500 km s^{-1}) (Temim et al., 2019), while the ISO spectra indicate 8% broadening of this [C II] line. The Herschel Photodetector Array Camera and Spectrometer (PACS) resolution (∼240 km s^{-1}) at 158 μm is a factor of ∼5 superior to that of the ISO LWS (∼1100 km s^{-1}). The marginally detected broadening of the [C II] line in the LWS spectra may need to be verified (or disputed) by future follow–up observations.

4.4 High velocity SN Ejecta

We compared our measured FWHM values for the detected emission lines with the instrumental FWHM reported in the ISO LWS Handbook, ∼ 0.283 μm and ∼ 0.584 μm for lines detected with the SW and LW subdetectors (see Table 4.7, respectively (Gry et al., 2003). We note that these instrumental resolutions are consistent (within statistical uncertainties) with the line width measurements for our HII region sample and the planetary nebula NGC 6720 (see Table 4.3). For each emission line, we take the instrumental FWHM (B_{LWS}) to be the smaller value of either the FWHM reported in the ISO LWS Handbook or our measured FWHM of the emission line in NGC 6720 (Table 4.7). Note that the handbook provides only one number for each of SW and LW and the FWHM is expected to be a function of wavelength because the LWS is a grating instrument. We confirm that using either the ISO Handbook or our measured NGC 6720 values for the detector resolutions does not significantly affect our scientific conclusions.

We detect broad lines (up to $\sim$ 3000 km s^{-1}) in several SNRs including G21.5–0.9, G29.7–0.3, the Crab Nebula, and G320.4–1.2. The velocity profiles of a few representative cases are shown in Figure 4.28. We classify these SNRs into three groups based on the statistical significance of the measured intensity and broadening of at least one emission line in each SNR spectrum: i.e., – Group A: both a firm line detection with S/N $>$ 5 and a clear 5 σ broadening detection, Group B: the line is firmly detected (S/N $>$ 5), but the broadening is marginal ($<$ 5 σ), and Group C: the lines appear to be broad, but the line detection is marginal (3 $<$ S/N $<$ 5), or show a marginal broadening only in the [C II] 158 μm line. In Table 4.8, we summarize these results.

The spectrum of the Crab Nebula (see Figure 4.28) shows clear evidence of broad emission lines from high-speed ejecta. Its spectrum exhibits double–peaked line features (Figure 4.25, [O III] 88 μm), indicating both blue- and red-shifted emission components expanding along the line of sight. In fact, all detected emission lines (i.e., 52 and 88 [O III], 63 and 145 [O I], 122 [N II], and 158 [C II]) from its spectra are broad, with line widths of $B_{Line} \sim$ 2000–3000 km s^{-1}. The 88 μm [O III] line in G320.4–1.2 shows an asymmetrical broadening, which may also suggest double–peaks with differential blue and red shifts (Figure 4.28). Below, we discuss individual SNRs with evidence of ejecta emission in detail.

G21.5–0.9 – Observations of the PWN with the Herschel PACS detector revealed broad [O I] 63 μm and [C II] 158 μm lines with measured FWHMs of 850 km s^{-1} and 1000 km s^{-1}, respectively, indicating the presence of PWN-shocked ejecta (Hattori et al., 2020; Cha et al., 2021). The LWS pointing encompasses almost all of the IR emission of the PWN (see Figure 4.4). The FIR lines at 63 [O I] 122 [N II], and 145 [O I] show broadening (Table 4.2, Figure 4.25). The broadening at 63 μm is firmly detected, thus we classify the detection into Group A, indicating that the

emission likely originates from fast-moving ejecta. Our estimates of the [O I] 63 μm and 145 μm line FWHMs of $\sim$ 900 km s^{-1}, are consistent with the measured values from the Herschel PACS observations.

G29.7–0.3 – Herschel PACS observations of the PWN showed narrow and broad components for each of the [O I] 63 μm, [O III] 88 μm, and [C II] 158 μm emission lines (Temim et al., 2019). Temim et al. (2019) attributed the narrow component to background emission, and estimated FWHMs of 1270 – 1570 km s^{-1} for the broad components, suggesting that the PWN shock is interacting with ejecta in the interior of the remnant.

The ISO LWS pointing covers the entirety of the PWN as seen in the FIR (Figure 4.5). We detect broad [N II] 122 μm and [O I] 145 μm lines. The broadening is firmly detected for the [N II] 122 μm (1200 km s^{-1}) and [O I] 145 μm (1300 km s^{-1}) lines (Group A). This is the first detection of [O I] 145 and [N II] 122 μm line broadening in this SNR. Our measured line widths are consistent with those detected at [O I] 63 and [O III] 88 μm based on the Herschel PACS data Temim et al. (2019).

G54.1+0.3 – Temim et al. (2010) suggested that the IR morphology is due to the PWN driving shocks into the expanding SN ejecta. Using Spitzer archival IRS, IRAC, and MIPS data, Rho et al. (2018) found dust emission spatially coincident with the ejecta line emission as traced by [Ar II]. In addition to Ar, they also detected atomic fine-structure emission from Ne, Cl, Si, and S. These lines are broadened, corresponding to velocities up to several 10^2 km s^{-1}. The [C II] line at 158 μm shows a slight, but statistically significant ($> 5\ \sigma$) broadening of $B_{Line} = 640$ km s^{-1}. However, the [C II] emission contribution from the remnant is unclear due to contamination from line–of–sight emission. Thus, we classify this SNR as Group C.

Crab Nebula – Gomez et al. (2012) showed that broad atomic lines observed with the ISO LWS correspond with resolved redshifted and blueshifted emission peaks

in the Herschel PACS spectra from a bright filament at the eastern side of the remnant. With the higher-resolution PACS data, they estimate that the redshifted and blueshifted emission peaks are in the velocity range of 1290 – 1750 km s^{-1}.

Here, our results are based on a pointing toward the northern part of the remnant (Figure 4.11). The [O III] 52 and 88 μm, [N III] 57 μm, [O I] 63 and 145 μm, [N II] 122 μm, and [C II] 158 μm lines are broad ($\sim$ 1800 – 3300 km s^{-1}, Table 4.2). The double–peaked structure due to red– and blue–shifted components is resolved in the LWS data for the [O III] 88 μm line (Figure 4.25). Applying a two–Gaussian + linear component model fit to this line gives line centroid values corresponding to $\pm$ 1000 km s^{-1}. The Crab Nebula exhibits the clearest case in our sample of broad line emission originating from high-speed ejecta.

G320.4–1.2 – Koo et al. (2011) reported a clump of gas near the PWN emitting a [Ne II] 12.81 μm line with a line-of-sight velocity of $\sim$ +1000 km s^{-1}, indicating SN ejecta. A recent X-ray proper motion study of compact ejecta knots located to the north of the pulsar (in the RCW 89 nebula) indicates high velocities up to 5000 km s^{-1} (Borkowski et al., 2020).

The LWS pointing is centered on the PWN, which shows a complicated structure of filaments in the Herschel 70 μm image (Figure 4.31). We detect [O I] 63 μm, [O III] 88 μm, [N II] 122 μm, and [C II] 158 μm emission lines. The 88 μm [O III] is broadened by $\sim$ 2000 km s^{-1} (Group A). Our detection of broad lines is consistent with similar high-speed ejecta emission reported in Koo et al. (2011) and Borkowski et al. (2020). G320.4–1.2 shows promising evidence for emission from both ejecta and dust from the same region (see Section 4.6 for a detailed discussion of the continuum emission).

RCW 103 – A previous ISO study found that the post-shock gas has low densities ($n_e \sim 10^3$ cm^{-3}) and abundances close to solar values, and thus no clear indication of ejecta emission (Oliva et al., 1999). A Chandra study found sparse

ejecta emission throughout SNR, with abundance values slightly above solar values (Frank et al., 2015).

We examined the ISO LWS spectra of two sub-regions within RCW 103, one near the SNR's center and the other at the bright southern shell (regions # 1 and # 3, respectively, see Figure 4.15). We extracted the background spectrum from another LWS data pointed at a region just outside of the southern shell of RCW 103 (region # 2, Figure 4.15). We find that the region # 3 spectrum clearly shows enhanced [O I] line emission at 63 μm above the background spectrum (see Table 4.2), which may be related to shock interactions with a molecular cloud (see Section 4.5). The central region (# 1) shows marginal evidence for line–broadening, however the line strengths are similar to (or even weaker than) those measured in the background region. Thus, the line–broadening is not compelling, and we classify this SNR as Group C.

E0102.2-7219 – Optical observations suggest the presence of fast-moving ejecta emitting [S II], [S III], [Ar III], and Hα and Hβ lines at speeds up to $\sim$ 1800 km s^{-1} (Seitenzahl et al., 2018). Rho et al. (2009) measured several mid-IR (MIR) emission lines from ejecta, including broad and lines which suggest velocity dispersion ranges of $\sim$ 2000 – 4000 km s^{-1}.

We measure a candidate broad [O III] 88 μm line, suggesting a velocity up to $\sim$ 1300 km s^{-1}. However, the broadening is statistically insignificant ($\sim$ 1 σ), and the line detection is marginal ($\sim$ 4 σ, Table 4.2). Thus, we classify this evidence into Group C.

N132D – Based on Spitzer IRS, IRAC, and MIPS data, Tappe et al. (2012) detected [Ne II] and [O IV] MIR lines from a fast-moving ejecta knot position, while the southeastern shell is dominated by ISM (Tappe et al., 2006). We detect the [O I] 63 μm and 145 μm lines. The [O I] 63 μm line appears to be broadened (a 3 σ detection, Group B). The implied velocity dispersion is $\sim$ 1500 km s^{-1}. If our suggested line

broadening would be confirmed with follow–up observations, this velocity would be in plausible agreement with kinematic studies of the optical [O III] ejecta which estimate expansion velocities up to $\sim$ 3000 km s^{-1} (Morse et al., 1995; Law et al., 2020).

N49 – Bilikova et al. (2007) estimated regional expansion velocities up to $\sim$ 500 km s^{-1} based on echelle spectra of Hα and [N II] emission lines, while X-ray observations indicate that N49 is enriched in Si and S (Park et al., 2003, 2012), as well as O and Ne (Zhou et al., 2019). We find marginal evidence for a broad [O III] 88 μm line (a 3 σ detection, Group C, Table 4.2). If confirmed, this broad [O III] line may be associated with the O–rich ejecta in this SNR.

0540-69.3 – Optical [O III] emission lines with velocity dispersions of $\sim$ 3000 km s^{-1} have been detected in 0540-69.3 (Mathewson et al., 1980; Kirshner et al., 1989). X-ray measurements hint at metal-rich ejecta in the southern part of the SNR (Park et al., 2010). Our best–fit to the [O III] 52 μm line suggests potential broadening ($\sim$ 2900 km s^{-1}). However, the line intensity and broadening are both measured with only 3 σ confidence (Group C). The line-center is also shifted by +1300 km s^{-1}, however, this shift is not detected in the [O III] 88 μm line.

Follow–up observations with higher spectral resolution (e.g., the Far Infrared Field-Imaging Line Spectrometer (FIFI-LS) on board the Stratospheric Observatory for Infrared Astronomy (SOFIA) or the proposed Origins Space Telescope (Leisawitz et al., 2021)) are required to firmly detect the candidate broad lines in G54.1+0.3, RCW 103, E0102.2–7219, N132D, N49, and 0540–69.3. Furthermore, due to the large aperture (diameter = 80″) of the LWS, constructing a detailed spatial distribution of ejecta emission in SNRs of our sample is not feasible. Establishing the spatial associations between ejecta and dust emission features based on high–resolution imaging is necessary to test the dust formation in the SN ejecta.

4.5 SNRs Interacting with Molecular Clouds

4.5.1 Diagnostic Line Results

Progenitors of CC–SN burn through their fuel in relatively short time periods, and therefore their SNRs may interact with the molecular clouds where they were born. The high expansion speed of the SNR drives a shock into the interacting MC. The radiative cooling of the shocked gas produces a number of molecular and atomic emission lines in IR bands.

The [O I] 63 μm and 145 μm, and [C II] 158 μm line strengths are useful diagnostics for the pre-shock density of the cloud and the speed of the shock that it encounters (Hollenbach & McKee, 1989). In general, two types of shock interactions are considered, i.e., a continuous (C)-type, or jump (J)-type shock. In a C-type shock, the shock front moves at a speed slower than the magnetosonic speed in the medium, and thus the gas conditions (e.g., temperature and density) change gradually. In a J-type shock, the shock front moves faster than the magnetosonic speed, and there is a sharp change in the gas temperature and density as the shock front moves through the medium. The type of shock affects the post-shock chemistry and overall dust destruction. Here, we aim to identify shock types from our measurements of FIR [O I] and [C II] lines in these MC-interacting SNRs.

Our sample includes SNRs W 28, IC 443, Kes 79, CTB 109, and RCW 103, for which the shock-MC interaction has been reported in literature (Tatematsu et al., 1990; Dickman et al., 1992; Rho & Petre, 1997; Arikawa et al., 1999; Stanimirović et al., 2003; Paron et al., 2006; Kilpatrick et al., 2016; Zhou et al., 2016). For SNRs Kes 79, CTB 109, and IC 443, the [O I] 63 μm band was observed with a raster map across the face of remnant. The raster maps allow for measurements of spatial variations in line strength across the remnant, whereby the locations of various shocks

can be identified. These raster map observations focus on narrow wavelength ranges of select emission lines, not covering the full range of the LWS. The raster maps of IC 443 also include spectra of the [O I] 145 μm and [C II] 158 μm bands. The raster map narrow-band line spectra and our spectral model fits are shown in Figure 4.27, while Tables 4.4, 4.5, and 4.6 show the line profiles and best–fit results for Kes 79, CTB 109, and IC 443, respectively. Figure 4.29 shows the radial distribution of line intensity for each of the raster observations of the molecular-cloud interacting SNRs in our sample. In Figure 4.29, we also overlay the published radial distribution of the [O I] 63 um line intensity across the northeastern shell of IC 443 (Rho et al., 2001).

The raster map of Kes 79 consists of 9 observations, each separated by 1 arcmin, which extend across the eastern boundary (see Figure 4.6) of the remnant. The [O I] 63 μm line intensities are consistent with the mean, $I_{63\mu m} = 6.4 \times 10^{-5}$), to within 3 σ uncertainties. Thus, there is no clear emission enhancement between regions inside the boundary of the remnant versus outside of it.

The CTB 109 raster map (see Figure 4.8) consists of 11 observations positioned across the northwest quadrant of the remnant, with 3 arcmin spacing between each pointing. We note the lowest line fluxes in regions 5 — 7 located inside the boundary of the remnant, and highest near of the western perimeter. The dimmer regions roughly coincide with the location of a CO arm that reaches across the remnant (Kothes et al., 2002), which could indicate that the emission is being absorbed by a foreground MC.

The raster map of IC 443 consists of 9 observations spaced 3 arcmin apart, from the geometric center of the remnant to outside the southern shell (see Figures 4.12 and 4.29:Upper). The [O I] 63 μm, 145 μm and [C II] 158 μm lines are strongest at a bright IR ridge in the southern shell (position 5), $I_{63\mu m} = 9.7 \pm 0.4 \times 10^{-4}$, and weakest at the position exterior to the boundary of the remnant (position 1), $I_{63\mu m} = 0.35 \pm 0.07 \times 10^{-4}$

cm^{-2} s^{-1} sr^{-1}. The [O I] emission peaks at the southern shell (more than an order of magnitude higher than the background intensity), indicating significant cooling from the SNR shocks encountering dense MCs. Similar sharp increases in line intensity are present in LWS observations of W44 and 3C391 (Reach & Rho, 1996). IC 443 was also observed using single (non–raster) pointings directed at the southeastern (# 1), eastern (# 2), and western (# 3) boundaries of the remnant (see Table 4.2). The strongest [O I] and [C II] emission is observed at the southeast position. We note that [N II] lines from IC 443 show somewhat high velocity (2000 – 3000 km s^{-1}), but the significance of the detection is less than 5 σ. Higher resolution spectroscopy is required to resolve if the [N II] lines are truly broad.

RCW 103 and W 28 were observed with non–raster LWS pointings. RCW 103 is close to the Galactic plane ($b = -0.4°$). After background subtraction using a separate background pointing (# 2), nearly all of the [C II] is removed from the central (# 1) and southern border (# 3) spectra (see Figure 4.15). At the central region, the [O I] line strength is also reduced significantly. However, at the southern ridge the [O I] flux remains high, $I_{63\mu m} = 3.7^{+0.5}_{-0.5} \times 10^{-4}$. We note that the background emission around RCW 103 is non-uniform with a complex morphology, which may imply a significant spatial variation in the background intensity. Thus, our estimated background–subtracted flux of the [O I] line should be considered with caution. For W 28, there is no background observation. Since it is located close to the Galactic plane ($b = -0.1°$), the observed line intensity may be mixed with a significant amount of line-of-sight emission.

4.5.2 SNR–MC Interactions and Shock Models

Below we briefly overview previously documented evidence of MC interactions for the relevant SNRs in our sample, and discuss our results for each remnant. Our

estimated shock conditions based on the [O I] and [C II] emission for each of the MC–interacting SNRs are listed in Table 4.9 and the observed line fluxes are compared with shock models in Figure 4.30.

IC 443 – The MC interactions with IC 443 have been well studied. Shocked molecular gas was first detected toward the southern region of IC 443 with CO(1–0) observations that showed 20 km s^{-1} line widths (Denoyer, 1979). Since then, several different molecular species have been used as tracers to study the shock-cloud interactions in the SNR (Burton et al., 1988; Dickman et al., 1992; van Dishoeck et al., 1993; Snell et al., 2005; Reach et al., 2019; Kokusho et al., 2020). The importance of the FIR 63 μm line of [O I] as a shock diagnostic tool was demonstrated using an observation from the Kuiper Airborne Observatory, where the [O I] emission was found to correlate well with the near–IR H_2 emission (Burton et al., 1990). The [O I] 63 μm line strength was also used to determine the nature of the shocked gas in the northeast (Rho et al., 2001). Rho et al. (2001) observed IC 443 with ISO LWS raster line spectra across the northeastern rim of the remnant and reported similar peak [O I] 63 μm line brightness values ($\sim 5 \times 10^{-4}$) to ours. Based on strong 2MASS K_s-band emission (associated with H_2 line emission) relative to the J and H bands, they suggested that the southern shell is dominated by a slow continuous C–shock, with a shock speed $v_s \sim 30$ km s^{-1} and preshock hydrogen density, $n_o \sim 10^4$ cm^{-3} (as also concluded by Cesarsky et al. (1999)).

We compare our observed line brightness with C- and J- shock models. We reproduce the J–shock model calculations of line fluxes based on Figure 7 of Hollenbach & McKee (1989)[2]. For the C–shock models, we run the Paris–Durham code (Godard et al., 2019)[3] and produce the predicted line intensities depending on den-

[2]https://automeris.io/WebPlotDigitizer/

[3]https://ism.obspm.fr/shock.html

sity and shock velocities. We overview the Paris–Durham code in Appendix B, and present our input parameters in Table B.2. Our C–shock models assume a young shock age of 10^3 years, while the J–shock models assume the shock has reached a steady-state. Increasing the shock age of the C–shock models to 10^4 years (nearly reaching a steady-state) enhances the predicted [O I] and [C II] intensities by a factor of a few, but does not affect our conclusions. Figure 4.30 shows the calculated line intensities for various preshock densities ($10^3 - 10^6$ cm^{-3}) and shock speeds (5 – 150 km s^{-1}) for C–shock and J–shock models.

Our observed [O I] line brightness values in IC 443 are consistent with the lower density (10^3 cm^{-3}) fast (80 km s^{-1}) J–shock models from Hollenbach & McKee (1989). However, when we account for the large beam of the ISO LWS the true surface brightness may be a factor of a few smaller than the observed brightness. In this case, we find that a C–shock solution for the higher density (10^5–10^6 cm^{-3}) and slow (30 or 10 km s^{-1}) shock models from the Paris–Durham code fits our measured [O I] line flux. The observed [C II] 158 μm line emission can be reproduced only in the fast J–shock models, suggesting that at least some of the observed emission is due to this type of shock. It is difficult to firmly constrain the nature of the shock-cloud interaction in IC 443, and the presence of multiple shocks in the SNR is often invoked (see Snell et al. (2005) for a comprehensive review of possible shock-types). Recent IR line maps of IC 443 show that H_2 line emission (indicative of slower shocks) is mainly distributed along the southern ridge, while [Fe II] emission (representative of faster shocks) is present throughout the entire remnant (Kokusho et al., 2020). Thus, both slow shocks moving into a dense gas and fast shocks into a thinner gas may be present within the large aperture of the LWS in the southern portion of remnant.

Based on the allowed ranges of n_o and v_s, we estimate the ram pressure to be $p_{ram} = \rho v_s^2 \sim n_o v_s^2 \sim 10^{-7}$ dyne cm^{-2} at the bright [O I] and [C II] regions. From

X-ray measurements, we can estimate the thermal pressure of the remnant interior, $p_{th} = 2n_e kT_e$, where k is the Boltzmann constant, and n_e and T_e are the postshock electron density and temperature, respectively. Using the n_e and kT_e values reported by Troja et al. (2006), the thermal pressure is $\sim 10^{-9}$ dyne cm^{-2}. The ram pressure is more than two orders of magnitude higher than the thermal pressure, indicating that the shock is radiative. A similarly large difference in the ram and thermal pressure has been observed in other MC–interacting SNRs, W44 and 3C391 (Reach & Rho, 1996). Reach & Rho (1996) suggested that the higher ram pressures in regions with bright [O I] and [C II] suggests the presence of dense molecular clumps, while the comparatively low thermal pressures may be from X-ray gas at the interior where the density is relatively low.

RCW 103 – Observations of H_2 emission (Oliva et al., 1989; Burton & Spyromilio, 1993) and ^{12}CO $J = 1$–0 and HCO^+ lines (Paron et al., 2006) at the southern shell of RCW 103 indicate an interaction with an MC. The [O I] 63 μm line emission at the southern ridge has been observed with the IRS aboard Spitzer (Andersen et al., 2011), and previously with the ISO LWS (Oliva et al., 1999), with estimated intensity values of 3.2×10^{-4} and 6.0×10^{-4} ergs s^{-1} cm^{-2} sr^{-1}, respectively, roughly equivalent to our estimated value at region # 3 (5.3×10^{-4} ergs s^{-1} cm^{-2} sr^{-1}). Based on the strong [O I] 63 μm and 145 μm intensities at the southern ridge, the shock conditions are similar to those in IC 443, and may be the result of either a fast shock – low density or slow shock – high density scenario. However, the level of [C II] 158 μm emission in region # 2 is comparable to region # 3, suggesting that most of the [C II] 158 μm flux may originate from background. If the background–subtracted [C II] 158 μm emission is negligible, this is more consistent with the C–shock model with an initial shock speed $v_s \sim 10$ or 30 km s^{-1}, and preshock density $n_o = 10^5 - 10^6$ cm^{-3} (Figure 4.30c). The background region around RCW 103 is complicated and

the ambient [C II] 158 μm emission may vary across the remnant. If the [C II] line flux is truly significantly above the background flux, then there must exist a fast J-type component, similar to the scenario discussed in the case of IC 443. The lower right panel of Figure 4.15 shows the 2MASS J, H, and K_s band images of RCW 103. Filamentary emission from all three bands is visible at the southern boundary, with the K_s emission located to the exterior of J and H band emission. Region # 3 more closely coincides with the J and H band emission, suggesting that the region may be dominated more by C–shock conditions – a slower shock traversing into a dense medium. The estimated ram and thermal pressures are roughly equal at the southern ridge ($\sim 10^7$ dyne cm^{-2}), possibly due to dense CSM knots.

Kes 79 – Kes 79 is a several 10^3 yr–old (Zhou et al., 2016; Kuriki et al., 2018) double-shelled SNR, with a central compact object (Giacani et al., 2009). A broad OH absorption feature (Green, 1989) and bright HCO+ emission have been observed at the east and southeast boundary of Kes 79 near the local standard of rest velocity $V_{LSR} \sim 105$ km s^{-1}, consistent with the estimated distance to the SNR of 7.1 kpc based on the Galactic rotation curve (Green & Dewdney, 1992). The OH absorption and emission lines are detected both against Kes 79 and the associated pulsar B1849+00 (Stanimirović et al., 2003). The detection of OH lines in Kes 79 suggests an interaction with dense clouds. The detection of nearby CO clouds supports such SNR-cloud interactions (Kilpatrick et al., 2016). Zhou et al. (2016) found a broadened ^{12}CO J = 3–2 line ($\Delta v = 12$ km s^{-1}) along the east, south, and west of the SNR, suggesting MC interactions with the SNR shock. While the broad CO emission coincides with the southern and western radio shell (e.g., around 111 km s^{-1} component), the broad CO emission (e.g., at 103 km s^{-1}) in the east is a few tens of arcseconds to the west of the faint radio shell (Fig. 6d of Zhou et al., 2016). It indicates the interaction is at the front (around 103 km s^{-1}) of Kes 79 in the eastern direction.

The ISO pointings are slightly off the peak interacting sites (by up to a few tens of arcseconds) where the broad CO lines are detected. Thus, these ISO raster observations may cover only parts of the shock–clouds interacting regions. This is probably why the [O I] 63 μm emission does not show strong enhancement at a particular position but still relatively bright (a factor of 2–3 brighter than those of background emission in IC 443 raster or those of CTB 109). We consider that the ISO raster observations may not trace the strongest shock-cloud interacting regions.

CTB 109 – CTB 109 is a $\sim 10^4$ yr-old (Sánchez-Cruces et al., 2018) SNR. It is well-known for its semi-circular shape as seen in radio and X-rays, which has been attributed to the presence of a giant MC at its western boundary (Heydari-Malayeri et al., 1981; Tatematsu et al., 1987; Kothes et al., 2002). However, a search for broad ^{12}CO $J = 1$–0 emission, which would indicate interactions between the SNR shock and the cloud, resulted in no detection (Tatematsu et al., 1990). Our measurements show that the [O I] 63 μm emission is enhanced by a factor of ~ 2 (compared with the background emission to the north) in two regions along the western boundary (3 and 4). The emission is relatively weak, and not clearly indicative of a strong shock interaction (see Figure 4.29b).

W 28 – W 28 is a few 10^4 yr–old SNR (Velázquez et al., 2002) which exhibits both center-filled X-ray emission and a shell-like structure in radio, and thus belongs to the mixed-morphology class of SNRs (Wootten, 1981; Rho & Borkowski, 2002; Pannuti et al., 2017). Several molecular lines from H_2O, OH, and CO, and H_2 lines are detected in W 28, and are evidence of a shock passing through molecular gas (Reach & Rho, 1998; Arikawa et al., 1999; Reach & Rho, 2000). We detect [O I] 63 and 145 μm emission lines which appear which appears consistent with our C–shock model with a high preshock density ($10^4 - 10^6$ cm^{-3}) (see Figure 4.30f). We detect a [C II] 158 μm line that is exceptionally strong, which is consistent with a fast J–shock

model (Table 4.9). The difference in ram and thermal pressures is not as significant in W 28 (a factor of ~ 2) as in IC 443 (a factor of ~ 100). We note that, considering its projected position close to the Galactic plane ($b \sim -0.1°$), the contamination in our measured line flux from the strong Galactic background emission may be significant.

4.6 Continuum Emission in SNR G320.4–1.2

In the LWS spectra of several SNRs, we clearly detect the continuum emission in the FIR band (40 – 200 μm), originating from cold to warm dust grains. If the observed FIR continuum is associated with the SN ejecta gas, the dust emission spectrum is useful to constrain the dust production in these CC–SN explosions. A Herschel survey identified FIR emission from SNRs in the Galactic plane, and in a few cases, estimated the dust mass associated with SN ejecta (Chawner et al., 2019, 2020). Here we focus on SNR G320.4–1.2, which was not covered by the Herschel survey. The remnant shows a clearly broadened [O III] 88 μm line (Section 4.4, Figure 4.28) and a bright continuum (Figure 4.32). The presence of dust emission associated with high–velocity ejecta and the relatively reliable detector calibrations make this SNR the best candidate to analyze the continuum spectrum in order to constrain the dust mass produced by the SN.

To model the dust emission in this SNR, we fit the continuum spectrum (after the flux normalizations among the individual subdetectors were applied, see Section 4.2) with a blackbody (BB) model in the form of

$$F_\lambda = \frac{\kappa_\lambda B_\lambda(T) M_{dust}}{D^2}, \tag{4.1}$$

where F_λ is the flux at each wavelength, λ, κ is the dust mass absorption coefficient, B_λ is the Planck function at temperature T, and M_{dust} and D are the

dust mass and distance to the source, respectively. We assumed the distance of D = 5.2 kpc for G320.4-1.2 (Gaensler et al., 1999). The dust mass coefficient, κ_λ, is a function of wavelength:

$$\kappa_\lambda = \kappa_{\lambda_0} \left(\frac{\lambda_0}{\lambda} \right)^\beta . \tag{4.2}$$

We assume that the emission can be described by $\kappa_{\lambda_0} = 0.07$ m^2 kg^{-1} for λ_0 = 850 μm (James et al., 2002), and $\beta = 1.9$, similar to bulk interstellar dust (Planck Collaboration et al., 2014).

Because our spectrum is not background–subtracted, the observed continuum includes dust emission components from both the SNR and ISM, and thus we apply a two–component BB model. The warm component represents emission associated with the SNR, and the cold component accounts for cold dust in the ISM background emission (Reach et al., 1995; Boulanger et al., 1996; Lagache et al., 1998). Before fitting, we excised the emission lines from the spectrum, leaving only the underlying continuum. We found that, while the observed spectrum is overall well-described by the best–fit model (see Figure 4.32:Left), the fit is statistically poor ($\chi^2_\nu \sim 200$). We realized that the statistical uncertainties on a small fraction of the flux values in the spectrum ($\sim 5\%$ of the total data points) are exceptionally small (typically $\ll 1\%$ of the flux values), which are more than an order of magnitude smaller than the average fractional uncertainties on the rest of the flux values ($\sim 15\%$). This small fraction of data points contributes the total χ^2_ν almost entirely (by $\sim 98\%$). To mitigate this issue, we manually assign statistical uncertainties on these flux values, adopting the mean uncertainty values for all flux measurements in each subdetector. After this adjustment, the best–fit model significantly improves ($\chi^2_\nu \sim 4$).

Our best–fit dust temperatures and masses are 46 – 52 K and 0.03 – 0.06 $M_\odot$ for the warm component, and 17 – 20 K and 4 – 15 $M_\odot$ for the cold component. The quoted ranges of these estimates represent the systematic uncertainties due to flux normalizations among subdetectors. The statistical uncertainties are small, on the order of $\lesssim 2\%$. We note that when the SW1 subdetector is used as a baseline, the resulting fit is poorer, and the estimated dust mass is at least 2 times greater than those estimated with other subdetectors as the baseline. Because of this anomaly, we exclude it in our discussion hereafter. The warm component most likely represents the emission spectrum of the SN-created dust, for which we estimate the mass $\sim$ 0.03 – 0.06 $M_\odot$. Our best–fit temperature for the cold component is consistent with that for the background ISM dust temperature as measured in literature (Reach et al., 1995; Boulanger et al., 1996; Lagache et al., 1998).

Based on the ISO LWS spectrum, G320.4–1.2 is a promising candidate that shows dust emission originating from grains formed in SN ejecta. We clearly detect the [O III] 88 μm with a velocity dispersion of $\sim$ 2000 km s^{-1} indicative of high–velocity ejecta. We also clearly detect a warm (46 – 52 K) dust continuum associated with this SN ejecta feature. The ISO beam partially covers the intriguing MIR source, IRAS 15099–5856 (IRAS 15099 hereafter) located at (α_{2000}, δ_{2000}) = ($15^h13^m56\overset{s}{.}32$, $-59°07'40\overset{''}{.}9$) (Koo et al., 2011). IRAS 15099 contains a bright central source, IRS1, surrounded by diffuse fainter emission, with spiral filaments extending out to a few arcminutes (see Figure 4.31. While the origin of IRAS 15099 is unclear, Arendt (1991) suggested that the IR emission may result from dust heated by a hot plasma, or by the nearby O star, Muzzio 10.

Koo et al. (2011) fit the Spitzer IRS spectrum of IRS1 with several dust components, and found that most of the emission arises from crystalline olivine and amorphous silicate at T = 54 – 58 K. They found a total dust mass of 0.009±0.001

d^2_{4kpc} $M_\odot$ for IRS1. At a distance of 5.2 kpc, their estimated total dust mass becomes 0.015 $M_\odot$. We note that, due to the large angular diameter of the beam, it is unclear if the broad [O III] line that we detect is associated with the compact central emission of IRS1, or the surrounding diffuse emission. Thus, our estimated dust mass range is in plausible agreement with that by (Koo et al., 2011) roughly within a factor of $\sim$ 2.

To estimate the background–subtracted dust mass of IRAS 15099, we use the archival Herschel PACS (Poglitsch et al., 2010) HPDP images at 70 μm and 160 μm, and SPIRE (Griffin et al., 2010) Level 2.5 images at 250 μm, 350 μm, and 500 μm images of SNR G320.4–1.2 (Observation IDs: 1342203291, 1342203292). Since our Herschel extraction aperture diameter (206″) of our regions is larger than the beam size of the maps (FWHM $\leq$ 35.2″), we do not apply aperture corrections to the extracted spectral energy distribution (SED).

The emission associated with IRAS 15099 is most clearly visible at 70 μm (see Figure 4.31). The brightest feature is located at the position of IRS1, with spiral filaments that reach out several arcminutes. Emission associated with IRS1 is clearly detected at 160 μm. Koo et al. (2011) identified emission at 65 μm and 90 μm, but not at 140 μm or 160 μm with the AKARI FIS (Far Infrared Surveyor). Thus, we identify clear 160 μm emission from IRS1 for the first time. To measure the net flux from IRAS 15099, we chose a 206″ diameter aperture centered at (α_{2000}, δ_{2000}) = ($15^h13^m57^s.1980$, -59°07′39″.78) which covers the bulk of the 70 μm emission apparently associated with IRAS 15099. We chose ten background regions to the east and west of the remnant, exterior to the radio and X-ray shell. These regions are covered in the PACS and SPIRE images, and avoid the bright ISM emission to the north (see Figure 4.31). We estimate net flux densities of 108 ± 26.0 Jy, 56.3 ± 39.4 Jy, 19.2 ± 13.4 Jy, 7.1 ± 5.5 Jy, and 2.6 ± 2.0 Jy at 70 μm, 160 μm, 250 μm, 350 μm, and 500 μm,

respectively. The flux from the 206″ diameter aperture increases by about a factor of 3 – 4 over our ISO-measured flux. Scaling the aperture sizes between ISO and Herschel, we estimate a total dust mass of 0.1 – 0.2 $M_{\odot}$ for our Herschel-measured fluxes.

We fit the Herschel background–subtracted SED with a one-component BB model and estimate a total dust mass of 0.66 ± 0.06 $M_{\odot}$ at a temperature of 34 ± 0.6 K. This dust mass is highly dependent on background subtraction, which varies significantly in the region around G320.4–1.2. The discrepancy in the dust mass estimates based on the Herschel and ISO data may be attributed to these uncertainties. Follow–up observations with higher spatial and spectral resolutions, (e.g., with the James Webb Space Telescope (JWST) and SOFIA), are required to verify if the dust and ejecta emission are clearly correlated. Our estimate for the dust mass associated with ejecta in G320.4–1.2 is in line with the growing number of previously published dust mass estimates in CC–SNRs (see Table 4.8 for values and references).

4.7 SNR Comparison with HII Regions

We compare the FIR atomic line emission of the SNRs with the HII regions in our sample, W51, NGC 6334, and G159.6–18.5 (Table 4.3 and Figure 4.26). In W51 and NGC 6334, we detect a bright continuum and several emission lines, [O III] 52, 88 μm, [N III] 57 μm, [O I] 63, 145 μm, [N II] 122 μm, and [C II] 158 μm. In G159.6–18.5, we detect only the 158 μm [C II] line and weak continuum emission. We note that the [N III] 57 μm line is detected only in the HII regions, and not in the SNRs, although Reach & Rho (2000) found hints of a faint [N III] 57 μm line flux in W 28, W44, and 3C391 ($< 0.25 \times 10^{-4}$ ergs s^{-1} cm^{-1} sr^{-1}). In an ISO spectral survey of 45 compact HII regions, Peeters et al. (2002) reported clear [N III] 57 μm detections on ∼ 60% of the sample. The [N III] 57 μm/[N II] 122 μm ratio ranges from ∼ 1 – 10, suggesting

higher ionization states of nitrogen in the HII regions than in the SNRs. The lack of [N III] 57 μm detections in our SNR sample compared with the HII region sample of Peeters et al. (2002) indicates that the presence of strong [N III] 57 μm emission may be a discriminator between SNRs and HII regions.

4.8 Summary

We have studied the previously unpublished ISO LWS spectra of 20 SNRs in the Galaxy and Magellanic Clouds. We detect a number of FIR atomic fine-structure lines, including [O III] at 52 μm and 88 μm, [O I] at 63 μm and 145 μm, [N II] at 122 μm, and [C II] at 158 μm, as well as a bright continuum in several SNRs . We find that

- In several SNRs, we find evidence for broad [O I], [O III], and [N II] lines suggesting emission from high–velocity SN ejecta. We present for the first time a firmly detected broad [O III] 88 μm line in G320.4–1.2, indicative of fast-moving SN ejecta in this SNR. In G21.5–0.9, G29.7–0.3, and the Crab Nebula, we confirm previous detections of broad-line emission and present the lines that were not previously identified as broad in some cases.
- We find marginal evidence of broad lines in G54.1+0.3, RCW 103, E0102.2-7219, N132D, N49, and 0540–69.3. Follow–up high resolution imaging spectroscopy with modern instruments (e.g., SOFIA or JWST) is required to verify the presence of high velocity ejecta in these SNRs.
- Based on the [O I] emission from IC 443 and RCW 103, we find regions along the southern ridge in both SNRs where the SNR shock is likely interacting with a dense molecular cloud. The strong [C II] 158 μm emission in IC 443 indicates the presence of fast J-type shocks.

– We apply a two–component blackbody model fit to the LWS continuum of G320.4–1.2, and estimate a dust mass $\sim 0.1 - 0.2\ M_{\odot}$ and temperature of ~ 50 K associated with SN ejecta.

– We detect the [N III] 57 um line only in our HII region sample. This distinctive spectral characteristic may serve as a discriminator in the identification of HII regions and SNRs.

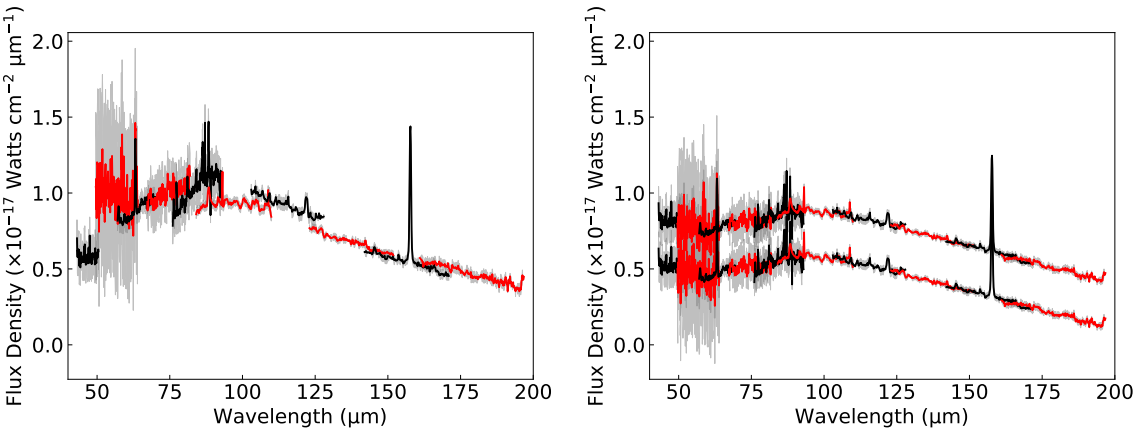

Figure 4.1: Left Panel: The ISO LWS spectrum of RCW 103 taken directly from the ISO Data Archive. The alternating red and black colors represent different subdetector spectra. Right Panel: The same spectrum as the left panel with the extended source correction and subdetector matching applied. Applying relative normalizations among the individual subdetector spectra results in a range of flux levels of the overall spectrum. The upper and lower bound flux levels are shown. The extended source corrections reduce the overall flux level by $\sim 30\%$ on average.

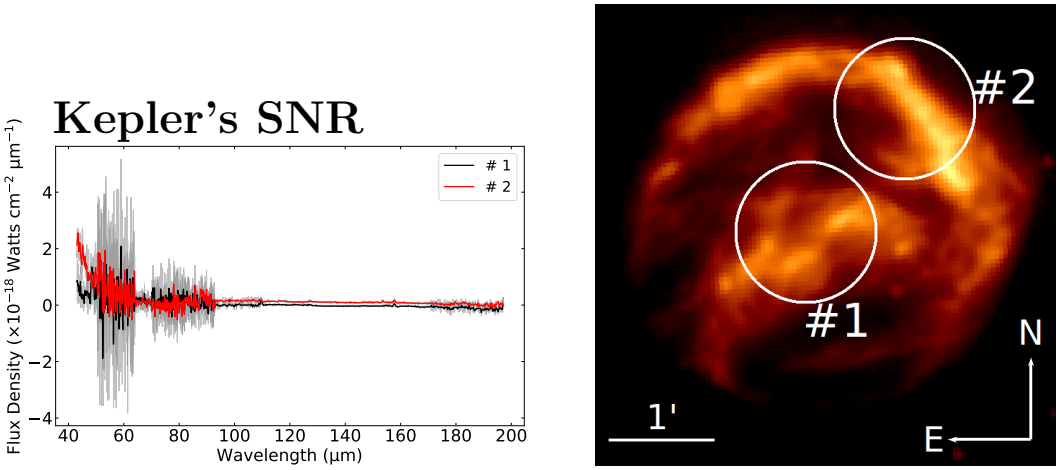

Figure 4.2: Left: The ISO LWS spectra of Kepler's SNR. Right: The Spitzer MIPS 24 μm image of Kepler's SNR. Two ISO LWS pointings are shown with white circles.

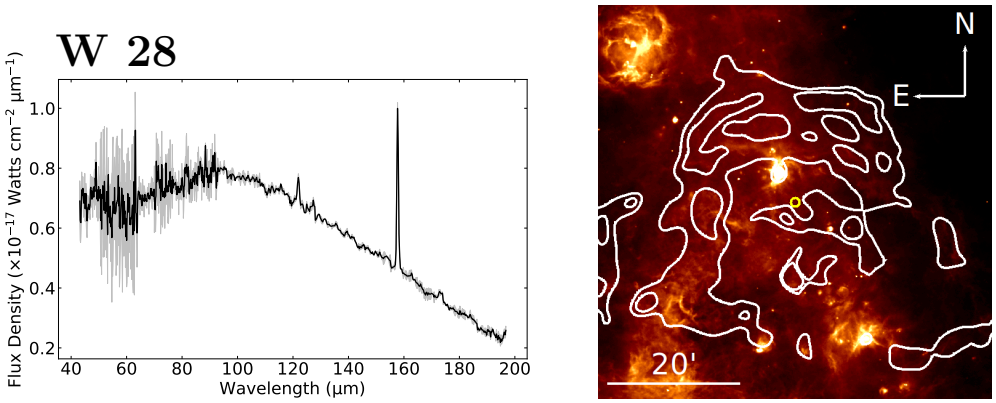

Figure 4.3: Left: The ISO LWS spectrum of W 28. Right: The Herschel PACS 70 μm image of W 28. The ISO LWS pointing is shown with a yellow circle. The white contours are from a VLA 325 MHz image.

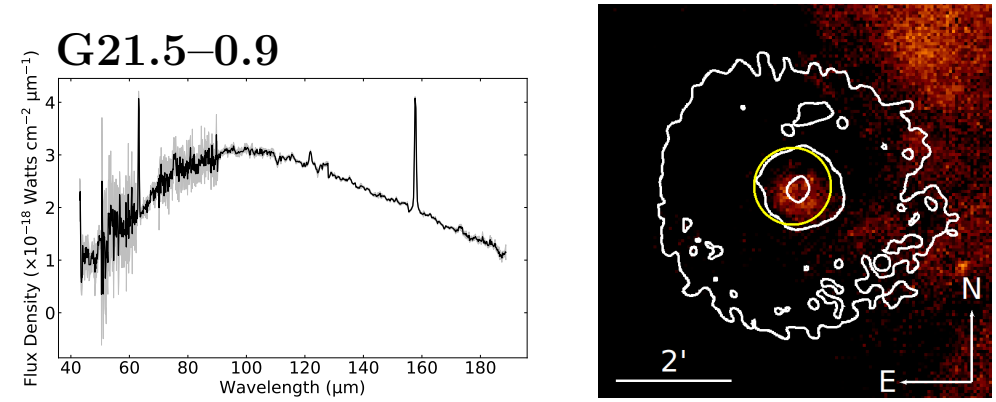

Figure 4.4: Left: The ISO LWS spectrum of G21.5–0.9. Right: The Herschel PACS 70 μm image of G21.5–0.9. The ISO LWS pointing is shown with a yellow circle. The white contours are from a Chandra (0.5 – 7.0 keV) image.

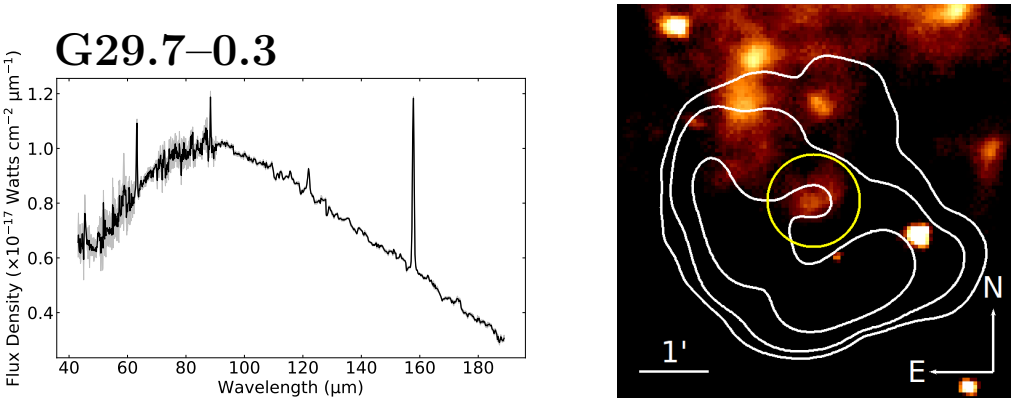

Figure 4.5: Left: The ISO LWS spectrum of G29.7–0.3. Right: The Herschel PACS 70 μm image of G29.7–0.3. The ISO LWS pointing is shown with a yellow circle. The white contours are from a VLA (1.4 GHz) image.

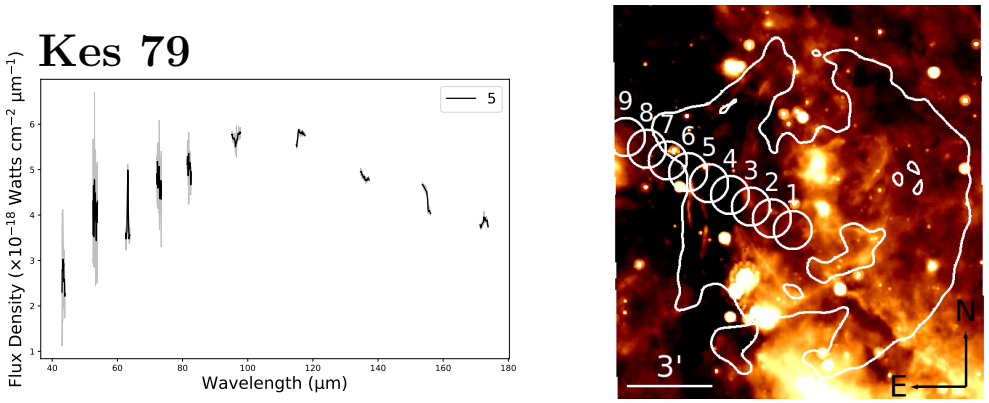

Figure 4.6: Left: The ISO LWS spectrum of Kes 79. Right: The Spitzer MIPS 24 μm image of Kes 79. The ISO LWS pointings are shown with white circles. The white contours are from a VLA (1.4 GHz) image. The raster spectra are shown in Figure 4.27.

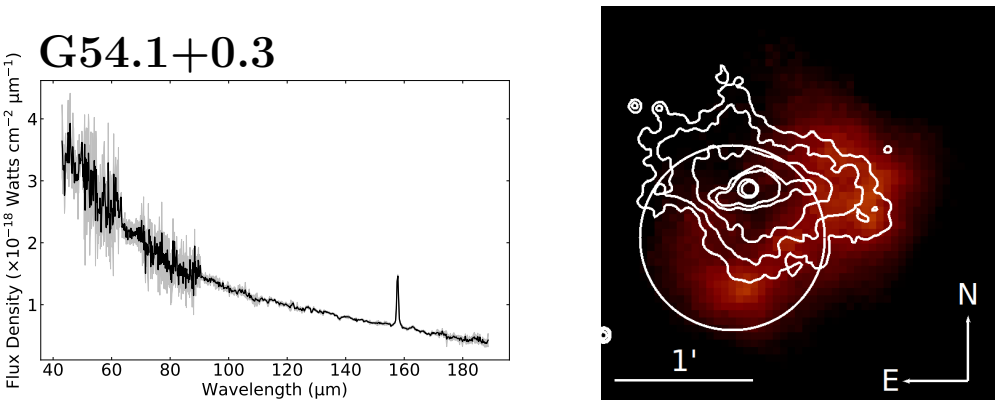

Figure 4.7: Left: The ISO LWS spectrum of G54.1+0.3. Right: The Herschel PACS 70 μm image of G54.1+0.3. The ISO LWS pointing is shown with a white circle. The white contours are from a Chandra (0.5 – 7.0 keV) image.

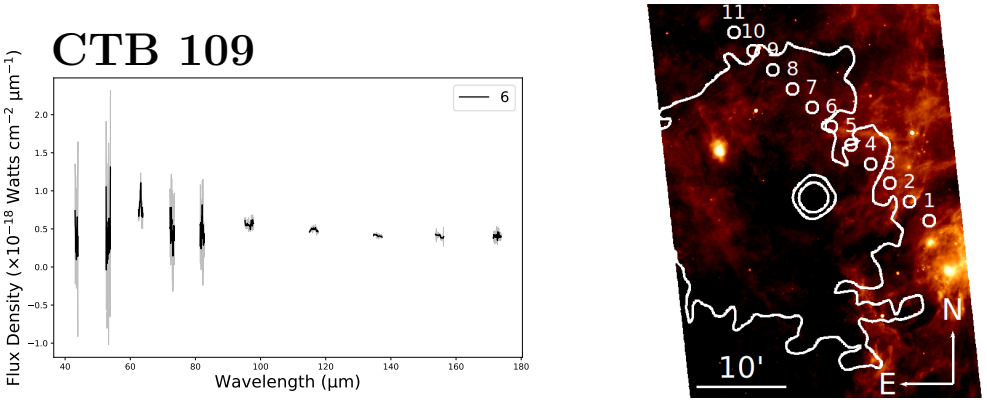

Figure 4.8: Left: The ISO LWS spectrum of CTB 109. Right: The Spitzer MIPS 24 μm image of CTB 109. The ISO LWS pointings are shown with white circles. The white contours are from an XMM-Newton (2.0 – 7.2 keV) image. The raster spectra are shown in Figure 4.27.

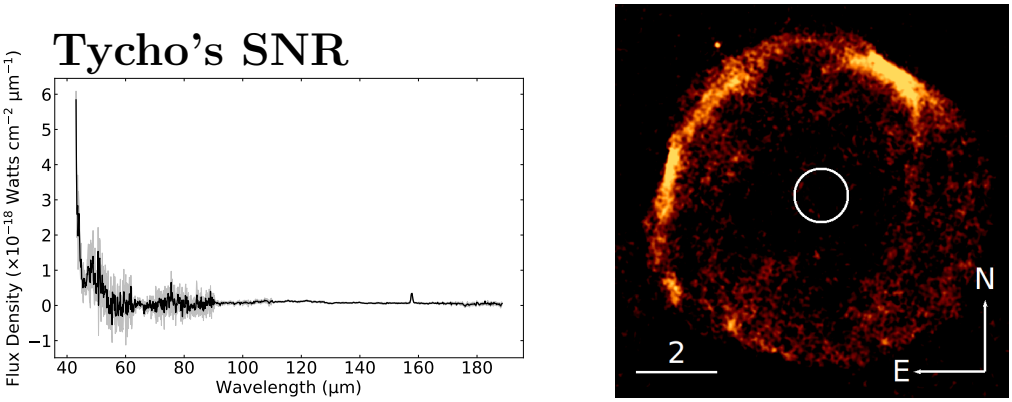

Figure 4.9: Left: The ISO LWS spectrum of Tycho's SNR. Right: The Herschel PACS 70 μm image of Tycho's SNR. The ISO LWS pointing is shown with a white circle.

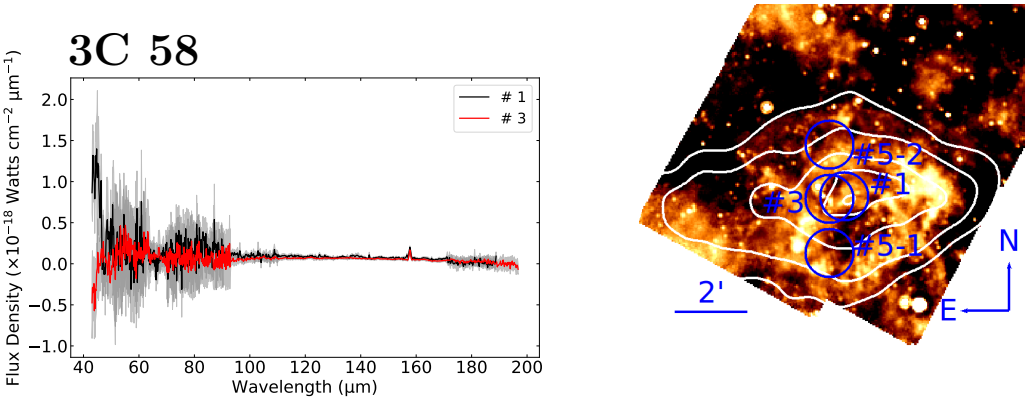

Figure 4.10: Left: The ISO LWS spectra of 3C 58. Right: The Spitzer MIPS 24 μm image of 3C 58. The ISO LWS pointings are shown with blue circles. The white contours are from a VLA (1.48 GHz) image.

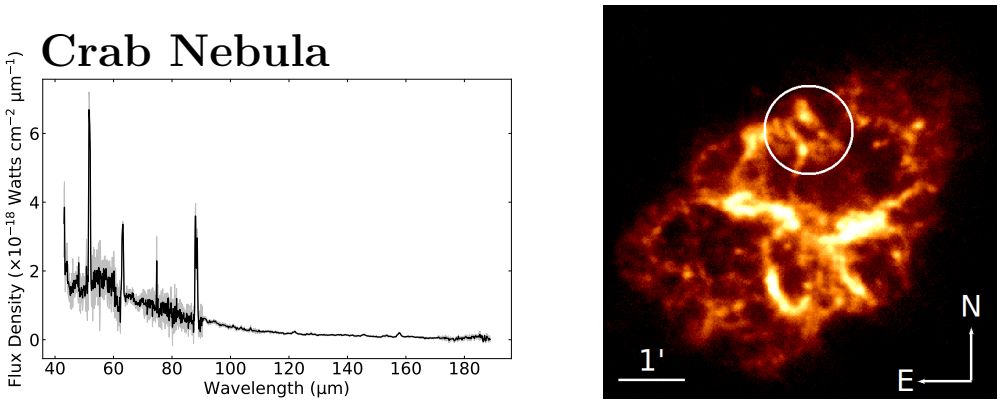

Figure 4.11: Left: The ISO LWS spectrum of Crab Nebula. Right: The Herschel PACS 70 μm image of the Crab Nebula. The ISO LWS pointing is shown with a white circle.

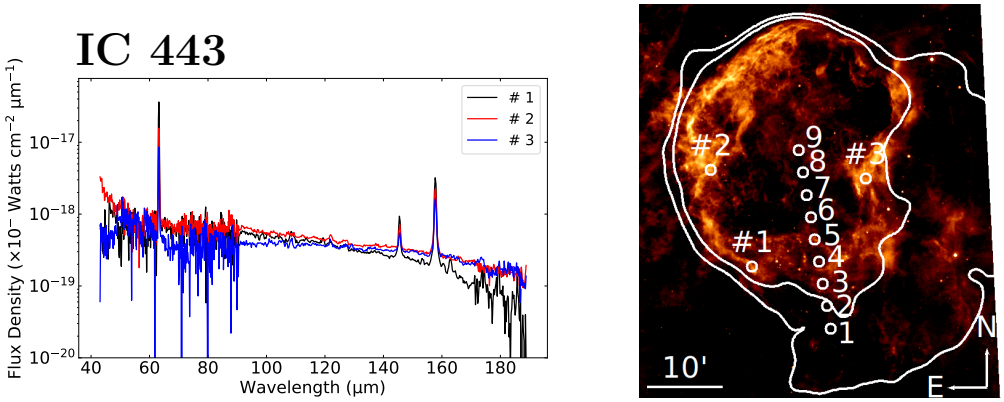

Figure 4.12: Left: The ISO LWS spectra of IC 443. Right: The Spitzer MIPS 24 μm image of IC 443. The ISO LWS pointings are shown with white circles. The raster line profiles are displayed in Figure 4.27. The white contours are from a VLA (330 MHz) image.

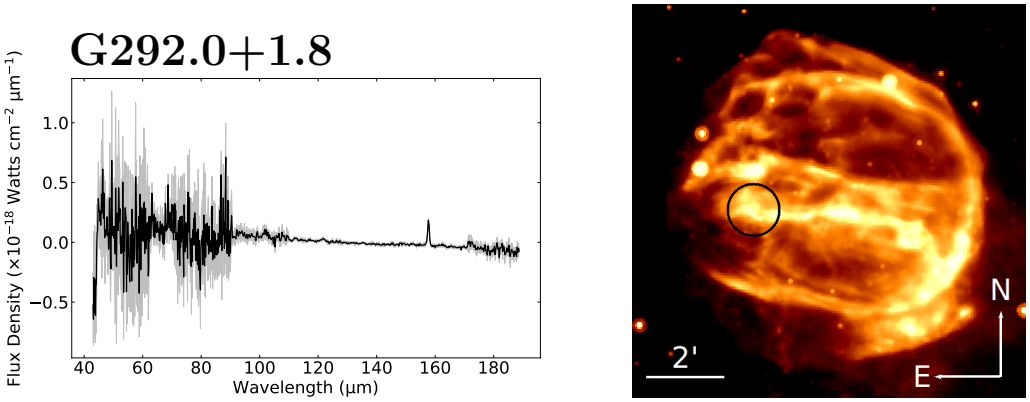

Figure 4.13: Left: The ISO LWS spectrum of G292.0+1.8. Right: The Spitzer MIPS 24 μm image of G292.0+1.8. The ISO LWS pointing is shown with a black circle.

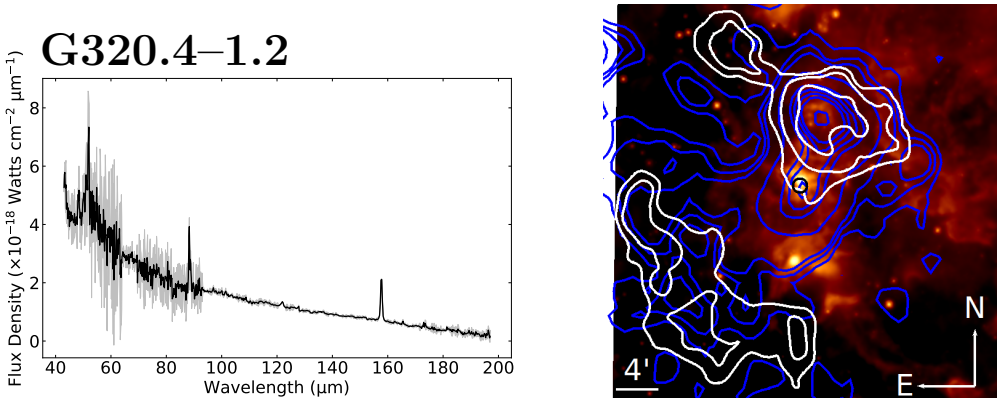

Figure 4.14: Left: The ISO LWS spectrum of G320.4–1.2. Right: The WISE 22 μm image of G320.4–1.2. The ISO LWS pointing is shown near the center with a black circle. The white contours are from a MOST (843 MHz) image. The blue contours are from a broadband ROSATimage.

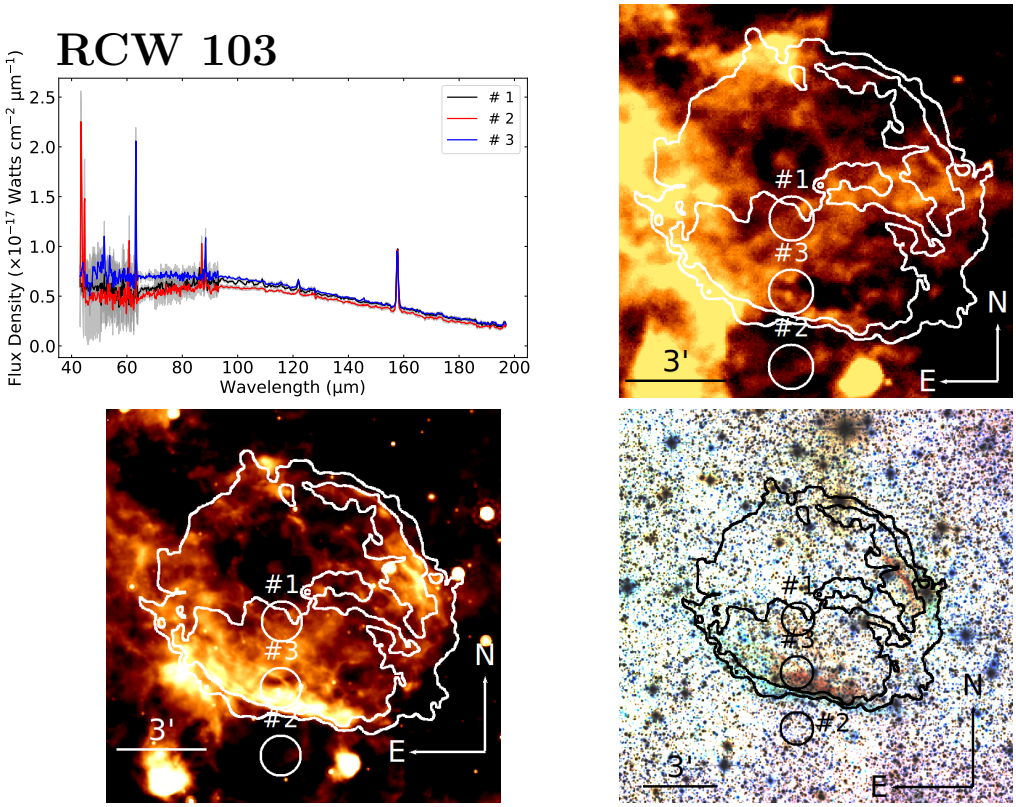

Figure 4.15: Upper Left: The ISO LWS spectra of RCW 103. Upper Right: The Herschel PACS 70 μm image of RCW 103. Lower Left: The Spitzer MIPS 24 μm image of RCW 103. Lower Right: The 3-color 2MASS image of RCW 103. The J, H, and K_s bands are shown in red, green, and blue, respectively. In all three image panels, the ISO LWS pointings are shown with white or black circles. The contours are from a Chandra (0.5 – 7.0 keV) image

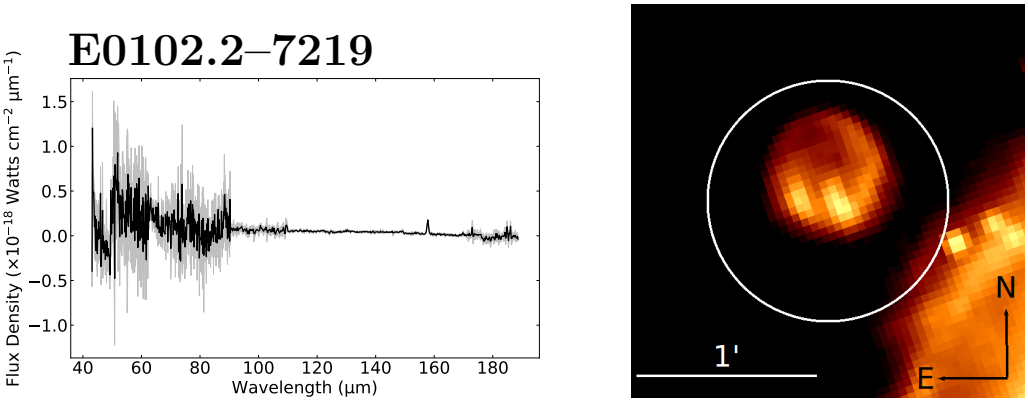

Figure 4.16: Left: The ISO LWS spectrum of E0102.2–7219. Right: The Spitzer MIPS 24 μm image of E0102.2-7219. The ISO LWS pointing is shown with a white circle.

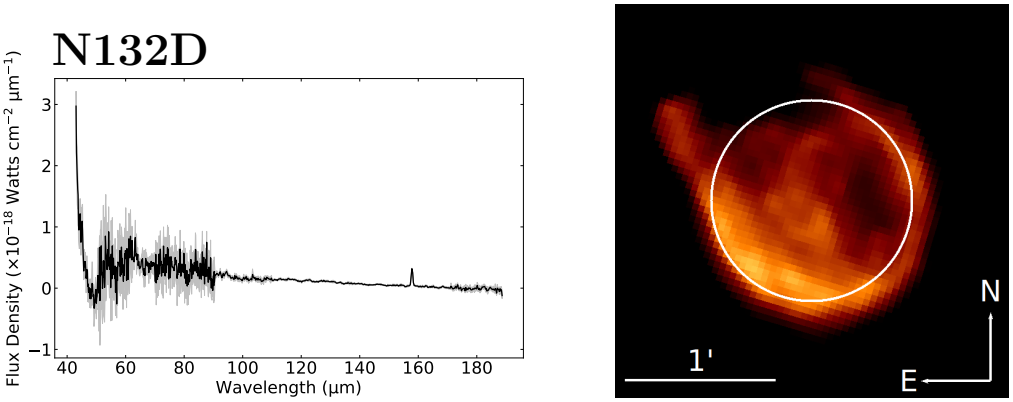

Figure 4.17: Left: The ISO LWS spectrum of N132D. Right: The Spitzer MIPS 24 μm image of N132D. The ISO LWS pointing is shown with a white circle.

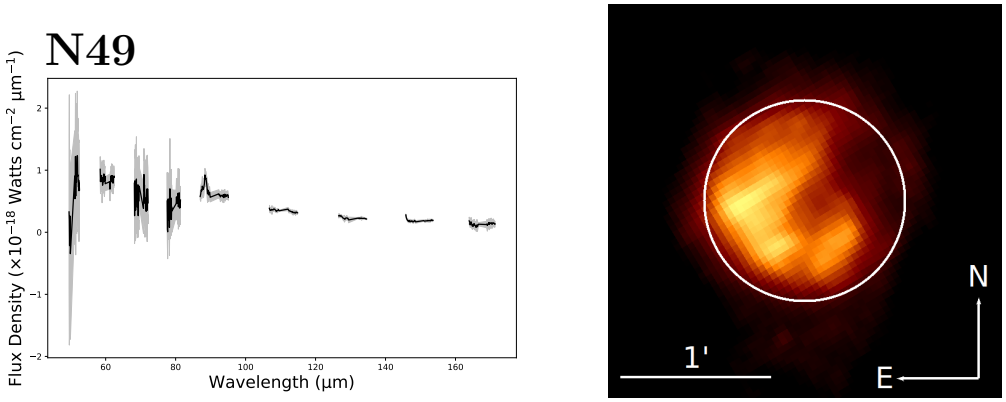

Figure 4.18: Left: The ISO LWS spectrum of N49. Right: The Spitzer MIPS 24 μm image of N49. The ISO LWS pointing is shown with a white circle.

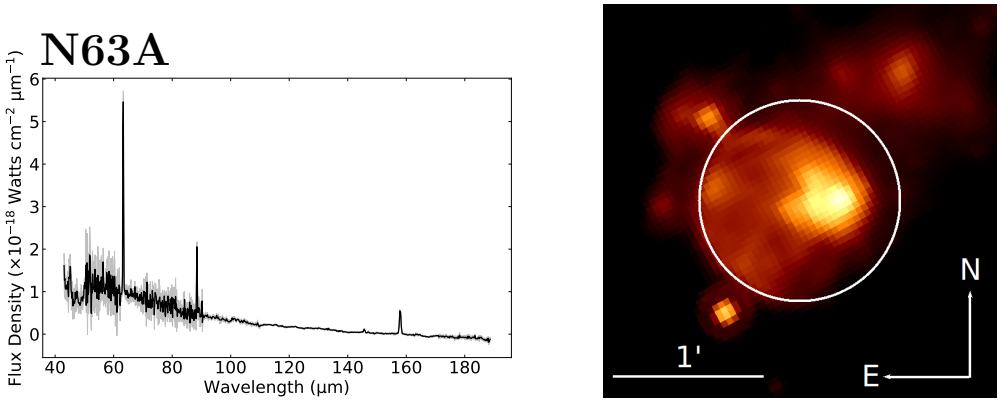

Figure 4.19: Left: The ISO LWS spectrum of N63A. Right: The Spitzer MIPS 24 μm image of N63A. The ISO LWS pointing is shown with a white circle.

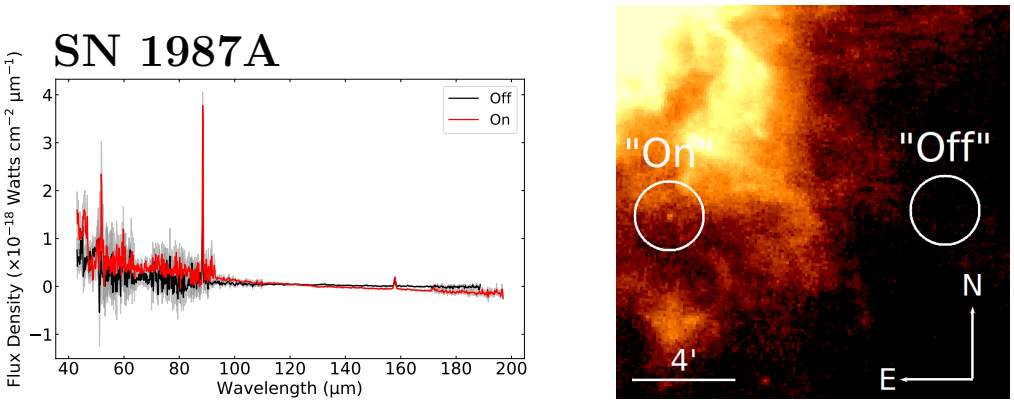

Figure 4.20: Left: The ISO LWS spectrum of SN 1987A. Right: The Herschel PACS 100 μm image of SN 1987A. The ISO LWS pointings are shown with white circles.

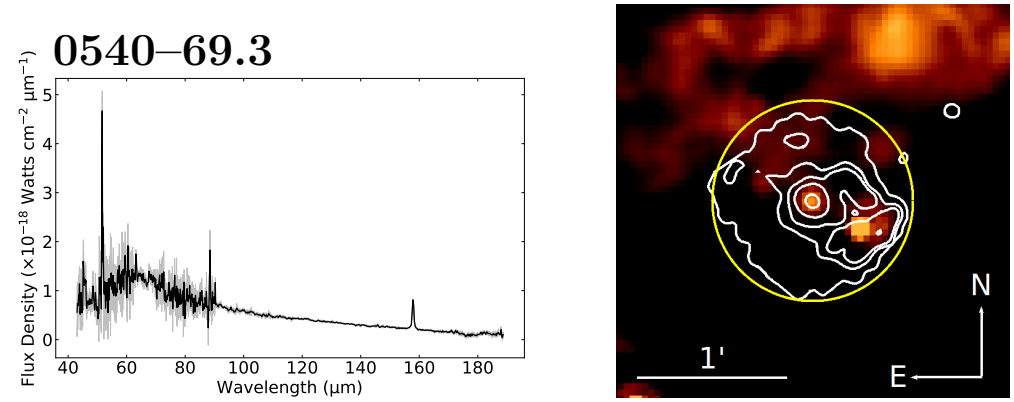

Figure 4.21: Left: The ISO LWS spectrum of 0540–69.3. Right: The Spitzer MIPS 24 μm image of 0540-69.3. The ISO LWS pointing is shown with a yellow circle. The white contours are from a Chandra (0.5 – 7.0 keV) image.

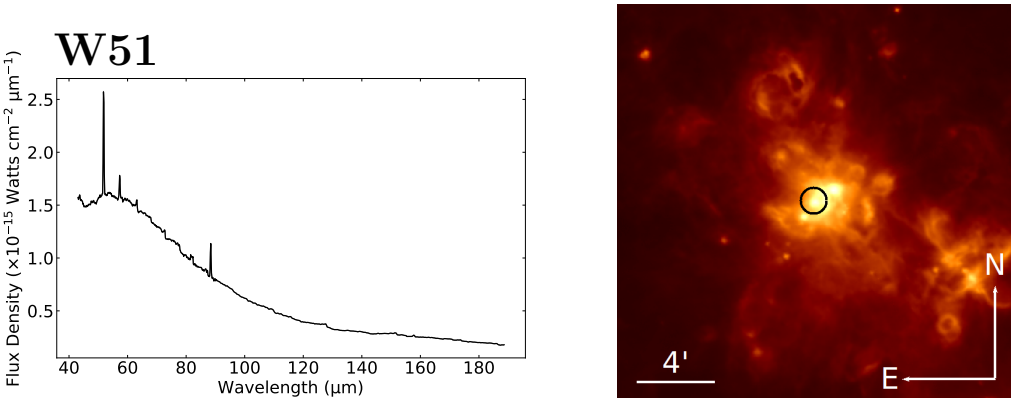

Figure 4.22: Left: The ISO LWS spectrum of W51. Right: The Herschel PACS 70 μm image of W51. The ISO LWS pointing is shown with a black circle.

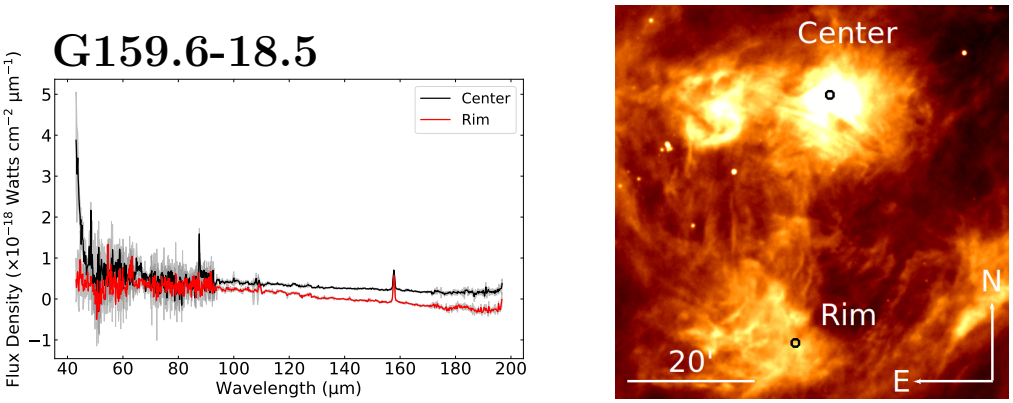

Figure 4.23: Left: The ISO LWS spectra of G159.6–18.5. Right: The WISE 22 μm image of G159.6–18.5. The ISO LWS pointings are shown with black circles.

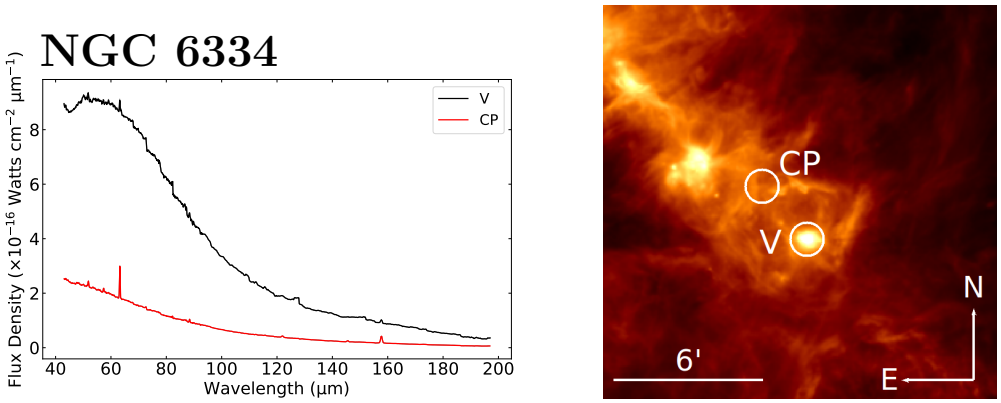

Figure 4.24: Left: The ISO LWS spectra of NGC 6334. Right: The Herschel PACS 70 μm image of NGC 6334. The ISO LWS pointings are shown with white circles.

Table 4.1. ISO LWS Observations of Our Sample of SNRs and HII Regions

Name	Target Name*	RA, DEC (J2000)	Date	t_{on} (s)	Publications	Figure
SNRs						
G4.5+6.8	Kepler # 1	$17^h30^m41^s.79$ $-21°29'29''.4$	1996-02-16	814	This Work	4.2
G4.5+6.8	Kepler # 2	$17^h30^m37^s.77$ $-21°28'19''.7$	1996-02-16	812	This Work	4.2
G6.4-0.1	W 28	$18^h00^m38^s.65$ $-23°25'03''.8$	1996-02-24	814	This Work	4.3
G21.5–0.9	G21.5–0.9	$18^h33^m34^s.08$ $-10°34'04''.7$	1996-10-11	1064	This Work	4.4
G29.7–0.3	G29.7–0.2	$18^h46^m25^s.19$ $-02°58'33''.9$	1997-10-31	1126	3, This Work	4.5
G33.6+0.1	Kes 79 (L02)	$18^h52^m54^s.00$ $+00°41'23''.9$	1996-10-04	1424	This Work	4.6
G54.1+0.3	G54.1+0.3	$19^h30^m30^s.69$ $+18°51'53''.1$	1996-04-24	1052	This Work	4.7
G109.1–01.0	CTB 109 (L02)	$23^h02^m17^s.27$ $+59°11'01''.43$	1997-02-23	1770	This Work	4.8
G120.1+1.4	Tycho #1	$00^h25^m18^s.97$ $+64°08'22''.06$	1997-02-15	1114	This Work	4.9
G130.7+3.1	3C 58 #1	$02^h05^m34^s.38$ $+64°49'49''.7$	1997-07-24	1126	This Work	4.10
G130.7+3.1	3C 58 #3	$02^h05^m38^s.21$ $+64°49'45''.1$	1998-03-13	4036	This Work	4.10
G130.7+3.1	3C 58 #5	$02^h05^m38^s.15$ $+64°48'14''.98$	1998-03-13	1332	This Work	4.10
G130.7+3.1	3C 58 Off (L02)	$02^h07^m20^s.20$ $+64°38'44''.99$	1998-03-13	608	This Work	4.10

Table 4.1 (cont'd)

Name	Target Name*	RA, DEC (J2000)	Date	t_{on} (s)	Publications	Figure
G184.6–05.8	Crab Nebula	$05^h34^m32^s.02$ $+22°02'04''.6$	1998-02-19	1126	This Work	4.11
G189.1+3.0	IC 443 # 1	$06^h17^m43^s.76$ $+22°21'59''.1$	1998-02-26	1126	1, 2, This Work	4.12
G189.1+3.0	IC 443 # 2	$06^h18^m7^s.45$ $+22°34'47''.42$s	1998-02-27	1126	2, This Work	4.12
G189.1+3.0	IC 443 # 3	$06^h16^m38^s.43$ $+22°33'36''.90$	1998-02-27	1126	2, This Work	4.12
G189.1+3.0	IC443 – R10E STR (L02)	$06^h17^m07^s.59$ $+22°25'34''.2$	1998-03-18	2710	This Work	4.12
G292.0+1.8	G292.0+1.8	$11^h24^m47^s.11$ $-59°15'44''.6$	1996-09-02	1064	This Work	4.13
G320.4–1.2	G320.3–1.2	$15^h13^m56^s.52$ $-59°08'10''.5$	1996-02-20	812	This Work	4.14
G332.4–0.4	RCW 103 #1	$16^h17^m41^s.84$ $-51°03'19''.8$	1996-02-14	812	This Work	4.15
G332.4–0.4	RCW 103 #2 (Off)	$16^h17^m42^s.04$ $-51°07'49''.7$	1996-02-14	814	This Work	4.15
G332.4-0.4	RCW 103 #3	$16^h17^m41^s.94$ $-51°05'34''.7$	1996-02-20	812	This Work	4.15
J0104.1–7201	SMC-E0102.2-7219	$01^h04^m02^s.16$ $-72°02'00''.5$	1996-04-22	1052	This Work	4.16
J0525.0–6938	LMC–N132D	$05^h25^m02^s.50$ $-69°38'38''.5$	1996-05-06	1054	This Work	4.17
J0526.0–6604	LMC–N49 (L02)	$05^h26^m00^s.57$ $-66°05'01''.7$	1997-06-16	950	This Work	4.18
J0535.7–6602	LMC–N63A	$05^h35^m43^s.15$ $-66°02'05''.8$	1996-04-29	1054	This Work	4.19

Table 4.1 (cont'd)

Name	Target Name*	RA, DEC (J2000)	Date	t_{on} (s)	Publications	Figure
J0535–6916	SN 1987A (Off)	$05^h34^m28^s.13$ –69°16′07″.3	1996-05-06	1052	This Work	4.20
J0535–6916	SN 1987A	$05^h35^m28^s.04$ –69°16′11″.6	1996-05-25	1552	2, This Work	4.20
J0535–6916	SN 1987A (L02)	$05^h35^m28^s.04$ –69°16′11″.7	1996-07-10	808	This Work	4.20
J0540.2–6920	LMC 0540–69.3	$05^h40^m11^s.13$ –69°19′54″.2	1996-05-06	1052	This Work	4.21
HII Regions						
G49.2–0.7	W51 FIR2	$19^h23^m44^s.10$ +14°30′33″.5	1997-04-24	2708	2, This Work	4.22
G159.6–18.5	G159 Center	$03^h39^m57^s.95$ +31°56′35″.5	1997-09-05	1180	This Work	4.23
G159.6–18.5	G159 Rim	$03^h40^m23^s.35$ +31°17′48″.1	1997-09-05	1180	This Work	4.23
G351.13–0.46	NGC6334 CP	$17^h20^m06^s.31$ –35°55′45″.80	1996-03-20	1110	This Work	4.24
G351.13–0.46	NGC6334 V	$17^h19^m57^s.36$ –35°57′52″.49	1996-03-20	1108	This Work	4.24
Planetary Nebulae						
G63.2+13.9	NGC6720	$18^h53^m35^s.68$ +33°01′40″.3	1996-11-16	1268	4, This Work	

Note. — 1. (Snell et al., 2005) 2. (Liseau et al., 2006) 3. (He et al., 2005) 4. (Liu et al., 2001)

*The majority of targets were observed in the L01 mode, which covered the full range of the LWS detector. A few targets were observed in the L02 mode, which covered only certain wavelength bands specified by the observer.

Table 4.2. Observed Spectral Lines from ISO LWS Spectra of Supernova Remnants

Target	Wavelength (μm)	Line	FWHM (%)[c] (μm)	Surface Brightness (10^{-4} ergs s^{-1}cm^{-2}sr^{-1})	Velocity[a] (km s^{-1})	Shift[b,k] (km s^{-1})
Kepler (#1)	$157.73^{+0.01}_{-0.01}$	[C II]	$0.55^{+0.04}_{-0.03}$	$0.06^{+0.02}_{-0.01}$	...	...
Kepler (#2) *(G4.5+6.8)*	[h]$157.74^{+0.02}_{-0.02}$	[C II]	$0.56^{+0.09}_{-0.06}$	$0.08^{+0.02}_{-0.02}$	...	...
W 28	[e]$63.15^{+0.01}_{-0.01}$	[O I]	$0.31^{+0.02}_{-0.02}$ (12^{+7}_{-7}%)	$1.3^{+0.2}_{-0.1}$	700^{+200}_{-200}	-160^{+60}_{-50}
(G6.4–0.1)	$121.92^{+0.02}_{-0.02}$	[N II]	$0.76^{+0.06}_{-0.05}$ (29^{+9}_{-8}%)	$0.8^{+0.2}_{-0.2}$	1200^{+200}_{-200}	...
	[e,i,g]$145.49^{+0.07}_{-0.04}$	[O I]	$0.60^{+0.09}_{-0.15}$	$0.14^{+0.09}_{-0.05}$	...	
	[g]$157.73^{+0.02}_{-0.02}$	[C II]	$0.74^{+0.03}_{-0.03}$ (27^{+5}_{-5}%)	$4.7^{+0.7}_{-0.4}$	870^{+90}_{-90}	...
G21.5–0.9	$63.21^{+0.01}_{-0.01}$	[O I]	$0.33^{+0.01}_{-0.01}$ (20^{+3}_{-3}%)	$1.06^{+0.08}_{-0.08}$	900^{+90}_{-80}	130^{+20}_{-20}
	[g]$121.83^{+0.03}_{-0.04}$	[N II]	$0.94^{+0.11}_{-0.09}$ (61^{+18}_{-15}%)	$0.32^{+0.06}_{-0.04}$	1800^{+400}_{-300}	-180^{+80}_{-100}
	[f]$145.59^{+0.04}_{-0.04}$	[O I]	$0.74^{+0.10}_{-0.09}$ (25^{+16}_{-16}%)	$0.10^{+0.02}_{-0.02}$	900^{+300}_{-300}	130^{+80}_{-90}
	[g]$157.76^{+0.01}_{-0.01}$	[C II]	$0.66^{+0.01}_{-0.01}$ (13^{+2}_{-2}%)	$1.35^{+0.05}_{-0.05}$	600^{+50}_{-50}	40^{+9}_{-9}
G29.7–0.3	$63.20^{+0.01}_{-0.01}$	[O I]	$0.29^{+0.02}_{-0.02}$	$1.08^{+0.16}_{-0.09}$	...	...
(Kes 75)	$88.39^{+0.01}_{-0.01}$	[O III]	$0.29^{+0.03}_{-0.03}$	$0.7^{+0.2}_{-0.2}$	...	140^{+40}_{-50}
	$121.96^{+0.01}_{-0.01}$	[N II]	$0.77^{+0.04}_{-0.04}$ (32^{+6}_{-6}%)	$0.85^{+0.07}_{-0.07}$	1200^{+140}_{-130}	160^{+30}_{-30}
	[f]$145.59^{+0.05}_{-0.04}$	[O I]	$0.85^{+0.11}_{-0.09}$ (46^{+18}_{-15}%)	$0.28^{+0.07}_{-0.04}$	1300^{+300}_{-300}	100^{+90}_{-80}
	[g]$157.78^{+0.01}_{-0.01}$	[C II]	$0.631^{+0.009}_{-0.009}$ (8^{+1}_{-1}%)	$5.24^{+0.13}_{-0.13}$	460^{+40}_{-40}	60^{+10}_{-10}

Table 4.2 (cont'd)

Target	Wavelength (μm)	Line	FWHM (%)[c] (μm)	Surface Brightness (10^{-4} ergs s^{-1}cm^{-2}sr^{-1})	Velocity[a] (km s^{-1})	Shift[b,k] (km s^{-1})
G54.1+0.3	$63.18^{+0.01}_{-0.01}$	[O I]	$0.297^{+0.03}_{-0.03}$	$0.19^{+0.04}_{-0.02}$	...	...
	[d,e]$88.39^{+0.04}_{-0.09}$	[O III]	$0.56^{+0.17}_{-0.09}$	$0.13^{+0.05}_{-0.04}$	...	...
	$122.03^{+0.03}_{-0.02}$	[N II]	$0.44^{+0.04}_{-0.04}$	$0.04^{+0.01}_{-0.01}$	...	330^{+60}_{-60}
	$157.74^{+0.01}_{-0.01}$	[C II]	$0.67^{+0.01}_{-0.01}$ (15^{+1}_{-1}%)	$0.72^{+0.03}_{-0.03}$	640^{+40}_{-40}	...
Tycho # 1 *(G120.1+1.4)*	$157.72^{+0.01}_{-0.01}$	[C II]	$0.62^{+0.01}_{-0.01}$ (5^{+2}_{-2}%)	$0.24^{+0.01}_{-0.01}$	370^{+80}_{-80}	...
3C 58 (#1) *(G130.7+3.1)*	[e]$157.75^{+0.03}_{-0.03}$	[C II]	$0.60^{+0.06}_{-0.05}$	$0.10^{+0.02}_{-0.02}$	...	...
3C 58 (#3)	$157.72^{+0.01}_{-0.01}$	[C II]	$0.58^{+0.02}_{-0.02}$	$0.09^{+0.01}_{-0.01}$	...	...
[j]**3C 58 (#5 Raster 1)**	$157.74^{+0.02}_{-0.02}$	[C II]	$0.67^{+0.04}_{-0.04}$ (14^{+7}_{-7}%)	$0.07^{+0.01}_{-0.01}$	600^{+200}_{-100}	...
[j]**3C 58 (#5 Raster 2)**	$157.74^{+0.01}_{-0.01}$	[C II]	$0.59^{+0.03}_{-0.03}$	$0.07^{+0.01}_{-0.01}$	...	...
Crab Nebula *(G184.6–05.8)*	$51.79^{+0.01}_{-0.01}$	[O III]	$0.55^{+0.03}_{-0.03}$ (109^{+12}_{-12}%)	$3.7^{+0.4}_{-0.3}$	2800^{+200}_{-200}	-160^{+70}_{-70}
[l](blue-shifted)	$51.66^{+0.02}_{-0.02}$	[O III]	$0.32^{+0.05}_{-0.04}$ (22^{+19}_{-15}%)	$2.1^{+0.4}_{-0.4}$	1100^{+500}_{-400}	-900^{+100}_{-100}
[l](red-shifted)	$51.98^{+0.02}_{-0.02}$	[O III]	$0.26^{+0.04}_{-0.03}$	$1.3^{+0.4}_{-0.4}$	...	900^{+100}_{-100}
	$63.13^{+0.01}_{-0.01}$	[O I]	$0.56^{+0.02}_{-0.02}$ (102^{+7}_{-7}%)	$1.51^{+0.09}_{-0.09}$	2300^{+100}_{-100}	-300^{+50}_{-50}
	$88.23^{+0.02}_{-0.02}$	[O III]	$1.01^{+0.07}_{-0.06}$ (255^{+23}_{-22}%)	$4.1^{+0.5}_{-0.5}$	3300^{+200}_{-200}	-430^{+70}_{-70}
[l](blue-shifted)	$88.02^{+0.01}_{-0.01}$	[O III]	$0.39^{+0.03}_{-0.03}$ (38^{+11}_{-11}%)	$1.6^{+0.2}_{-0.1}$	900^{+200}_{-100}	-1120^{+40}_{-50}

Table 4.2 (cont'd)

Target	Wavelength (μm)	Line	FWHM (%)[c] (μm)	Surface Brightness (10^{-4} ergs s^{-1}cm^{-2}sr^{-1})	Velocity[a] (km s^{-1})	Shift[b,k] (km s^{-1})
[l](red-shifted)	$88.57^{+0.01}_{-0.01}$	[O III]	$0.41^{+0.04}_{-0.03}$ (45^{+14}_{-11}%)	$1.4^{+0.2}_{-0.1}$	1000^{+200}_{-200}	730^{+30}_{-40}
	[e]$121.91^{+0.05}_{-0.05}$	[N II]	$1.0^{+0.2}_{-0.2}$ (73^{+32}_{-29}%)	$0.10^{+0.03}_{-0.03}$	2000^{+600}_{-500}	...
	$145.5^{+0.1}_{-0.1}$	[O I]	$1.5^{+0.5}_{-0.3}$ (160^{+80}_{-49}%)	$0.09^{+0.04}_{-0.02}$	2900^{+1100}_{-600}	...
	$157.69^{+0.03}_{-0.03}$	[C II]	$1.09^{+0.07}_{-0.07}$ (87^{+12}_{-11}%)	$0.15^{+0.02}_{-0.02}$	1800^{+200}_{-100}	-90^{+60}_{-60}
IC 443 (#1)	$63.19^{+0.01}_{-0.01}$	[O I]	$0.280^{+0.002}_{-0.002}$	$13.2^{+0.3}_{-0.3}$	...	...
(G189.1+3.0)	[f]$145.55^{+0.01}_{-0.01}$	[O I]	$0.72^{+0.03}_{-0.03}$ (23^{+5}_{-5}%)	$0.62^{+0.05}_{-0.05}$	$900\ ^{+100}_{-100}$	50^{+20}_{-20}
	[g]$157.73^{+0.01}_{-0.01}$	[C II]	$0.67^{+0.02}_{-0.02}$ (14^{+2}_{-2}%)	$2.56^{+0.1}_{-0.09}$	600^{+60}_{-60}	...
IC 443 (#2)	[g]$63.20^{+0.01}_{-0.01}$	[O I]	$0.295^{+0.005}_{-0.005}$ (6^{+1}_{-1}%)	$5.8^{+0.3}_{-0.3}$	500^{+70}_{-70}	90^{+20}_{-20}
(G189.1+3.0)	[e]$121.93^{+0.06}_{-0.07}$	[N II]	$1.2^{+0.3}_{-0.3}$ (111^{+50}_{-43}%)	$0.15^{+0.04}_{-0.04}$	2700^{+800}_{-700}	...
	$145.52^{+0.01}_{-0.01}$	[O I]	$0.66^{+0.02}_{-0.01}$ (13^{+2}_{-2}%)	$0.33^{+0.02}_{-0.02}$	640^{+60}_{-60}	...
	[g]$157.75^{+0.01}_{-0.01}$	[C II]	$0.67^{+0.02}_{-0.02}$ (15^{+4}_{-4}%)	$1.8^{+0.2}_{-0.2}$	640^{+100}_{-90}	....
IC 443 (#3)	$63.18^{+0.01}_{-0.01}$	[O I]	$0.274^{+0.006}_{-0.005}$	$2.89^{+0.09}_{-0.07}$	...	....
(G189.1+3.0)	[e]$122.02^{+0.07}_{-0.06}$	[N II]	$1.1^{+0.3}_{-0.2}$ (94^{+57}_{-36}%)	$0.09^{+0.03}_{-0.02}$	2400^{+1000}_{-600}	300^{+200}_{-200}
	$145.52^{+0.02}_{-0.02}$	[O I]	$0.77^{+0.04}_{-0.04}$ (31^{+6}_{-6}%)	$0.25^{+0.03}_{-0.03}$	1000^{+100}_{-100}	...
	$157.75^{+0.01}_{-0.01}$	[C II]	$0.68^{+0.01}_{-0.01}$ (16^{+2}_{-1}%)	$0.88^{+0.04}_{-0.04}$	670^{+40}_{-40}	...

Table 4.2 (cont'd)

Target	Wavelength (μm)	Line	FWHM (%)[c] (μm)	Surface Brightness (10^{-4} ergs s^{-1}cm^{-2}sr^{-1})	Velocity[a] (km s^{-1})	Shift[b,k] (km s^{-1})
G292.0+1.8	[e]$63.22^{+0.02}_{-0.03}$	[O I]	$0.29^{+0.07}_{-0.06}$	$0.14^{+0.07}_{-0.04}$	...	...
	$88.37^{+0.03}_{-0.02}$	[O III]	$0.17^{+0.05}_{-0.06}$	$0.21^{+0.11}_{-0.08}$	...	...
	[g]$157.73^{+0.01}_{-0.01}$	[C II]	$0.61^{+0.02}_{-0.02}$	$0.16^{+0.01}_{-0.01}$	...	...
G320.4–1.2	[e,g,i]$63.15^{+0.03}_{-0.04}$	[O I]	$0.29^{+0.08}_{-0.06}$	$0.3^{+0.1}_{-0.1}$	...	...
	$88.28^{+0.03}_{-0.03}$	[O III]	$0.66^{+0.06}_{-0.06}$ (137^{+20}_{-20}%)	$1.2^{+0.1}_{-0.1}$	2100^{+200}_{-200}	-240^{+90}_{-90}
	$121.95^{+0.02}_{-0.03}$	[N II]	$0.9^{+0.1}_{-0.1}$ (62^{+22}_{-19}%)	$0.18^{+0.03}_{-0.03}$	1800^{+400}_{-400}	120^{+60}_{-70}
	[g]$157.70^{+0.01}_{-0.01}$	[C II]	$0.629^{+0.006}_{-0.006}$ (7^{+1}_{-1}%)	$1.21^{+0.02}_{-0.02}$	400^{+30}_{-30}	-78^{+9}_{-9}
RCW 103 (# 1)	$63.20^{+0.01}_{-0.01}$	[O I]	$0.32^{+0.01}_{-0.01}$ (17^{+3}_{-3}%)	$1.53^{+0.11}_{-0.07}$	800^{+90}_{-90}	100^{+30}_{-30}
(G332.4–0.4)	$88.30^{+0.02}_{-0.02}$	[O III]	$0.23^{+0.05}_{-0.04}$	$0.7^{+0.3}_{-0.2}$	...	-180^{+60}_{-60}
	$121.87^{+0.02}_{-0.02}$	[N II]	$0.89^{+0.04}_{-0.04}$ (51^{+6}_{-6}%)	$0.9^{+0.1}_{-0.1}$	1600^{+100}_{-100}	...
	[i]$145.49^{+0.04}_{-0.04}$	[O I]	$0.64^{+0.06}_{-0.06}$	$0.25^{+0.05}_{-0.05}$	...	...
	[g]$157.73^{+0.01}_{-0.01}$	[C II]	$0.70^{+0.01}_{-0.01}$ (20^{+1}_{-1}%)	$5.7^{+0.2}_{-0.2}$	750^{+40}_{-40}	...
RCW 103 (# 3)	$51.84^{+0.04}_{-0.03}$	[O III]	$0.27^{+0.08}_{-0.06}$	$1.2^{+1.0}_{-1.0}$	...	...
(G332.4-0.4)	$63.17^{+0.01}_{-0.01}$	[O I]	$0.28^{+0.01}_{-0.01}$	$5.3^{+0.7}_{-0.7}$	...	-80^{+30}_{-30}
	$88.42^{+0.01}_{-0.01}$	[O III]	$0.30^{+0.02}_{-0.02}$	$1.6^{+0.5}_{-0.2}$	...	200^{+30}_{-30}

Table 4.2 (cont'd)

Target	Wavelength (μm)	Line	FWHM (%)[c] (μm)	Surface Brightness (10^{-4} ergs s^{-1}cm^{-2}sr^{-1})	Velocity[a] (km s^{-1})	Shift[b,k] (km s^{-1})
	[e]$121.97^{+0.03}_{-0.03}$	[N II]	$0.98^{+0.11}_{-0.16}$ (68^{+19}_{-28}%)	$0.9^{+0.2}_{-0.2}$	2000^{+300}_{-500}	180^{+70}_{-80}
	[i]$145.44^{+0.03}_{-0.04}$	[O I]	$0.65^{+0.10}_{-0.09}$	$0.35^{+0.06}_{-0.05}$	...	-180^{+70}_{-80}
	$157.72^{+0.01}_{-0.01}$	[C II]	$0.74^{+0.02}_{-0.02}$ (26^{+3}_{-3}%)	$5.6^{+0.4}_{-0.4}$	850^{+70}_{-60}	-50^{+10}_{-10}
E0102.2–7219	[d]$88.29^{+0.05}_{-0.04}$	[O III]	$0.7^{+0.1}_{-0.1}$ (20^{+21}_{-18}%)	$0.16^{+0.04}_{-0.04}$	1300^{+800}_{-600}	-400^{+200}_{-100}
(*J0104.1–7201*)	$157.78^{+0.01}_{-0.01}$	[C II]	$0.60^{+0.03}_{-0.03}$	$0.11^{+0.01}_{-0.01}$	...	-90^{+20}_{-20}
N132D	[e]$63.27^{+0.02}_{-0.02}$	[O I]	$0.43^{+0.05}_{-0.04}$ (54^{+17}_{-16}%)	$0.18^{+0.05}_{-0.03}$	1500^{+300}_{-300}	...
(*J0525.0–6938*)	$157.87^{+0.01}_{-0.01}$	[C II]	$0.61^{+0.01}_{-0.01}$ (4^{+1}_{-1}%)	$0.23^{+0.01}_{-0.01}$	330^{+70}_{-70}	...
[j]**N49** *(J0526.0–6604)*	[e]$88.50^{+0.07}_{-0.09}$	[O III]	$1.1^{+0.6}_{-0.4}$ (90^{+103}_{-68}%)	$0.4^{+0.2}_{-0.1}$	3000^{+2000}_{-1000}	...
N63A	$63.26^{+0.01}_{-0.01}$	[O I]	$0.264^{+0.009}_{-0.009}$	$1.73^{+0.13}_{-0.08}$	...	100^{+20}_{-20}
(*J0535.7–6602*)	$88.45^{+0.01}_{-0.01}$	[O III]	$0.276^{+0.018}_{-0.015}$	$0.63^{+0.09}_{-0.08}$	...	...
	$145.75^{+0.02}_{-0.03}$	[O I]	$0.60^{+0.06}_{-0.06}$	$0.076^{+0.012}_{-0.012}$	...	180^{+50}_{-60}
	$157.94^{+0.01}_{-0.01}$	[C II]	$0.563^{+0.01}_{-0.01}$	$0.42^{+0.02}_{-0.02}$	...	90^{+10}_{-10}
SN1987A	[e]$51.86^{+0.02}_{-0.02}$	[O III]	$0.26^{+0.04}_{-0.04}$	$0.7^{+0.2}_{-0.2}$	...	...
(J0535–6916)	$88.48^{+0.01}_{-0.01}$	[O III]	$0.29^{+0.01}_{-0.01}$	$1.5^{+0.2}_{-0.2}$	...	160^{+10}_{-10}
	$157.88^{+0.01}_{-0.01}$	[C II]	$0.62^{+0.02}_{-0.02}$	$0.20^{+0.01}_{-0.01}$	...	...

Table 4.2 (cont'd)

Target	Wavelength (μm)	Line	FWHM (%)[c] (μm)	Surface Brightness (10^{-4} ergs s^{-1}cm^{-2}sr^{-1})	Velocity[a] (km s^{-1})	Shift[b,k] (km s^{-1})
[j]**SN1987A (L02)**	$51.87^{+0.01}_{-0.01}$	[O III]	$0.30^{+0.03}_{-0.03}$	$0.7^{+0.1}_{-0.1}$	...	...
	$157.87^{+0.01}_{-0.01}$	[C II]	$0.60^{+0.02}_{-0.02}$	$0.19^{+0.01}_{-0.01}$	...	...
0540–69.3	[e]$51.64^{+0.03}_{-0.03}$	[O III]	$0.59^{+0.12}_{-0.09}$ (91^{+38}_{-29}%)	$1.8^{+0.6}_{-0.5}$	2900^{+800}_{-600}	-1300^{+200}_{-200}
(J0535.7–6602)	$63.22^{+0.01}_{-0.01}$	[O I]	$0.26^{+0.02}_{-0.02}$	$0.18^{+0.02}_{-0.02}$	...	-90^{+60}_{-50}
	[e]$88.47^{+0.02}_{-0.02}$	[O III]	$0.32^{+0.05}_{-0.05}$	$0.4^{+0.2}_{-0.1}$	...	...
	$157.88^{+0.01}_{-0.01}$	[C II]	$0.64^{+0.03}_{-0.02}$ (6^{+2}_{-2}%)	$0.47^{+0.03}_{-0.03}$	400^{+100}_{-100}	...

[a]Estimated velocity dispersion after accounting for instrumental resolution.

[b]Doppler shift from the line centroid.

[c]Percent broader than instrument resolution.

[d]Values are estimated from detector LW1.

[e]Less than 5 σ detection.

[f]No line-broadening detected in adjacent subdetector.

[g]High reduced chi-squared value ($\gtrsim 2$).

[h]Low reduced chi-squared value ($\lesssim 0.1$).

[i]Line not detected in adjacent subdetector.

[j]L02 mode observation.

[k]For remnants in the SMC or LMC, the Doppler-shift due to the motion of the galaxy has been subtracted.

[l]The best–fit results for two–Gaussian + linear component model fits to each of the [O III] 52 and 88 μm lines are shown.

··· Value is approximately zero.

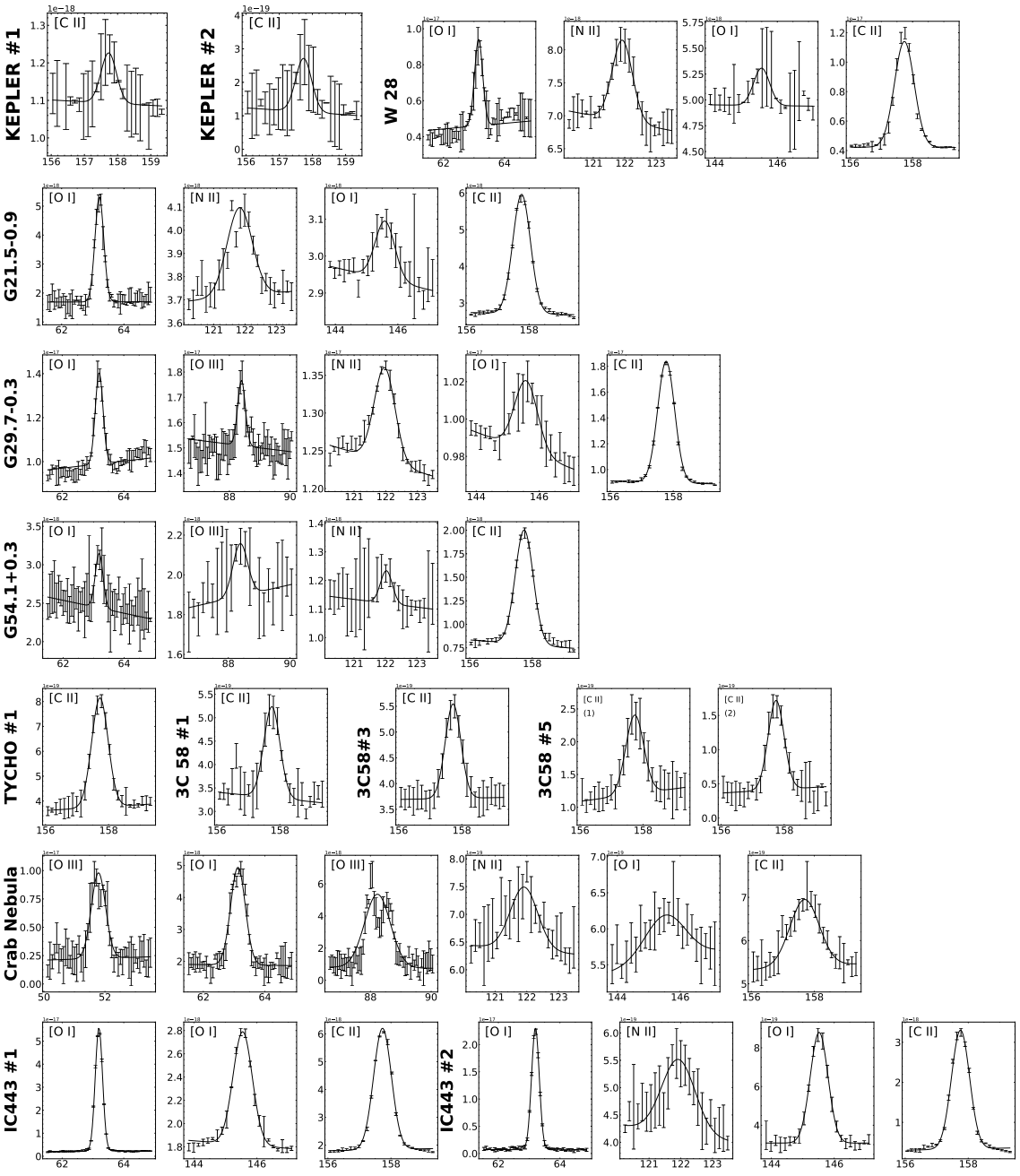

Figure 4.25: FIR Lines of SNRs. The best–fit Gaussian + linear model is overlaid. The y-axis is in units of flux density (erg s^{-1} cm^{-2} sr^{-1}) and x-axis in units of wavelength (μm).

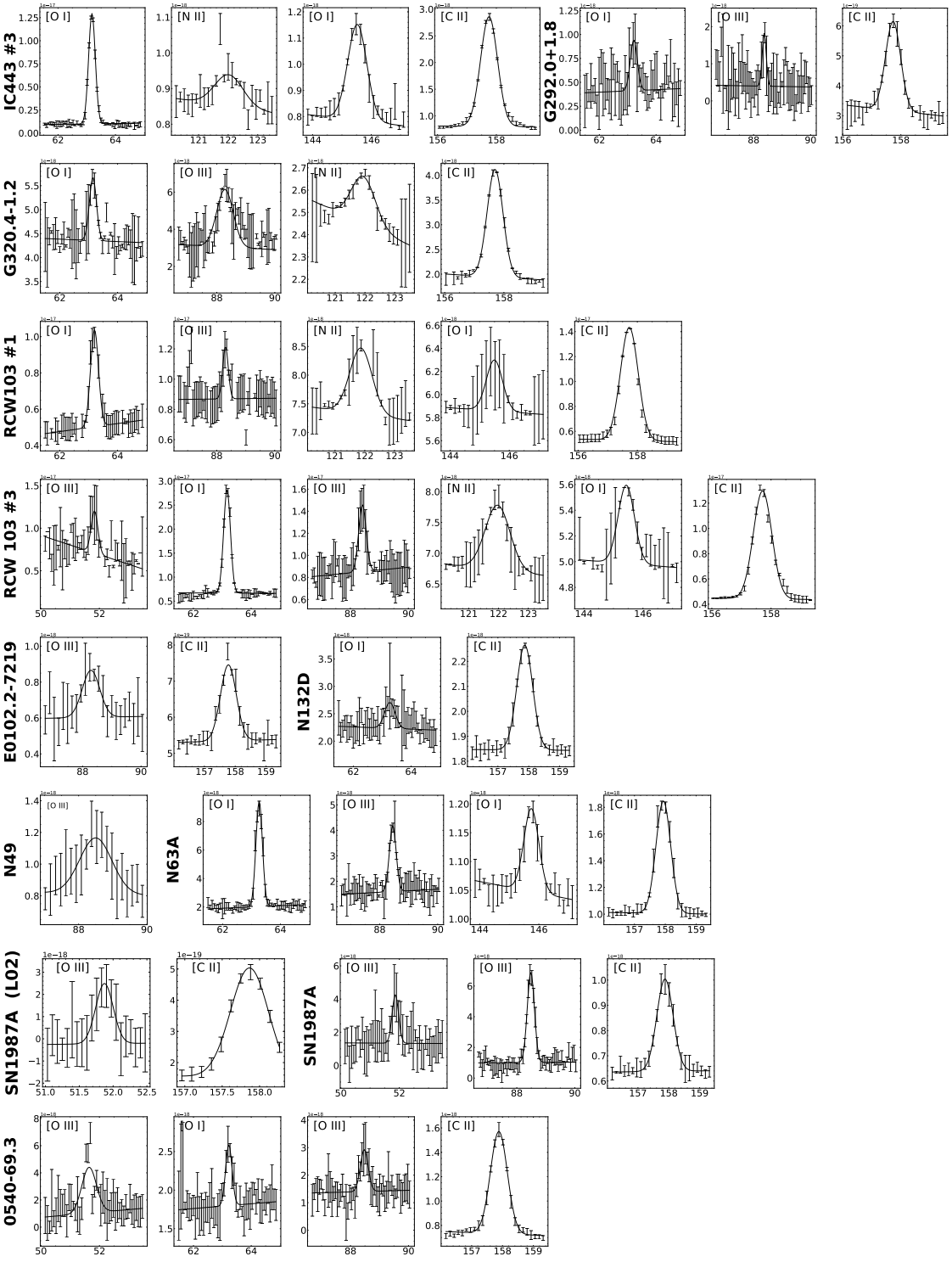

Figure 4.25: FIR Lines of SNRs (continued)

Table 4.3. Observed Spectral Lines from ISO LWS Spectra of HII Regions and PN NGC 6720

Target	Wavelength (μm)	Line	FWHM (%)[c] (μm)	Surface Brightness (10^{-4} ergs s^{-1}cm^{-2}sr^{-1})
W51	$51.82^{+0.01}_{-0.01}$	[O III]	$0.283^{+0.004}_{-0.004}$	289^{+8}_{-8}
	$63.17^{+0.01}_{-0.01}$	[O I]	$0.283^{+0.009}_{-0.008}$	41^{+2}_{-2}
	$88.39^{+0.01}_{-0.01}$	[O III]	$0.287^{+0.005}_{-0.005}$	124^{+4}_{-4}
	$145.54^{+0.01}_{-0.01}$	[O I]	$0.56^{+0.03}_{-0.03}$	$4.9^{+0.5}_{-0.4}$
	$157.74^{+0.01}_{-0.01}$	[C II]	$0.58^{+0.03}_{-0.03}$	12^{+1}_{-1}
G159 (Center) *(G159.6-18.5)*	$157.76^{+0.01}_{-0.01}$	[C II]	$0.62^{+0.01}_{-0.01}$	$0.37^{+0.02}_{-0.02}$
G159 (Rim)	$157.76^{+0.01}_{-0.01}$	[C II]	$0.57^{+0.01}_{-0.01}$	$0.49^{+0.02}_{-0.02}$
NGC6334 (V)	$51.81^{+0.03}_{-0.03}$	[O III]	$0.38^{+0.09}_{-0.08}$	12^{+4}_{-4}
	$63.16^{+0.01}_{-0.01}$	[O I]	$0.25^{+0.02}_{-0.02}$	13^{+2}_{-2}
	$88.38^{+0.02}_{-0.02}$	[O III]	$0.34^{+0.05}_{-0.05}$	9^{+2}_{-2}
	$145.54^{+0.01}_{-0.01}$	[O I]	$0.54^{+0.01}_{-0.01}$	$2.21^{+0.08}_{-0.08}$
	$157.70^{+0.01}_{-0.01}$	[C II]	$0.62^{+0.03}_{-0.03}$	10^{+1}_{-1}
NGC6334 (CP)	$51.83^{+0.01}_{-0.01}$	[O III]	$0.28^{+0.03}_{-0.03}$	7^{+1}_{-1}
	$57.37^{+0.01}_{-0.01}$	[N III]	$0.30^{+0.02}_{-0.02}$	$4.4^{+0.5}_{-0.5}$
	$63.19^{+0.01}_{-0.01}$	[O I]	$0.28^{+0.003}_{-0.003}$	$39.0^{+0.7}_{-0.7}$
	$88.41^{+0.01}_{-0.01}$	[O III]	$0.28^{+0.01}_{-0.01}$	$4.4^{+0.5}_{-0.5}$
	$121.98^{+0.02}_{-0.02}$	[N II]	$0.65^{+0.03}_{-0.02}$	$4.4^{+0.3}_{-0.3}$
	$145.51^{+0.01}_{-0.01}$	[O I]	$0.613^{+0.008}_{-0.008}$	$3.19^{+0.06}_{-0.06}$
	$157.72^{+0.01}_{-0.01}$	[C II]	$0.631^{+0.007}_{-0.007}$	$22.2^{+0.7}_{-0.7}$
NGC6720	$51.84^{+0.01}_{-0.01}$	[O III]	$0.262^{+0.006}_{-0.006}$	$20.3^{+0.8}_{-0.5}$
	$57.34^{+0.01}_{-0.01}$	[N III]	$0.277^{+0.006}_{-0.007}$	$6.4^{+0.3}_{-0.3}$
	$63.19^{+0.01}_{-0.01}$	[O I]	$0.276^{+0.004}_{-0.004}$	$4.4^{+0.1}_{-0.1}$
	$88.38^{+0.01}_{-0.01}$	[O III]	$0.283^{+0.005}_{-0.005}$	$14.8^{+0.4}_{-0.4}$
	$88.41^{+0.01}_{-0.01}$	[O III]	$0.62^{+0.01}_{-0.01}$	$15.1^{+0.5}_{-0.5}$
	$121.96^{+0.01}_{-0.01}$	[N II]	$0.63^{+0.02}_{-0.02}$	$0.33^{+0.02}_{-0.02}$
	$145.54^{+0.01}_{-0.01}$	[O I]	$0.68^{+0.04}_{-0.04}$	$0.17^{+0.02}_{-0.02}$
	$157.76^{+0.01}_{-0.01}$	[C II]	$0.59^{+0.02}_{-0.02}$	$0.60^{+0.03}_{-0.02}$

Note. — Notation the same as in Table 4.2

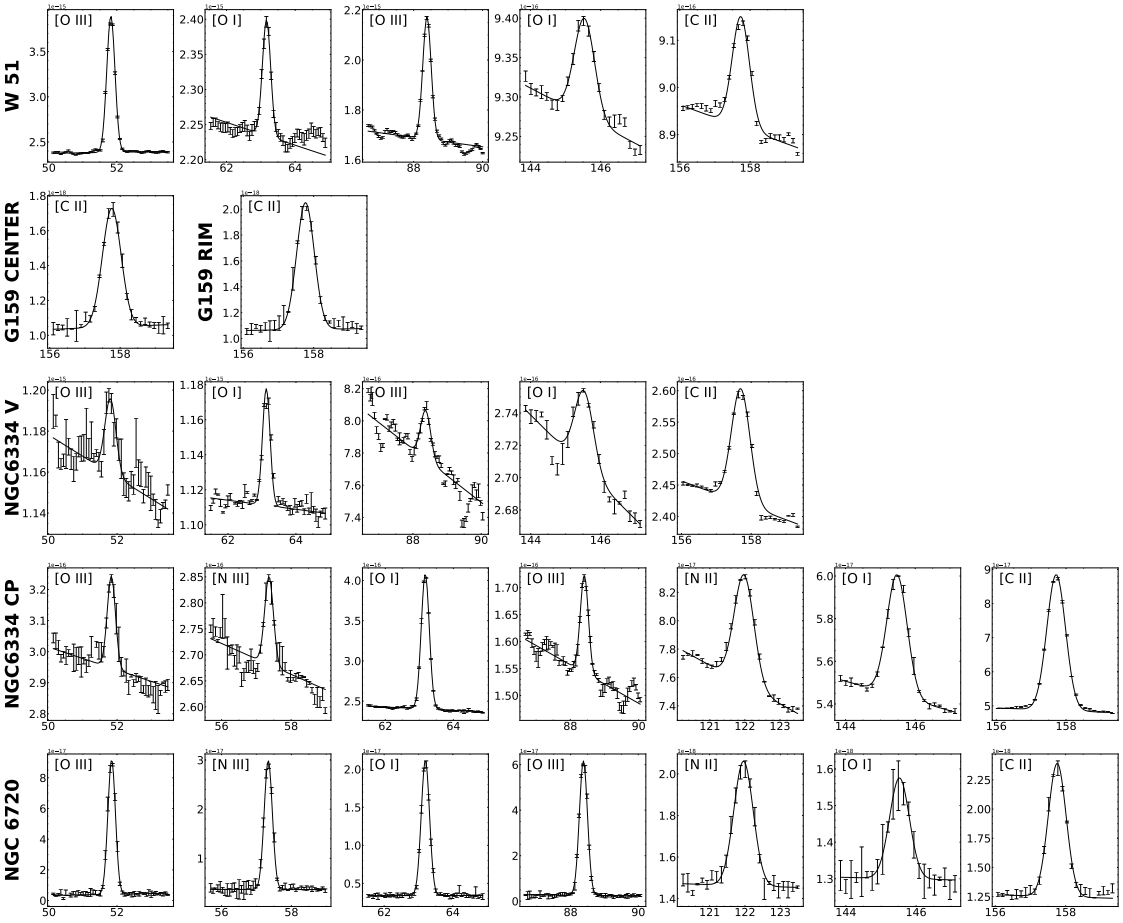

Figure 4.26: FIR Lines of HII Regions. Presentation is the same as Figure 4.25.

Table 4.4. Kes 79 Raster Map 63 μm [O I] Observations

Raster	R.A. (J2000)	Decl. (J2000)	FWHM (%)[c] (μm)	Surface Brightness (10^{-4} ergs s^{-1}cm^{-2}sr^{-1})	Velocity[a] km s^{-1}	Shift[b] (km s^{-1})
1	$18^{h}52^{m}42\overset{s}{.}33$	$+00°39'46\overset{''}{.}89$	$0.27^{+0.01}_{-0.01}$	$0.68^{+0.04}_{-0.04}$	...	...
2	$18^{h}52^{m}45\overset{s}{.}25$	$+00°40'11\overset{''}{.}13$	$0.29^{+0.01}_{-0.01}$	$0.69^{+0.05}_{-0.05}$	...	...
3	$18^{h}52^{m}48\overset{s}{.}17$	$+00°40'35\overset{''}{.}37$	$0.291^{+0.01}_{-0.01}$	$0.65^{+0.04}_{-0.04}$	...	...
4	$18^{h}52^{m}51\overset{s}{.}08$	$+00°40'59\overset{''}{.}62$	$0.29^{+0.02}_{-0.01}$	$0.59^{+0.06}_{-0.06}$	...	...
5	$18^{h}52^{m}54\overset{s}{.}00$	$+00°41'23\overset{''}{.}86$	$0.28^{+0.01}_{-0.01}$	$0.52^{+0.02}_{-0.02}$	...	100^{+10}_{-10}
6	$18^{h}52^{m}56\overset{s}{.}92$	$+00°41'48\overset{''}{.}09$	$0.28^{+0.01}_{-0.01}$	$0.62^{+0.03}_{-0.03}$	...	80^{+20}_{-20}
7	$18^{h}52^{m}59\overset{s}{.}83$	$+00°42'12\overset{''}{.}34$	$0.28^{+0.01}_{-0.01}$	$0.63^{+0.02}_{-0.02}$	...	70^{+10}_{-10}
8	$18^{h}53^{m}02\overset{s}{.}75$	$+00°42'36\overset{''}{.}58$	$0.31^{+0.01}_{-0.01}$	$0.71^{+0.03}_{-0.03}$	...	...
9	$18^{h}53^{m}05\overset{s}{.}66$	$+00°43'00\overset{''}{.}82$	$0.28^{+0.01}_{-0.01}$	$0.68^{+0.02}_{-0.02}$	...	60^{+10}_{-10}

Note. — Notation the same as in Table 4.2

Table 4.5. CTB 109 Raster Map 63 μm [O I] Observations

Raster	R.A. (J2000)	Decl. (J2000)	FWHM (%)[c] (μm)	Surface Brightness (10^{-4} ergs s^{-1}cm^{-2}sr^{-1})	Velocity[a] (km s^{-1})	Shift[b] (km s^{-1})
1	$22^h59^m29\overset{s}{.}61$	$+58°50'11\overset{''}{.}35$	$0.28^{+0.02}_{-0.03}$	$0.20^{+0.03}_{-0.04}$	...	...
2	$22^h59^m46\overset{s}{.}21$	$+58°52'16\overset{''}{.}99$	$0.29^{+0.01}_{-0.01}$	$0.26^{+0.02}_{-0.02}$	...	-50^{+10}_{-10}
3	$23^h00^m02\overset{s}{.}87$	$+58°54'22\overset{''}{.}51$	$0.39^{+0.06}_{-0.05}$ (38^{+21}_{-18}%)	$0.22^{+0.05}_{-0.05}$	1300^{+400}_{-400}	-150^{+100}_{-90}
4	$23^h00^m19\overset{s}{.}55$	$+58°56'27\overset{''}{.}89$	$0.27^{+0.03}_{-0.03}$	$0.14^{+0.02}_{-0.02}$	...	...
5	$23^h00^m36\overset{s}{.}26$	$+58°58'33\overset{''}{.}14$	$0.24^{+0.03}_{-0.03}$	$0.09^{+0.02}_{-0.02}$	...	...
6	$23^h00^m53\overset{s}{.}01$	$+59°00'38\overset{''}{.}25$	$0.27^{+0.06}_{-0.07}$	$0.12^{+0.04}_{-0.05}$	...	...
7	$23^h01^m09\overset{s}{.}79$	$+59°02'43\overset{''}{.}22$	$0.24^{+0.08}_{-0.05}$	$0.12^{+0.08}_{-0.07}$	...	-200^{+200}_{-100}
8	$23^h01^m26\overset{s}{.}61$	$+59°04'48\overset{''}{.}07$	$0.35^{+0.03}_{-0.04}$ (24^{+11}_{-14}%)	$0.21^{+0.04}_{-0.04}$	1000^{+300}_{-300}	...
9	$23^h01^m43\overset{s}{.}46$	$+59°06'52\overset{''}{.}77$	$0.48^{+0.09}_{-0.08}$ (70^{+32}_{-28}%)	$0.17^{+0.06}_{-0.06}$	1800^{+600}_{-500}	...
10	$23^h02^m00\overset{s}{.}35$	$+59°08'57\overset{''}{.}34$	$0.37^{+0.13}_{-0.07}$ (31^{+46}_{-25}%)	$0.17^{+0.08}_{-0.07}$	1200^{+900}_{-500}	-300^{+100}_{-100}
11	$23^h02^m17\overset{s}{.}26$	$+59°11'01\overset{''}{.}77$	$0.28^{+0.04}_{-0.04}$	$0.12^{+0.04}_{-0.04}$	...	...

Note. — Notation the same as in Table 4.2

Table 4.6. IC 443 Raster Map Observations

Raster	R.A. (J2000)	Decl. (J2000)	FWHM (%)[c] (μm)	Surface Brightness (10^{-4} ergs s^{-1}cm^{-2}sr^{-1})	Velocity[a] (km s^{-1})	Shift[b] (km s^{-1})
63 μm [O I]						
1	$06^h16^m58.^s52$	$+22°13'45.''22$	$0.27^{+0.02}_{-0.02}$	$0.35^{+0.07}_{-0.07}$	...	...
2	$06^h17^m00.^s78$	$+22°16'42.''47$	$0.28^{+0.02}_{-0.02}$	$0.62^{+0.06}_{-0.06}$	...	120^{+40}_{-40}
3	$06^h17^m03.^s05$	$+22°19'39.''71$	$0.30^{+0.01}_{-0.01}$	$1.97^{+0.05}_{-0.05}$	...	...
4	$06^h17^m05.^s32$	$+22°22'36.''95$	$0.31^{+0.01}_{-0.01}$	$0.77^{+0.04}_{-0.04}$	...	...
5	$06^h17^m07.^s59$	$+22°25'34.''19$	$0.26^{+0.01}_{-0.01}$	$9.7^{+0.4}_{-0.4}$	...	60^{+10}_{-10}
6	$06^h17^m09.^s86$	$+22°28'31.''43$	$0.32^{+0.02}_{-0.01}$	$0.81^{+0.06}_{-0.06}$	...	...
7	$06^h17^m12.^s14$	$+22°31'28.''66$	$0.29^{+0.02}_{-0.02}$	$0.20^{+0.08}_{-0.08}$	...	290^{+20}_{-20}
8	$06^h17^m14.^s42$	$+22°34'25.''89$	$0.22^{+0.03}_{-0.03}$	$0.48^{+0.08}_{-0.09}$	...	160^{+80}_{-70}
9	$06^h17^m16.^s69$	$+22°37'23.''12$	$0.30^{+0.01}_{-0.01}$	$0.76^{+0.05}_{-0.05}$	...	200^{+10}_{-10}
145 μm [O I]						
1	$06^h16^m58.^s52$	$+22°13'45.''22$	$0.5^{+0.3}_{-0.3}$	$0.013^{+0.009}_{-0.009}$	...	...
2	$06^h17^m00.^s78$	$+22°16'42.''47$	$0.57^{+0.05}_{-0.05}$	$0.03^{+0.01}_{-0.01}$	...	160^{+50}_{-40}
3	$06^h17^m03.^s05$	$+22°19'39.''71$	$0.61^{+0.04}_{-0.04}$	$0.08^{+0.01}_{-0.01}$	...	...
4	$06^h17^m05.^s32$	$+22°22'36.''95$	$0.54^{+0.06}_{-0.05}$	$0.05^{+0.01}_{-0.01}$	...	...
5	$06^h17^m07.^s59$	$+22°25'34.''19$	$0.58^{+0.01}_{-0.01}$	$0.32^{+0.01}_{-0.01}$	...	...
6	$06^h17^m09.^s86$	$+22°28'31.''43$	$0.84^{+0.07}_{-0.06}$ (43^{+12}_{-10}%)	$0.05^{+0.01}_{-0.01}$	1200^{+200}_{-200}	-100^{+40}_{-40}
7	$06^h17^m12.^s14$	$+22°31'28.''66$	$0.48^{+0.09}_{-0.07}$	$0.03^{+0.01}_{-0.01}$	...	...
8	$06^h17^m14.^s42$	$+22°34'25.''89$	$0.46^{+0.05}_{-0.05}$	$0.04^{+0.01}_{-0.01}$	...	160^{+70}_{-60}
9	$06^h17^m16.^s69$	$+22°37'23.''12$	$0.62^{+0.05}_{-0.05}$	$0.05^{+0.01}_{-0.01}$	...	...
158 μm [C II]						
1	$06^h16^m58.^s52$	$+22°13'45.''22$	$0.58^{+0.02}_{-0.02}$	$0.22^{+0.02}_{-0.02}$	...	...
2	$06^h17^m00.^s78$	$+22°16'42.''47$	$0.59^{+0.04}_{-0.04}$	$0.36^{+0.04}_{-0.04}$	...	...
3	$06^h17^m03.^s05$	$+22°19'39.''71$	$0.60^{+0.02}_{-0.02}$	$0.77^{+0.06}_{-0.06}$	...	...
4	$06^h17^m05.^s32$	$+22°22'36.''95$	$0.54^{+0.04}_{-0.04}$	$0.49^{+0.06}_{-0.05}$	...	...
5	$06^h17^m07.^s59$	$+22°25'34.''19$	$0.60^{+0.02}_{-0.02}$	$1.37^{+0.04}_{-0.04}$	...	...
6	$06^h17^m09.^s86$	$+22°28'31.''43$	$0.62^{+0.02}_{-0.02}$	$0.41^{+0.02}_{-0.02}$	...	...
7	$06^h17^m12.^s14$	$+22°31'28.''66$	$0.58^{+0.04}_{-0.03}$	$0.27^{+0.03}_{-0.03}$	...	70^{+30}_{-20}
8	$06^h17^m14.^s42$	$+22°34'25.''89$	$0.63^{+0.02}_{-0.02}$	$0.39^{+0.04}_{-0.04}$	...	70^{+30}_{-30}
9	$06^h17^m16.^s69$	$+22°37'23.''12$	$0.4^{+0.1}_{-0.2}$	$0.3^{+0.2}_{-0.2}$	...	...

Note. — Notation the same as in Table 4.2

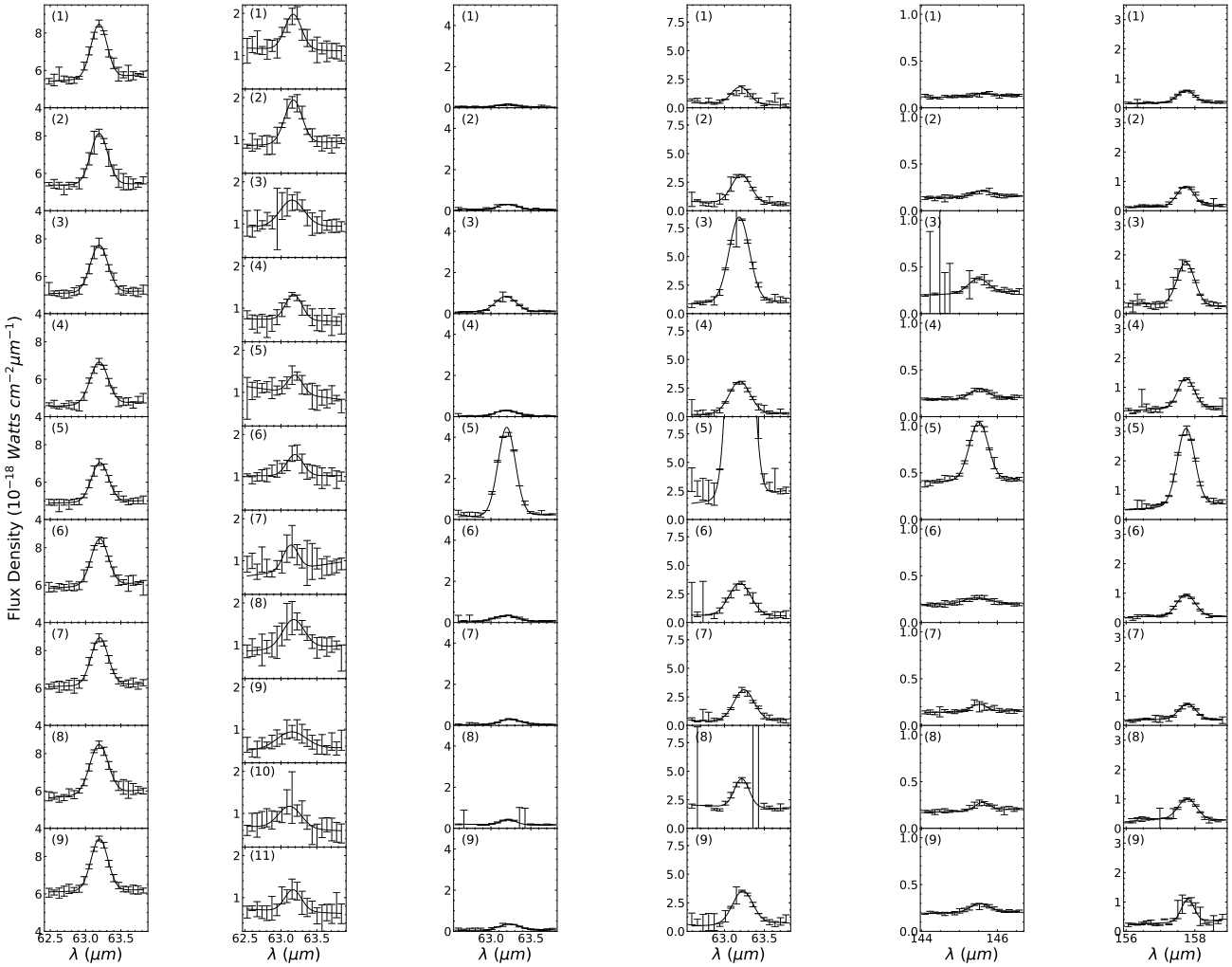

(a) Kes 79: 63 µm (b) CTB 109: 63 µm (c) IC 443: 63 µm (d) Same as (c) Zoomed (e) IC 443: 145 µm (f) IC 443: 158 µm

Figure 4.27: FIR Lines of LWS Observations with multiple raster pointings.

Table 4.7: Spectral Resolution of ISO LWS

Detector	Line	Detector FWHM[a]		NGC 6720 FWHM	
		(μm)	(km s^{-1})	(μm)	(km s^{-1})
SW2 (49.5–64 μm)	52 μm ([O III])	0.283±0.009	1640±50	0.262±0.006	1510±40
SW3 (57–70 μm)	57 μm ([N III])	0.283±0.009	1480±50	0.277±0.007	1450±40
SW3	63 μm ([O I])	0.283±0.009	1400±40	0.283±0.003	1400±20
SW5 (76–93 μm)	88 μm ([O III])	0.283±0.009	1340±40	0.283±0.005	1340±20
LW1 (84–110 μm)	88 μm ([O III])	0.584±0.015	1980±50	0.618±0.013	2100±40
LW2 (103–128 μm)	122 μm ([N II])	0.584±0.015	1440±40	0.634±0.024	1560±60
LW4 (142–171 μm)	145 μm ([O I])	0.584±0.015	1200±30	0.680±0.044	1400±90
LW4	158 μm ([C II])	0.584±0.015	1100±30	0.599±0.016	1140±30

[a]ISO LWS Handbook (Gry et al., 2003)

Table 4.8. Properties of Young SNRs with Broad FIR Lines

SNR	Distance (kpc)	Age (yr)	M_{dust} Herschel ($M_\odot$)	Progenitor Mass ($M_\odot$)	Broad Lines[a] (μm)	Measured[a] FWHM(km s^{-1})	Group	52/88 μm[a]	63/145 μm[a]
G21.5–0.9	4.8 [1]	<1000 [2,3]	0.29 [4]	–	63,122,145	900–1800	A	–	11
G29.7–0.3	5.1–10.6 [5,6]	723 [7]	0.51 [4]	8–12 [8]	122,145	1200–1300	A	–	1.3
G54.1+0.3	6.2 [16]	1800-2400 [17]	0.08–0.9 [18]	15–20 [19]	158	640	C	–	–
Crab Nebula	2 [9]	966	0.016–0.6 [10-13]	8–10 [14]	51,63,88,122,145,158	1800-3300	A	1.4, 1.0[b]	17
G320.4–1.2	5.2 [15]	1700 [15]	[e]0.009	–	88,122	1800-2100	A	–	–
RCW 103	3.1 [20]	2000 [21]	0.18 [22], 1.1 [23]	18–20 [24]	63,122	800-2000	C	–	6.1, 15[c]
E0102.2–7219	61	2050 [25]	[e]0.014[26]	25 – 40 [27,28,39]	88	1300	C	–	–
N132D	50	2500 [29]	[d]0.013 [30]	15 ± 5 [31]	63	1500	B	–	–
N49	50	4800 [32]	$\gtrsim$ 0.1 [33]	13 – 17 [34]	88	3000	C	–	–
0540-69.3	50	800 – 1100 [35]	[d,e]1 – 3×10^{-3} [36,37]	20 – 25 [38]	52	2900	C	4.5	–

[a]This work (ISO LWS).

[b]Blue, red-shifted line

[c]Center, rim

[d]AKARI estimate

[e]Spitzer estimate

* Group A: Line flux and line broadening are both significant to $\geq 5\sigma$; Group B: Significance of broad line emission is $> 5\sigma$, line broadening significance is $< 5\sigma$; Group C: Significance of broad line flux $< 5\sigma$.

Note. — 1. Tian & Leahy (2008) 2. Guest et al. (2019) 3. Bietenholz & Bartel (2008) 4. Chawner et al. (2019) 5. Leahy & Tian (2008) 6. Su et al. (2009) 7. Gotthelf et al. (2000) 8. Temim et al. (2019) 9. Trimble (1968) 10. De Looze et al. (2019) 11. Gomez et al. (2012) 12. Temim & Dwek (2013) 13. Owen & Barlow (2015) 14. Smith (2013) 15. Gaensler et al. (1999) 16. Leahy et al. (2008) 17. Bocchino et al. (2010) 18. Rho et al. (2018) 19. Gelfand et al. (2015) 20. Reynoso et al. (2004) 21. Carter et al. (1997) 22. Pinheiro Gonçalves et al. (2011) 23. Andersen et al. (2011) 24. Frank et al. (2015) 25. Finkelstein et al. (2006) 26. Rho et al. (2009) 27. Blair et al. (2000) 28. Flanagan et al. (2004) 29. Law et al. (2020) 30. Seok et al. (2008) 31. Sharda et al. (2020) 32. Park et al. (2012) 33. Otsuka et al. (2010) 34. Zhou et al. (2019) 35. Reynolds (1985) 36. Williams et al. (2008) 37. Lundqvist et al. (2020) 38. (Lundqvist et al., 2011) 39. Alan et al. (2019)

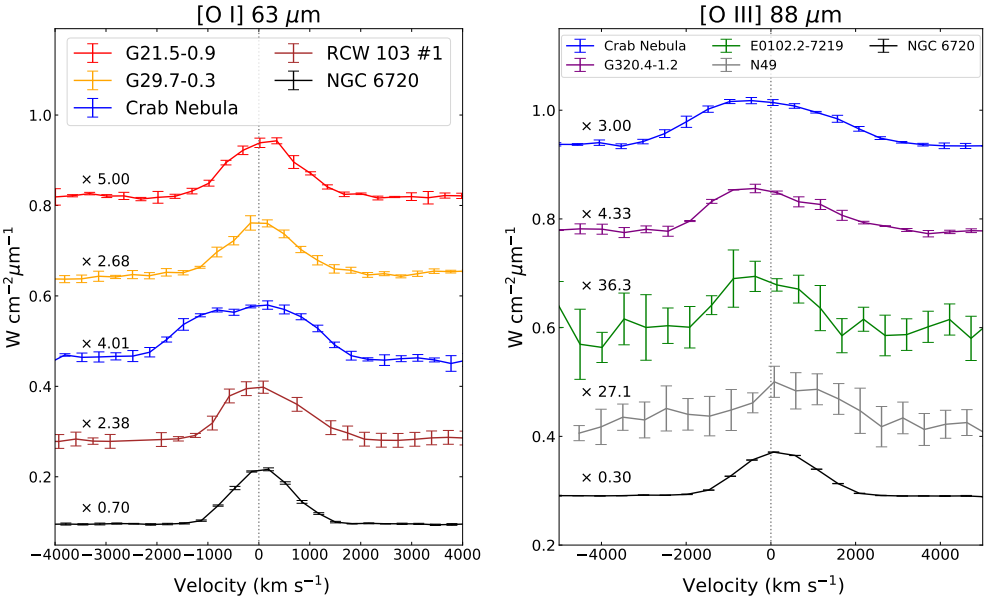

Figure 4.28: ISO LWS velocity profiles of apparently broad 63 μm [O I] and 88 μm [O III] SNR emission lines. The profiles are scaled by the value listed above each line, and shifted for comparison. The solid black line shows the profile of planetary nebula NGC 6720, which represents the velocity resolution of the detector.

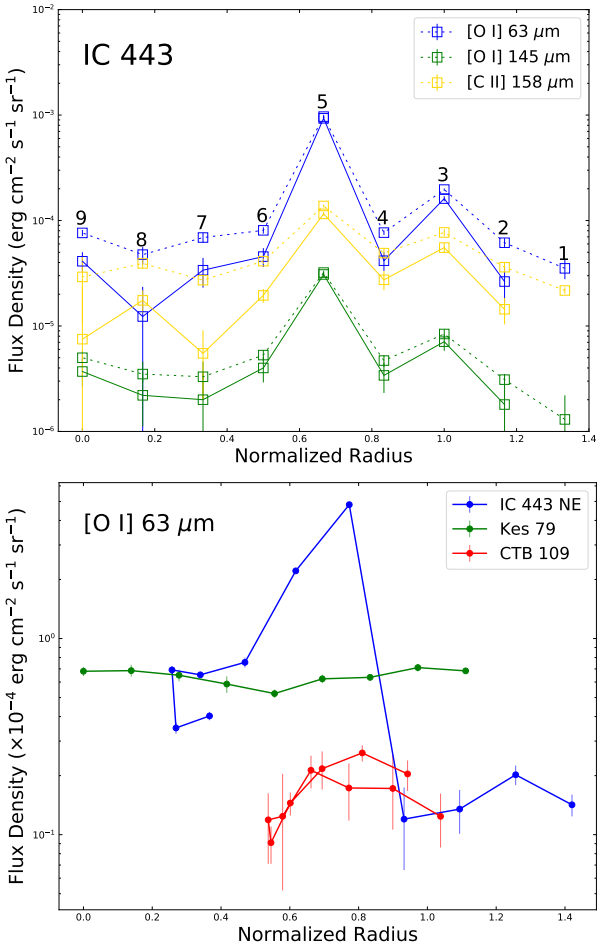

Figure 4.29: Upper: Distribution of [O I] and [C II] line intensity in the southern region of IC 443 (see Figure 4.12) as a function of distance from the center of the SNR. The total flux density in each region is represented by dashed lines, while solid lines indicate the background–subtracted values. The emission peaks at the double shell (position 5 at r=0.7 and 3 at r=1.0). Lower: Total [O I] 63 μm line intensity vs. radius for raster observations of Kes 79, CTB 109, and the northeast region of IC 443 from Rho et al. (2001) are compared with those of the southern region of IC 443 from the upper panel.

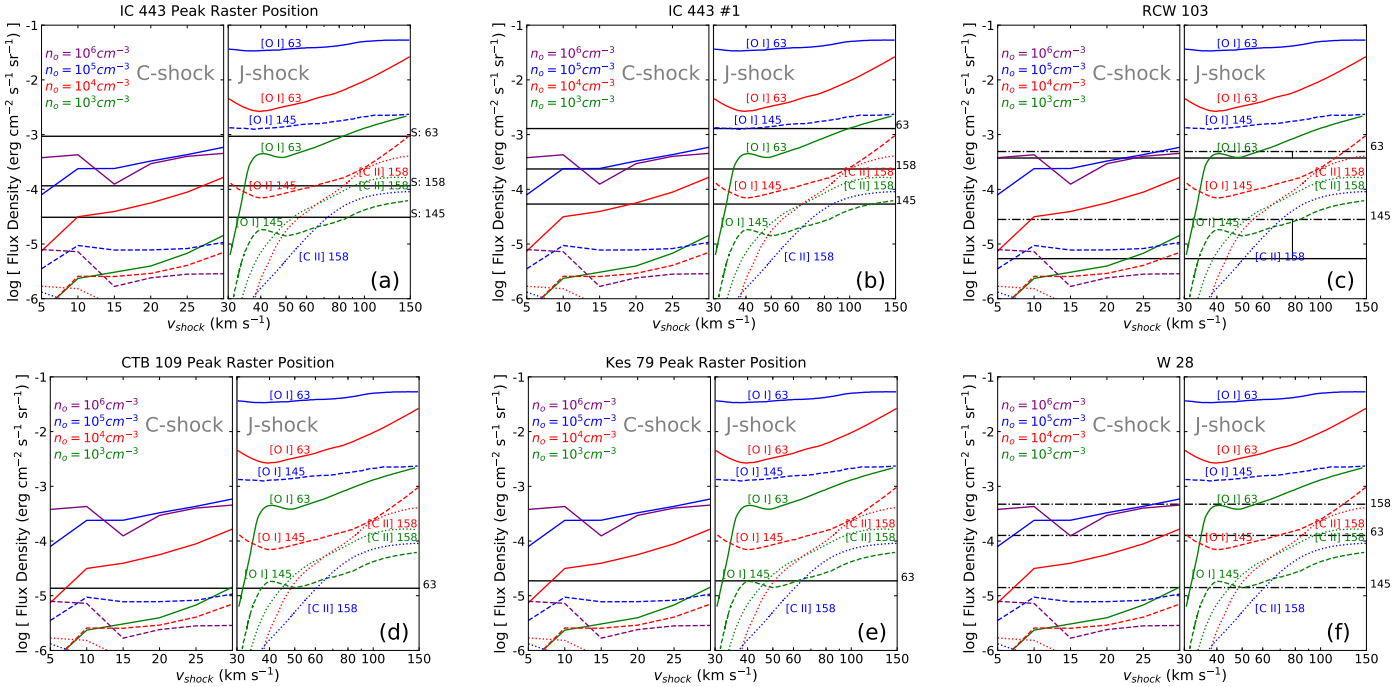

Figure 4.30: In each panel, the predicted [O I] 63 μm, [O I] 145 μm, [C II] 158 μm line brightness values for a slow C–shock (left side) and fast J–shock (right side) interacting with a molecular cloud. The C–shock line intensities were calculated using the Paris–Durham shock code, while the J–shock intensities are reproduced from Figure 7 of Hollenbach & McKee (1989). The observed background–subtracted line brightness values from ISO LWS observations of W 28, IC 443, Kes 79, CTB 109, and RCW 103 are overlaid as solid black horizontal lines. In the W 28 and RCW 103 panels, the total flux density and background–subtracted values are shown as dashed-dotted and solid lines, respectively. The W 28 observation did not include a background measurement.

Table 4.9: Shock Conditions in SNRs Interacting with Molecular Clouds

SNR	L^* ($L_\odot$)	J–shock (n_o, v_s) (cm^{-3}, km s^{-1})	C–shock (n_o, v_s) (cm^{-3}, km s^{-1})	Pressure (p_{ram}, p_{th}) (dyne cm^{-2})
W 28	2	10^3, 30 – 40	$10^4 - 10^6$, **$\sim$ 25**	5×10^{-8}, 10^{-9}
IC 443 #1	10	10^3, **$\sim$ 100**	$10^5 - 10^6$, $\sim$ 30	10^{-7}, 10^{-9}
IC 443 #2	5	10^3, **$\sim$ 60**	$10^5 - 10^6$, $\sim$ 15 or $\sim$ 30	—
IC 443 #3	2	10^3, **30 – 40**	$10^5 - 10^6$, 10 – 20	—
IC 443 Raster (5)	8	10^3, **$\sim$ 80**	$10^5 - 10^6$, $\sim$10 or $\sim$30	—
RCW 103	15	10^3, 30 – 50	$10^5 - 10^6$, $\sim$10 or $\sim$30	10^{-7}, 10^{-7}

*Luminosity values within the ISO LWS beam. Thermal pressure calculated using values from Rho & Borkowski (2002), Troja et al. (2006), and Frank et al. (2015) for W 28, IC 443, and RCW 103, respectively. The most favorable model is marked in bold.

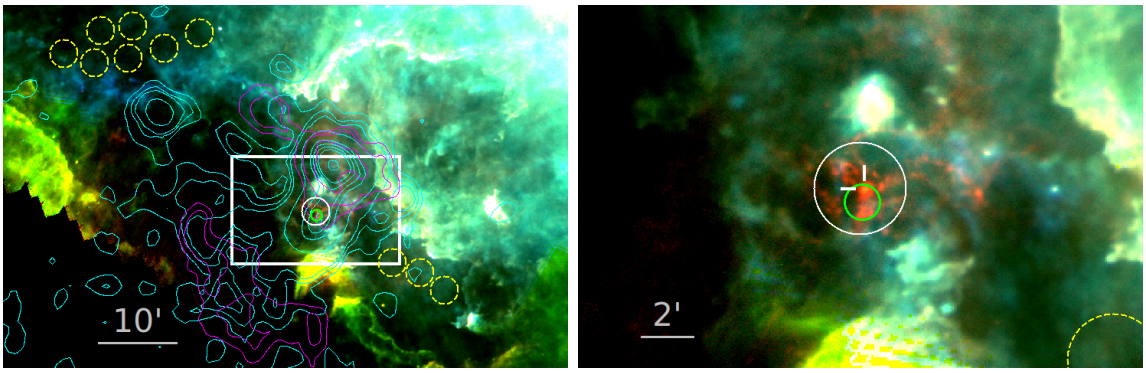

Figure 4.31: Herschel 3-color image (red: 70 μm, green: 160 μm, blue: 250 μm) with the ISO LWS beam shown as a green circle (0.67′ diameter), while the solid white and dashed-yellow circles (1.7′ diameter) shows the Herschel photometric target and background regions, respectively. Contours are the same as in Figure 4.14. Left: Zoomed-out view showing the overall extent of SNR G320.4–1.2. The white box shows the field of view of the panel on the right. Right: Zoomed-in with contours removed to highlight the bright (in red) filamentary 70 μm emission (from IRAS 15099) near the center of the SNR. The white markers indicate the position of the compact source (IRS1).

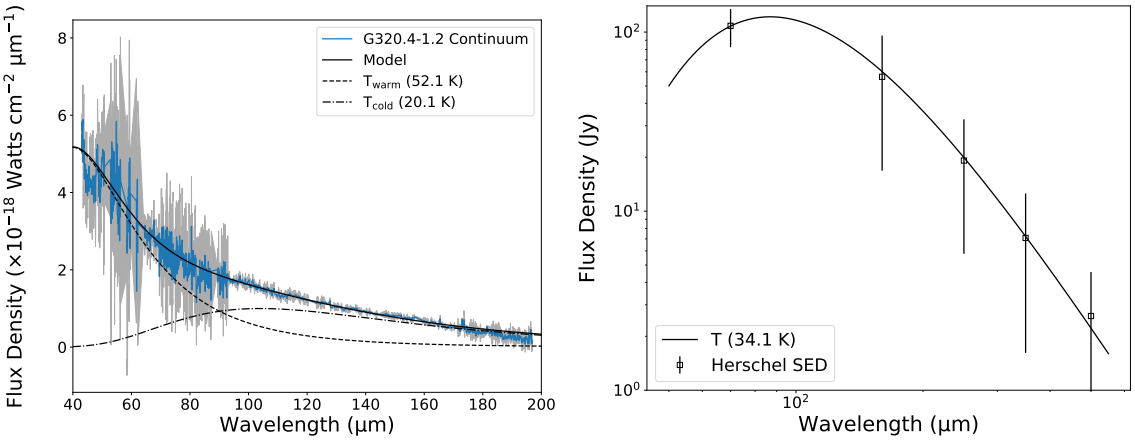

Figure 4.32: Left: Continuum spectrum of G320.4–1.2 obtained with the ISO LWS, with emission lines removed. Our best–fit two–component blackbody model is overlaid. A warm component ($T \sim 52$ K) dominates the spectrum at $\lambda \lesssim 90$ μm, while the cold component ($T \sim 20$ K) dominates at $\lambda \gtrsim 90$ μm. Right: Herschel background–subtracted SED of the center of G320.4–1.2 fit with our blackbody model, $T \sim 34$ K.

4.9 References

Alan, N., Park, S., & Bilir, S. 2019, ApJ, 873, 53

Andersen, M., Rho, J., Reach, W. T., Hewitt, J. W., & Bernard, J. P. 2011, ApJ, 742, 7

Arendt, R. G. 1991, AJ, 101, 2160

Arikawa, Y., Tatematsu, K., Sekimoto, Y., & Takahashi, T. 1999, PASJ, 51, L7

Bennett, C. L., Fixsen, D. J., Hinshaw, G., et al. 1994, ApJ, 434, 587

Bertoldi, F., Carilli, C. L., Cox, P., et al. 2003, A&A, 406, L55

Bietenholz, M. F., & Bartel, N. 2008, MNRAS, 386, 1411

Bilikova, J., Williams, R. N. M., Chu, Y. H., Gruendl, R. A., & Lundgren, B. F. 2007, AJ, 134, 2308

Blair, W. P., Sankrit, R., Shelton, R., et al. 2000, ApJL, 538, L61

Bocchino, F., Bandiera, R., & Gelfand, J. 2010, A&A, 520, A71

Borkowski, K. J., Reynolds, S. P., & Miltich, W. 2020, ApJL, 895, L32

Boulanger, F., Abergel, A., Bernard, J. P., et al. 1996, A&A, 312, 256

Burton, M., & Spyromilio, J. 1993, Proceedings of the Astronomical Society of Australia, 10, 327

Burton, M. G., Geballe, T. R., Brand, P. W. J. L., & Webster, A. S. 1988, MNRAS, 231, 617

Burton, M. G., Hollenbach, D. J., & Tielens, A. G. G. M. 1990, ApJ, 365, 620

Carter, L. M., Dickel, J. R., & Bomans, D. J. 1997, PASP, 109, 990

Cesarsky, D., Cox, P., Pineau des Forêts, G., et al. 1999, A&A, 348, 945

Cha, H., Rho, J., An, H., & Millard, M. 2021, submitted to ApJ

Chawner, H., Marsh, K., Matsuura, M., et al. 2019, MNRAS, 483, 70

Chawner, H., Gomez, H. L., Matsuura, M., et al. 2020, MNRAS, 493, 2706

Cox, D. P., Shelton, R. L., Maciejewski, W., et al. 1999, ApJ, 524, 179

De Looze, I., Barlow, M. J., Bandiera, R., et al. 2019, MNRAS, 488, 164

Denoyer, L. K. 1979, ApJL, 232, L165

Dickman, R. L., Snell, R. L., Ziurys, L. M., & Huang, Y.-L. 1992, ApJ, 400, 203

Docenko, D., & Sunyaev, R. A. 2010, A&A, 509, A59

Dwek, E., & Arendt, R. G. 2008, ApJ, 685, 976

Finkelstein, S. L., Morse, J. A., Green, J. C., et al. 2006, ApJ, 641, 919

Flanagan, K. A., Canizares, C. R., Dewey, D., et al. 2004, ApJ, 605, 230

Frank, K. A., Burrows, D. N., & Park, S. 2015, ApJ, 810, 113

Gaensler, B. M., Brazier, K. T. S., Manchester, R. N., Johnston, S., & Green, A. J. 1999, MNRAS, 305, 724

Gelfand, J. D., Slane, P. O., & Temim, T. 2015, ApJ, 807, 30

Giacani, E., Smith, M. J. S., Dubner, G., et al. 2009, A&A, 507, 841

Godard, B., Pineau des Forêts, G., Lesaffre, P., et al. 2019, A&A, 622, A100

Gomez, H. L., Krause, O., Barlow, M. J., et al. 2012, ApJ, 760, 96

Gotthelf, E. V., Vasisht, G., Boylan-Kolchin, M., & Torii, K. 2000, ApJL, 542, L37

Green, D. A. 1989, MNRAS, 238, 737

Green, D. A., & Dewdney, P. E. 1992, MNRAS, 254, 686

Green, D. A., Tuffs, R. J., & Popescu, C. C. 2004, MNRAS, 355, 1315

Griffin, M. J., Abergel, A., Abreu, A., et al. 2010, A&A, 518, L3

Gry, C., Swinyard, B., Harwood, A., et al. 2003, The ISO Handbook, Volume III - LWS - The Long Wavelength Spectrometer

Guest, B. T., Safi-Harb, S., & Tang, X. 2019, MNRAS, 482, 1031

Hattori, S., Straal, S. M., Zhang, E., et al. 2020, ApJ, 904, 32

He, J. H., Szczerba, R., Chen, P. S., & Sobolev, A. M. 2005, A&A, 434, 201

Heydari-Malayeri, M., Kahane, C., & Lucas, R. 1981, Nature, 293, 549

Hirashita, H., Burgarella, D., & Bouwens, R. J. 2017, MNRAS, 472, 4587

Hollenbach, D., & McKee, C. F. 1989, ApJ, 342, 306

Isaak, K. G., Priddey, R. S., McMahon, R. G., et al. 2002, MNRAS, 329, 149

James, A., Dunne, L., Eales, S., & Edmunds, M. G. 2002, MNRAS, 335, 753

Kilpatrick, C. D., Bieging, J. H., & Rieke, G. H. 2016, ApJ, 816, 1

Kirshner, R. P., Morse, J. A., Winkler, P. F., & Blair, W. P. 1989, ApJ, 342, 260

Kokusho, T., Torii, H., Nagayama, T., et al. 2020, ApJ, 899, 49

Koo, B.-C., McKee, C. F., Suh, K.-W., et al. 2011, ApJ, 732, 6

Kothes, R., Uyaniker, B., & Yar, A. 2002, ApJ, 576, 169

Kuriki, M., Sano, H., Kuno, N., et al. 2018, ApJ, 864, 161

Lagache, G., Abergel, A., Boulanger, F., & Puget, J. L. 1998, A&A, 333, 709

Laporte, N., Ellis, R. S., Boone, F., et al. 2017, ApJL, 837, L21

Law, C. J., Milisavljevic, D., Patnaude, D. J., et al. 2020, ApJ, 894, 73

Leahy, D. A., Tian, W., & Wang, Q. D. 2008, AJ, 136, 1477

Leahy, D. A., & Tian, W. W. 2008, A&A, 480, L25

Leisawitz, D., Amatucci, E., Allen, L., et al. 2021, Journal of Astronomical Telescopes, Instruments, and Systems, 7, 011014

Liseau, R., Justtanont, K., & Tielens, A. G. G. M. 2006, A&A, 446, 561

Liu, X. W., Barlow, M. J., Cohen, M., et al. 2001, MNRAS, 323, 343

Lloyd, C., Lerate, M. R., & Grundy, T. R. 2003, The LWS L01 Pipeline, , . http://ida.esac.esa.int:8080/hpdp/technical_reports/technote34.html

Lundqvist, N., Lundqvist, P., Björnsson, C. I., et al. 2011, MNRAS, 413, 611

Lundqvist, P., Sollerman, J., Kozma, C., et al. 1999, A&A, 347, 500

Lundqvist, P., Lundqvist, N., Vlahakis, C., et al. 2020, MNRAS, 496, 1834

Mathewson, D. S., Dopita, M. A., Tuohy, I. R., & Ford, V. L. 1980, ApJL, 242, L73

Morgan, H. L., & Edmunds, M. G. 2003, MNRAS, 343, 427

Morse, J. A., Winkler, P. F., & Kirshner, R. P. 1995, AJ, 109, 2104

Nakagawa, T., Yui, Y. Y., Doi, Y., et al. 1998, ApJS, 115, 259

Newville, M., Stensitzki, T., Allen, D. B., & Ingargiola, A. 2014, LMFIT: Non-Linear Least-Square Minimization and Curve-Fitting for Python, v0.8.0, Zenodo, doi:10.5281/zenodo.11813

Nozawa, T., Kozasa, T., Umeda, H., Maeda, K., & Nomoto, K. 2003, ApJ, 598, 785

Oliva, E., Drapatz, S., Lutz, D., Sturm, E., & Moorwood, A. F. M. 1998, Ap&SS, 255, 211

Oliva, E., Moorwood, A. F. M., & Danziger, I. J. 1989, A&A, 214, 307

Oliva, E., Moorwood, A. F. M., Drapatz, S., Lutz, D., & Sturm, E. 1999, A&A, 343, 943

Otsuka, M., van Loon, J. T., Long, K. S., et al. 2010, A&A, 518, L139

Owen, P. J., & Barlow, M. J. 2015, ApJ, 801, 141

Pannuti, T. G., Rho, J., Kargaltsev, O., et al. 2017, ApJ, 839, 59

Park, S., Burrows, D. N., Garmire, G. P., et al. 2003, ApJ, 586, 210

Park, S., Hughes, J. P., Slane, P. O., et al. 2012, ApJ, 748, 117

Park, S., Hughes, J. P., Slane, P. O., Mori, K., & Burrows, D. N. 2010, ApJ, 710, 948

Paron, S. A., Reynoso, E. M., Purcell, C., Dubner, G. M., & Green, A. 2006, PASA, 23, 69

Peeters, E., Martín-Hernández, N. L., Damour, F., et al. 2002, A&A, 381, 571

Pineda, J. L., Langer, W. D., Velusamy, T., & Goldsmith, P. F. 2013, A&A, 554, A103

Pinheiro Gonçalves, D., Noriega-Crespo, A., Paladini, R., Martin, P. G., & Carey, S. J. 2011, AJ, 142, 47

Planck Collaboration, Ade, P. A. R., Aghanim, N., et al. 2014, A&A, 564, A45

Poglitsch, A., Waelkens, C., Geis, N., et al. 2010, A&A, 518, L2

Reach, W. T., & Rho, J. 1996, A&A, 315, L277

—. 1998, ApJL, 507, L93

—. 2000, ApJ, 544, 843

Reach, W. T., Tram, L. N., Richter, M., Gusdorf, A., & DeWitt, C. 2019, ApJ, 884, 81

Reach, W. T., Dwek, E., Fixsen, D. J., et al. 1995, ApJ, 451, 188

Reynolds, S. P. 1985, ApJ, 291, 152

Reynoso, E. M., Green, A. J., Johnston, S., et al. 2004, PASA, 21, 82

Rho, J., & Borkowski, K. J. 2002, ApJ, 575, 201

Rho, J., Jarrett, T. H., Cutri, R. M., & Reach, W. T. 2001, ApJ, 547, 885

Rho, J., & Petre, R. 1997, ApJ, 484, 828

Rho, J., Reach, W. T., Tappe, A., et al. 2009, ApJ, 700, 579

Rho, J., Gomez, H. L., Boogert, A., et al. 2018, MNRAS, 479, 5101

Sánchez-Cruces, M., Rosado, M., Fuentes-Carrera, I., & Ambrocio-Cruz, P. 2018, MNRAS, 473, 1705

Sarangi, A., & Cherchneff, I. 2015, A&A, 575, A95

Seitenzahl, I. R., Vogt, F. P. A., Terry, J. P., et al. 2018, ApJL, 853, L32

Seok, J. Y., Koo, B.-C., Onaka, T., et al. 2008, PASJ, 60, S453

Sharda, P., Gaetz, T. J., Kashyap, V. L., & Plucinsky, P. P. 2020, ApJ, 894, 145

Sluder, A., Milosavljević, M., & Montgomery, M. H. 2018, MNRAS, 480, 5580

Smith, N. 2013, MNRAS, 434, 102

Snell, R. L., Hollenbach, D., Howe, J. E., et al. 2005, ApJ, 620, 758

Sollerman, J. 2002, NewAR, 46, 493

Stanimirović, S., Weisberg, J. M., Dickey, J. M., et al. 2003, ApJ, 592, 953

Su, Y., Chen, Y., Yang, J., et al. 2009, The Astrophysical Journal, 694, 376. https://doi.org/10.1088%2F0004-637x%2F694%2F1%2F376

Tappe, A., Rho, J., Boersma, C., & Micelotta, E. R. 2012, ApJ, 754, 132

Tappe, A., Rho, J., & Reach, W. T. 2006, ApJ, 653, 267

Tatematsu, K., Fukui, Y., Iwata, T., Seward, F. D., & Nakano, M. 1990, ApJ, 351, 157

Tatematsu, K., Fukui, Y., Nakano, M., et al. 1987, A&A, 184, 279

Temim, T., & Dwek, E. 2013, ApJ, 774, 8

Temim, T., Slane, P., Reynolds, S. P., Raymond, J. C., & Borkowski, K. J. 2010, ApJ, 710, 309

Temim, T., Slane, P., Sukhbold, T., et al. 2019, ApJL, 878, L19

Tian, W. W., & Leahy, D. A. 2008, MNRAS, 391, L54

Todini, P., & Ferrara, A. 2001, MNRAS, 325, 726

Trimble, V. 1968, AJ, 73, 535

Troja, E., Bocchino, F., & Reale, F. 2006, ApJ, 649, 258

van Dishoeck, E. F., Jansen, D. J., & Phillips, T. G. 1993, A&A, 279, 541

Velázquez, P. F., Dubner, G. M., Goss, W. M., & Green, A. J. 2002, AJ, 124, 2145

Vermeij, R., Damour, F., van der Hulst, J. M., & Baluteau, J. . P. 2002, A&A, 390, 649

Vermeij, R., & van der Hulst, J. M. 2002, A&A, 391, 1081

Williams, B. J., Borkowski, K. J., Reynolds, S. P., et al. 2008, ApJ, 687, 1054

Wootten, A. 1981, ApJ, 245, 105

Yuan, Y., & Neufeld, D. A. 2011, ApJ, 726, 76

Zhou, P., Chen, Y., Safi-Harb, S., et al. 2016, ApJ, 831, 192

Zhou, P., Vink, J., Safi-Harb, S., & Miceli, M. 2019, A&A, 629, A51

CHAPTER 5

Conclusions

This work presents kinematic studies of high-speed ejecta in SNRs at X-ray and infrared wavelengths. In X-rays, we use our high-resolution Chandra HETG spectroscopic data to measure radial velocities of numerous small emission features in the historical Galactic Type Ia SNRs, Kepler and Tycho. We build the 3-D structure of clumpy stellar debris in these SNRs in unprecedented detail. We note that similar studies were performed for these SNRs based on low-resolution CCD spectroscopy of Chandra ACIS detectors (Sato & Hughes, 2017a,b; Williams et al., 2017). Those previous CCD spectroscopic studies suffered from significant systematic uncertainties up to a few 1000 km s^{-1} (i.e., typically $\sim$ 50% or larger errors) on the radial velocity measurements of clumpy ejecta gas in Kepler and Tycho, which made it difficult to establish reliable 3–D structures of stellar debris in these SNRs. Our high-resolution Chandra HETG spectroscopy is not contaminated by such systematic uncertainties, and we measure radial velocities of small ejecta gas typically within statistical uncertainties of a few 100 km s^{-1}, a nearly order of magnitude improvement on the velocity measurements from the previous works. With these accurate measurements, we for the first time construct the 3-D structures of X-ray emitting hot stellar debris in these prominent Type Ia SNRs.

Highlights of our results include the detection of a few very high-speed (nearly freely expanding at the space velocities of $\sim 10^4$ km s^{-1}) clumpy ejecta gas in Kepler. We also detect high-speed ejecta gas that is spatially coincident with the peculiar emission feature called an "Ear" that extends well beyond the main shell of Kepler.

In Tycho, we estimated a potential secondary reverse-shock location, a new expansion center, and investigated the 3—D ejecta structure, which showed a significant north–south ejecta asymmetry along the line of sight, all of which have been unknown before. For the first time, we perform statistically significant measurements of the radial velocity of the peculiar ejecta features projected beyond the main shell of the SNR in the southeastern boundary. Three-dimensional simulations from SNe to SNRs are recently becoming more prevalent, and a growing number of evidence has indicated the importance of asymmetric SN explosions and the subsequent SN evolution in non-uniform environments (Ferrand et al., 2019, 2021; Orlando et al., 2020, 2021; Tutone et al., 2020; Griffeth Stone et al., 2021). In this new era of SN/SNR studies, observational constraints on the detailed 3-D nature of stellar debris in SNRs are critically important to construct more realistic physical modeling of SN and SNRs (Ferrand, 2020). Our study of 3-D structures of stellar debris in Kepler and Tycho provides new observational constraints on the kinematics of ejecta gas and their spatial structures in unprecedented detail and accuracy, particularly to help advance physical modeling and understanding of Type Ia SN explosions.

In our infrared study, we investigate the dust created in the ejecta of CC–SNRs, because it may help to determine if SNe are the main source of the large galactic dust masses observed in the early Universe. Previous studies have estimated dust masses of $\sim$ 0.01 – 1 $M_{\odot}$ in CC SNRs (Rho et al., 2009; Gomez et al., 2012; Matsuura et al., 2015; De Looze et al., 2017; Rho et al., 2018; Chawner et al., 2019), which may suggest CC SNe as a significant source of interstellar dust observed at high redshifts. We present previously unpublished archival ISO FIR spectroscopy of 20 SNRs, and identified several SNRs with broad emission line profiles, indicating that the emission may originate from high-speed ejecta. We also clearly detect FIR continuum emission in most of these SNRs, indicative of dust formation. In particular, based on the IR

spectroscopy of SNR G320.4–1.2, we estimate a significant dust mass of $\sim 0.1 - 0.2$ $M_{\odot}$ in this SNR. Our results provide another important piece of puzzle to reveal the main source of dust formation in the early Universe, motivating follow-up high-resolution IR spectroscopic studies of CC SNRs with modern detectors such as JWST for the study of the origin of interstellar dust.

5.1 References

Chawner, H., Marsh, K., Matsuura, M., et al. 2019, MNRAS, 483, 70

De Looze, I., Barlow, M. J., Swinyard, B. M., et al. 2017, MNRAS, 465, 3309

Ferrand, G. 2020, Astronomische Nachrichten, 341, 143

Ferrand, G., Warren, D. C., Ono, M., et al. 2019, ApJ, 877, 136

—. 2021, ApJ, 906, 93

Gomez, H. L., Krause, O., Barlow, M. J., et al. 2012, ApJ, 760, 96

Griffeth Stone, A., Johnson, H. T., Blondin, J. M., et al. 2021, ApJ, 923, 233

Matsuura, M., Dwek, E., Barlow, M. J., et al. 2015, ApJ, 800, 50

Orlando, S., Wongwathanarat, A., Janka, H. T., et al. 2021, A&A, 645, A66

Orlando, S., Ono, M., Nagataki, S., et al. 2020, A&A, 636, A22

Rho, J., Reach, W. T., Tappe, A., et al. 2009, ApJ, 700, 579

Rho, J., Gomez, H. L., Boogert, A., et al. 2018, MNRAS, 479, 5101

Sato, T., & Hughes, J. P. 2017a, ApJ, 840, 112

—. 2017b, ApJ, 845, 167

Tutone, A., Orlando, S., Miceli, M., et al. 2020, A&A, 642, A67

Williams, B. J., Coyle, N. M., Yamaguchi, H., et al. 2017, ApJ, 842, 28

APPENDIX A

Line Emisison Ratios

To determine the line emission contributions from electronic shell transitions of Si XIII and Si XII, we measured the temperature and ionization timescale of each knot by fitting an absorbed plane shock model to its broadband (0.3 - 7.0 keV) ACIS spectrum (see Section 2.3.3). We show our results in Table A.1. Based on each knot's best-fit temperature and ionization timescale, we used a `phabs*vvpshock` model to calculate the line ratios using XSPEC (version 12.10) with NEI APEC spectral data (version 3.0.9) (Arnaud, 1996; Smith et al., 2001). Our best-fit ACIS broadband models (see Section 2.3.3) suggest ratio values ranging from $\sim$ 0.05 - 0.23 and 0.47 - 2.15 for *i/r* and *f/r*, respectively. The 6.717 Å and 6.782 Å Si XII line ratios vary from 0.03 - 1.96 and 8e-4 - 0.98, respectively. Figure A1 shows contour plots of each line ratio for a range of temperatures and ionization timescales. Varying the line ratio values used in each measurement does not significantly affect our main results for the high v_r knots (N1 - N3, N5), and although our sample size is limited, the overall dominance of the redshift in the ejecta v_r also does not change. Hence, the overall results of our HETG v_r measurements are generally independent of the line ratio values estimated from the ACIS model fits.

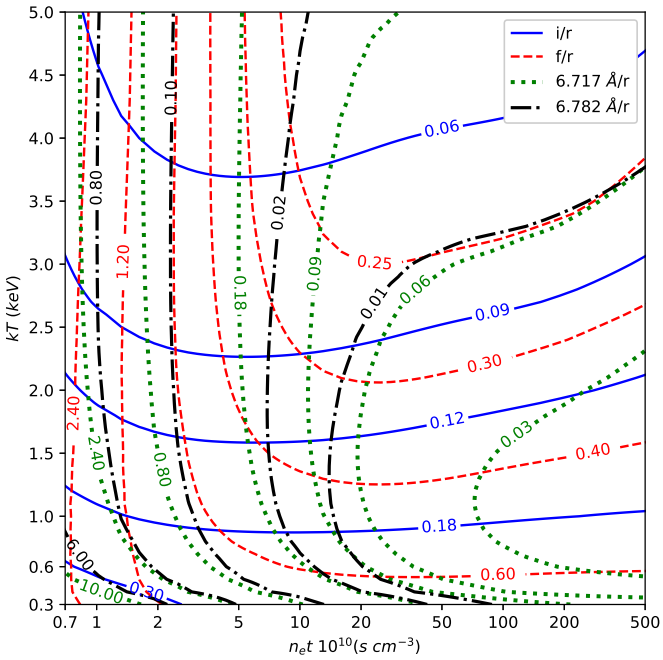

Figure A.1: Contours of line emission ratios for various temperatures and ionization timescales. The blue solid and red dashed contours represent ratio values of of Si XIII intercombination to resonance, and forbidden to resonance line fluxes, respectively. The green dotted and black dashed-dotted contours show ratio values of Si XII emission lines 6.717 $\mathring{A}$ and 6.782 $\mathring{A}$, to the Si XIII resonance line (r), respectively.

Table A.1. ACIS Spectral Fitting Results

Region	kT (keV)	τ (10^{10}s cm^{-3})[a]	Redshift (10^{-2})	K (10^{8}cm^{-5})[b]	χ^2/dof	i/r[c]	f/r[d]
N2	$3.86^{+0.94}_{-0.75}$	$2.18^{+0.28}_{-0.23}$	$2.66^{+0.07}_{-0.22}$	$12.8^{+2.2}_{-1.9}$	191.2/138	0.06	0.67
N1	$2.15^{+0.41}_{-0.33}$	$2.32^{+0.30}_{-0.26}$	$2.47^{+0.01}_{-0.28}$	$9.99^{+2.06}_{-1.46}$	131.9/103	0.10	0.64
N3	$3.49^{+0.69}_{-0.59}$	$2.16^{+0.17}_{-0.04}$	$2.13^{+0.07}_{-0.08}$	$10.4^{+1.2}_{-1.0}$	135.8/113	0.06	0.67
C3	$2.44^{+0.49}_{-0.42}$	$0.99^{+0.22}_{-0.14}$	$0.15^{+0.05}_{-0.05}$	$8.27^{+1.04}_{-1.02}$	120.3/108	0.10	1.77
N4	$4.49^{+2.25}_{-0.72}$	$1.85^{+0.36}_{-0.29}$	$1.08^{+0.10}_{-0.01}$	$4.47^{+0.33}_{-0.25}$	144.9/104	0.05	0.85
Ear1	$0.56^{+0.02}_{-0.04}$	$78.2^{+54.6}_{-19.2}$	$1.61^{+0.08}_{-0.05}$	$5.78^{+1.14}_{-0.48}$	135.8/103	0.22	0.59
C1	$3.64^{+1.03}_{-0.69}$	$2.11^{+0.28}_{-0.21}$	$0.31^{+0.04}_{-0.01}$	$4.76^{+0.64}_{-0.66}$	145.2/109	0.06	0.69
Ear2	$2.39^{+0.52}_{-0.38}$	$1.08^{+0.06}_{-0.12}$	$0.74^{+0.03}_{-0.04}$	$4.81^{+1.15}_{-0.57}$	114.1/112	0.10	1.58
N6	$3.34^{+0.88}_{-0.87}$	$2.58^{+0.52}_{-0.22}$	$0.80^{+0.01}_{-0.18}$	$3.07^{+0.40}_{-0.39}$	135.9/98	0.07	0.55
E	$3.05^{+0.39}_{-0.30}$	$1.52^{+0.27}_{-0.09}$	$1.06^{+0.01}_{-0.26}$	$29.3^{+1.6}_{-2.6}$	159.0/137	0.08	1.03
C2*	$1.27^{+0.12}_{-0.11}$	$5.15^{+1.34}_{-0.77}$	$0.19^{+1.10}_{-0.18}$	$29.8^{+2.8}_{-1.2}$	115.8/109	0.14	0.47
N7	$0.80^{+0.01}_{-0.02}$	$73.5^{+14.9}_{-11.2}$	$0.14^{+0.01}_{-0.17}$	108^{+7}_{-5}	194.9/143	0.19	0.51
C4*	$0.80^{+0.06}_{-0.07}$	$12.5^{+2.6}_{-2.4}$	$-0.33^{+0.02}_{-0.08}$	$97.1^{+8.4}_{-9.1}$	165.2/119	0.19	0.52
S1	$2.16^{+0.63}_{-0.59}$	$1.08^{+0.18}_{-0.12}$	$-0.49^{+0.12}_{-0.01}$	$1.38^{+0.53}_{-0.24}$	126.1/92	0.10	1.56
S2	$0.53^{+0.02}_{-0.02}$	300^{+1590}_{-131}	$-0.50^{+0.03}_{-0.04}$	$11.4^{+1.9}_{-0.3}$	137.0/107	0.23	0.61
Ear3	$4.02^{+1.73}_{-1.04}$	$0.94^{+0.12}_{-0.09}$	$-1.18^{+0.05}_{-0.11}$	$3.36^{+0.35}_{-0.66}$	139.9/107	0.07	2.15
N5	$4.93^{+1.84}_{-1.32}$	$1.16^{+0.12}_{-0.13}$	$-1.68^{+0.06}_{-0.02}$	$4.02^{+1.04}_{-1.02}$	146.4/113	0.05	1.68

[a] $\tau = n_e t$, where n_e is the electron density, and t is the time since the plasma was shocked.

[b] $K = \int n_e n_H dV / 4\pi d^2$, where n_H is the hydrogen density, V is the volume of the region, and d is the distance to the region.

[c] Si Kα intercombination (i) to resonance (r) line ratio.

[d] Si Kα forbidden (f) to resonance line ratio.

APPENDIX B

ISO Survey

In Table B.1 we list the SNRs observed with the *ISO* LWS that were not included in our sample. In most cases, we did not choose these data because they were previously published. In other cases, the data quality was poor and suffered from inadequate sampling of emission line profiles.

B.1 Paris–Durham Models

The line intensities of the C–shock models presented in Figure 4.30 are computed using the Paris–Durham shock code, which simulates the progression of a shock wave through a gaseous medium (Godard et al., 2019). By incorporating relevant heating, cooling, and grain processes, as well as a network of chemical reactions, the code finds the kinematic, thermodynamic, and chemical properties of the shocked layer. These models assume that the shock is irradiated by an external radiation field. Thus, the model contains a pre-shock radiative buffer created by the coupling of the radiation field with the inferred molecular cloud.

To account for an irradiated shock, we run the code in three stages. In the first stage, the code calculates the chemical and thermal conditions at the border of the radiative buffer and the diffuse interstellar medium. In the second stage, the conditions inside the buffer are evolved until the desired extinction (A_v) value is reached. Here, we choose the standard A_v value of 10^{-1} (Godard et al., 2019). In the final stage, the propagation of the shock is computed. In this stage, we performed multiple runs to calculate the model line fluxes for a range of shock velocities (v_s = 5 – 30 km s^{-1}) and pre-shock densities (n_o = 10^3 – 10^6 cm^{-3}). We compared the resulting [O I] 63 and 145 μm and [C II] 158 μm line intensities for each model with our measured values (see Figure 4.30). The relevant input parameters are listed in Table B.2.

Table B.1. *ISO* LWS SNR Observations Not in Our Sample

Name	Target Name*	RA, DEC (J2000)	Date	t_{on} (s)	Publications
G6.4–0.1	W28masA	$18^h01^m52^s.32$ –23°19′25″.7	1997-03-17	1346	1,2,12
G10.0–00.3	SGR1806-20	$18^h08^m40^s.30$ –20°24′40″.9	1997-03-23	730	–
G10.0–00.3	SGR1806-20 Bkg	$18^h08^m23^s.72$ –20°29′42″.1	1997-03-23	729	–
G31.9+0.0	3C391	$18^h49^m20^s.95$ –00°55′48″.4	1996-04-28	1414	1,2,10,12
G31.9+0.0	3C391mol	$18^h49^m21^s.93$ –00°57′22″.1	1997-03-10	1300	1,2,12
G31.9+0.0	3C391mol (L04)	$18^h49^m21^s.93$ –00°57′22″.1	1997-03-10	962	2,12
G31.9+0.0	3C391H20 (L02)	$18^h49^m21^s.95$ –00°57′22″.9	1997-10-26	1720	1,2,12
G31.9+0.0	3C391cut2 (L02)	$18^h49^m26^s.80$ –00°55′48″.7	1997-03-10	892	1,2,12
G31.9+0.0	3C391cut3 (L02)	$18^h49^m31^s.79$ –00°55′20″.4	1997-03-10	824	1,2,12
G31.9+0.0	3C391cut4 (L02)	$18^h49^m17^s.32$ –00°57′04″.4	1997-03-10	754	1,2,12
G34.7–0.4	W44 (L02) 1	$18^h56^m32^s.41$ +01°28′15″.6	1996-04-28	1680	1,2,10,11,12
G34.7–0.4	W44 (L02) 2	$18^h56^m28^s.37$ +01°29′59″.3	1996-04-28	1462	1,2,10,11,12
G34.7–0.4	W44cut3 (L02)	$18^h56^m00^s.36$ +01°12′49″.00	1997-03-10	1520	2,12

Table B.1 (cont'd)

Name	Target Name*	RA, DEC (J2000)	Date	t_{on} (s)	Publications
G34.7–0.4	W44masA	$18^h56^m28^s.33$ $+01°29'58''.90$	1997-03-10	962	2,12
G34.7–0.4	W44masA (L04)	$18^h56^m28^s.33$ $+01°29'59''.00$	1997-03-10	1300	2,12
G35.2–1.7	W48 (L04)	$19^h01^m47^s.60$ $+01°13'6''.10$	1996-10-24	2312	–
G042.8+00.6	SGR1900+14	$19^h07^m15^s.22$ $+09°19'21''.6$	1996-09-27	978	–
G042.8+00.6	SGR1900+14 (Bkg)	$19^h07^m09^s.18$ $+09°15'21''.3$	1997-03-29	1029	–
G111.7–2.1	Cas A #1	$23^h23^m27^s.75$ $+58°48'47''.0$	1996-06-24	1054	13
G111.7–2.1	Cas A #2	$23^h23^m26^s.74$ $+58°50'09''.9$	1996-06-24	1052	13
G111.7–2.1	Cas A #3	$23^h23^m18^s.70$ $+58°47'30''.8$	1996-06-24	1054	13
G111.7–2.1	Cas A #4	$23^h23^m53^s.94$ $+58°50'24''.3''$	1996-06-24	1054	13
G111.7–2.1	Cas A #5	$23^h23^m38^s.33$ $+58°49'22''.1$	1997-06-09	1612	13
G111.7–2.1	Cas A #6	$23^h23^m35^s.12$ $+58°47'38''.0$	1997-06-09	1612	13
G111.7–2.1	Cas A #7	$23^h23^m16^s.47$ $+58°49'07''.8$	1997-06-02	1614	13
G184.6–05.8	Crab Nebula #1	$05^h34^m34^s.27$ $+22°01'02''.4$	1997-10-11	1124	14,17

Table B.1 (cont'd)

Name	Target Name*	RA, DEC (J2000)	Date	t_{on} (s)	Publications
G184.6–05.8	Crab Nebula #2	$05^h34^m31^s.94$ $+22°02'04''.8$	1997-10-09	1126	14,17
G184.6–05.8	Crab Nebula #3	$05^h34^m29^s.31$ $+22°00'37''.0$	1997-10-09	1124	14,17
G184.6–05.8	Crab Nebula #4	$05^h34^m34^s.19$ $+21°59'54''.7$	1997-10-09	1630	14,17
G184.6–05.8	Crab Nebula (L02 Narrow)	$05^h34^m32^s.02$ $+22°02'04''.5$	1998-02-19	1184	–
G184.6–05.8	Crab Nebula (L02 Narrow)	$05^h34^m32^s.02$ $+22°02'04''.6$	1998-04-04	1184	–
G189.1+3.0	IC443cut	$06^h17^m49^s.69$ $+22°45'28''.4$	1998-03-13	1218	3, 12
G189.1+3.0	IC443 – C FP Scan (L04) 1.	$06^h17^m42^s.80$ $+22°21'37''.7$	1998-03-13	1574	–
G189.1+3.0	IC443 – C FP Scan (L04) 2.	$06^h17^m07^s.64$ $+22°25'34''.7$	1998-04-04	2230	–
G315.4–2.3	RCW 86	$14^h43^m04^s.20$ $-62°27'44''.4$	1996-02-14	812	–
G332.4–0.4	RCW103 H2+ion	$16^h17^m35^s.78$ $-51°06'18''.6$	1996-02-23	4160	4,5
J0047.2–7308	SMC0045 (L04)	$00^h47^m17^s.06$ $-73°08'29''.3$	1997-05-11	1694	–
J0048.5–7319	SMC0046 0 (L04)	$00^h48^m25^s.43$ $-73°19'16''.3$	1997-05-11	1020	–
J0059.4–7210	SMC N66	$00^h59^m8^s.02$ $-72°10'25''.97$	1996-04-01	815	6,8,9

Table B.1 (cont'd)

Name	Target Name*	RA, DEC (J2000)	Date	t_{on} (s)	Publications
J0535–6916	SN 1987A	$05^h35^m28^s.04$ –69°16′11″.7	1998-02-04	3428	15,16
J0537.8–6910	LMC-N157B	$05^h37^m51^s.76$ –69°10′22″.0	1996-04-29	1054	8,9

Note. — 1. (Reach & Rho, 1998) 2. (Reach & Rho, 2000) 3. (Rho et al., 2001) 4. (Oliva et al., 1998) 5. (Oliva et al., 1999) 6. (Liseau et al., 2006) 7. (He et al., 2005) 8. (Vermeij & van der Hulst, 2002) 9. (Vermeij et al., 2002) 10. (Reach & Rho, 1996) 11. (Cox et al., 1999) 12. (Yuan & Neufeld, 2011) 13. (Docenko & Sunyaev, 2010) 14. (Green et al., 2004) 15. (Lundqvist et al., 1999) 16. (Sollerman, 2002) 17. (Gomez et al., 2012)

*The observing mode is in parentheses. L01–L02: Grating, L03–L04: Fabry-Pérot.

Table B.2: Paris–Durham Input Parameters

Parameter	Value
n_H, pre-shock proton density	10^3 – 10^6 cm^{-3}
G_o, radiation field scaling factor	1
A_V^o, pre-shock visual extinction	0.1
V_s, shock speed	5 – 30 km s^{-1}
b, magnetic field parameter	1[a]
ζ_{H_2}, H_2 cosmic ray ionization rate	3×10^{-17} s^{-1}
u_{turb}, turbulent velocity	1 km s^{-1}
$timeJ$, shock age	$10^3 - 10^4$ yr

[a]Dimensionless value of the initial magnetic field transverse to the plane of the shock, $b = B_o[\mu G]/(n_H)^{1/2}$.